The Dissertation Committee for David Roger Miller
certifies that this is the approved version of the following dissertation:

# *In Vivo* Optical Imaging to Investigate Neurovascular Structure and Cerebral Hemodynamics

Committee:

Andrew K. Dunn, Supervisor

Thomas E. Milner

Hsin-Chih "Tim" Yeh

Theresa A. Jones

# *In Vivo* Optical Imaging to Investigate Neurovascular Structure and Cerebral Hemodynamics

**by**

**David Roger Miller**

**DISSERTATION**

Presented to the Faculty of the Graduate School of

The University of Texas at Austin

in Partial Fulfillment

of the Requirements

for the Degree of

**DOCTOR OF PHILOSOPHY**

THE UNIVERSITY OF TEXAS AT AUSTIN

May 2018

I dedicate this dissertation to my loving parents, siblings, friends, and mentors.

# Acknowledgments

A million thanks to my parents, Shelley and Marvin Miller. I am incredibly honored to be your son, and so proud of you both. My thirst for knowledge was undoubtedly distilled by my parents. I am forever grateful for your enormous sacrifices to provide me an incredible education, and for your willingness to support me wherever my curiosity led - little did you know how impactful giving me "The Feynman Lectures" would be. I thank you for your unwavering support and encouragement. I look back fondly on driving to Sinclair every morning, chess tournaments in Columbus, and even math problems on Saturdays. Moreover, I cannot begin to describe how instrumental attending Carleton was for the development of me as both a person and scientist. I am forever in your debt for supporting me financially and emotionally during that time. I strive to make you proud and fulfill our motto: "To whom much is given, much is expected." I certainly feel you have given me so much - above all, a loving home and family. Yasher koach!

I thank my siblings for their unconditional love. Sarah, you have shaped my perspective on education and inspire me to engage with and empower underrepresented groups. Rubin, your generosity and inclusiveness has opened my eyes to the breadth of the world. Rachel, your kindness is contagious. Your home is an oasis for the mind. Levi, I look forward to seeing your successes -

I will always be your biggest fan in whatever endeavor you pursue.

Graduate school was a rollercoaster of emotions. I thank my friends for lifting my spirits up when I needed it most, and for introducing me to new ideas and experiences. I am much appreciative of the cross pollination of ideas I have shared during my time in Austin. Thank you Jacob Speedy, Owen Demke, Taylor Want, Alex Hannah, Jon Clutton, Cristina Rodgers, Casey LeMay and so many more.

I feel incredibly privileged to have had numerous brilliant mentors shape my path. Dr. Joel Weisberg, you have become a cherished friend. Your insights into the world around you - both in mystical pulsars and ethereal physical theories - inspired me to find my passion at the intersection of physics and the brain. Thank you for allowing me to pursue my interests for my Senior Thesis - it has led me down a path of passion and discovery.

I am incredibly grateful for the guidance from my PhD advisor, Dr. Andrew Dunn, as well as mentors Dr. Thomas Milner, Dr. Tim Yeh, Dr. Nelson Christensen, Dr. Bob Metcalfe, Louise Epstein, Dr. Costas Anastassiou, and Howard Sales.

I am especially grateful for the enormous help I received throughout my tenure in the Dunn lab. Dr. Evan Perillo, Dr. Jeremy Jarrett, Dr. Flor Medina, Dr. Shams Kazmi, Ahmed Hassan, and Taylor Clark were instrumental in performing deep imaging studies in mice. Dr. Mitch Davis for vectorization guidance and Andrew Mark for assisting in modeling beam profiles. I

also thank Dr. Theresa Jones for discussions on YFP imaging and Dr. Boris Zemelman for fruitful discussions on fluorescent proteins. I thank Dr. Scott Aaronson for provocative discussions on the role of quantum mechanics in the brain. I thank Dr. Andrew Fowler for assistance with making Ruthenium micelles. I thank Dr. Lisa Richards for offering her immense knowledge on Speckle imaging, as well as Colin Sullender, Chakameh Zahedkargaran, and Jeremy Arkin. I also thank the undergraduates who worked with me: Kristen Hagan for helping to process data and building the autocorrelator and its software, Alex Brown for modeling the depth limits of multiphoton microscopy, and Grace Jiang for building a 3D vasculature model. I thank Julie Strickland and Dr. Janet Zoldan for collaborating on vessel regrowth with pluripotent stem cells. I am incredibly grateful to Dr. David Boas, Dr. Sava Sakadžić, and Dr. Abbas Yaseen for making my time at Harvard/MGH an impactful experience; your wide perspective on brain imaging applications helped spark my interest in brain decoding.

The research in this thesis is supported by the good-natured, hard-working folks at the National Institutes of Health [NS082518, NS078791, EB011556]; the American Heart Association [14EIA18970041]; the Cancer Prevention and Research Institute of Texas [RR160005]; and The University of Texas at Austin. I am especially thankful to the National Science Foundation Graduate Research Fellowship Program [DGE-1110007] for funding me during my doctoral research.

# *In Vivo* Optical Imaging to Investigate Neurovascular Structure and Cerebral Hemodynamics

David Roger Miller, Ph.D.
The University of Texas at Austin, 2018

Supervisor: Andrew K. Dunn

The ability to visualize structural features of the brain and associated functional information has fueled a revolution in our understanding of the brain. The optical technique two-photon microscopy (2PM) is widely used to study individual neural circuits and blood vessel networks *in vivo* because it is minimally invasive and provides three-dimensional images with cellular resolution. There is rising interest from neuroscientists for the ability to extend the traditional imaging depth of 2PM, which is typically limited to $\sim$500 $\mu$m below the surface of the brain.

In this dissertation, I detail the development of a novel laser source that enables deep-tissue *in vivo* multiphoton microscopy imaging of blood vessel networks and neurons. Using an excitation wavelength near 1,300 nm at which scattering in tissue is minimized, I demonstrate the ability to chronically study vascular morphology and dynamics as well as neuron morphology at imaging depths of 1 mm and beyond.

# Table of Contents

# List of Tables

# List of Figures

# Chapter 1

# Introduction

The quest to understand consciousness is a natural progression of human intelligence attempting to make sense of itself. The path to understanding consciousness started in the abstract, finding a strong foothold in philosophical debate. Many renown philosophers were also scientists attempting to quantify the universe around them. Today, the pursuit of consciousness has moved beyond the theories of early philosophers and scientists to experimental inquiries into the brain. I feel immensely privileged to be conducting brain research in an age in which new brain imaging capabilities are not only being developed in laboratories but also deployed in human clinics. Moreover, a broad community of scientists, engineers, philosophers, and medical doctors are coming together in unprecedented collaboration to unpack the mysteries of the brain. In this dissertation, I focus on the physics and engineering research I conducted and how its findings improve our understanding of the brain.

developed the microscope and laser instrumentation, designed and performed the experiments, analyzed the data, and wrote the manuscript; and adapted from "Deep tissue imaging with multiphoton fluorescence microscopy," Vol 4, pp. 32–39, Copyright (2017) with permission from Elsevier [12] for which David Miller performed the literature search, developed the model for Fig. 1 in the article, and wrote a majority of the manuscript.

## 1.1 The Brain

The human brain is a fascinating and complex feat of biology consisting of some 86 billion neuronal cells that are linked by 100 trillion connections [13]. To sustain healthy function of the myriad neurons, the brain requires a constant supply of energy - mainly oxygen - that is delivered through a dense network of blood vessels. Blood flow and neural activity are intricately linked through a process called neurovascular coupling in which cerebral blood flow is regulated by the energy demands of neural activity. Via neurovascular coupling, blood flow serves as the bridge between microscopic interactions of brain cells and macroscopic behavior. Regulation of blood flow and the oxygen it delivers is critical as brain cells are particularly vulnerable to hypoxia, which can lead to cell death manifesting as cognitive deficits. *Stroke* is the colloquial term for a lack of oxygen to a brain region. Roughly 795,000 strokes occur in the United States annually [14], resulting in 140,000 deaths [15] - making stroke the fifth leading cause of mortality in the U.S. and the leading cause of adult disability. A stroke is unexpected, has devastating results for victims

and loved ones, and currently has no long-term treatment. The aim of this thesis is to shed light on the dynamics of cerebral blood vessel networks and the neurons they sustain in order to provide insights for future treatments and diagnostics of brain diseases such as stroke.

## 1.2 Brain Imaging Modalities

The development of new techniques capable of rapid, three-dimensional imaging of the brain has fueled rapid advances in brain imaging. The difficulty in understanding the brain is that it operates at numerous spatial levels from molecules to integrated circuits. At the molecular level on the spatial scale of nanometers, ions are the root for neural activity. At the individual cellular level, these ions control the firing of neurons, which have cell bodies on the order of microns. Blood vessels range in size from microns in capillaries to millimeters in large feeding and draining vessels. Neuron axons can extend meters in length. Moreover, temporal dynamics similarly range in scale. A plethora of techniques exist to resolve the various spatial and temporal levels important to brain operation. Ideally, one imaging modality could visualize both small and large features of the brain at any location in the brain. Unfortunately, there is a trade off between spatial resolution and imaging depth as shown in Fig. 1.1. One metric for the utility and maturity of an imaging modality is that its spatial resolution should be 1000 times better than its imaging depth. Magnetic Resonance Imaging (MRI) can obtain 3D images of the entire brain but is limited to a spatial resolution of 1 mm. Ultrasound has an imaging depth on

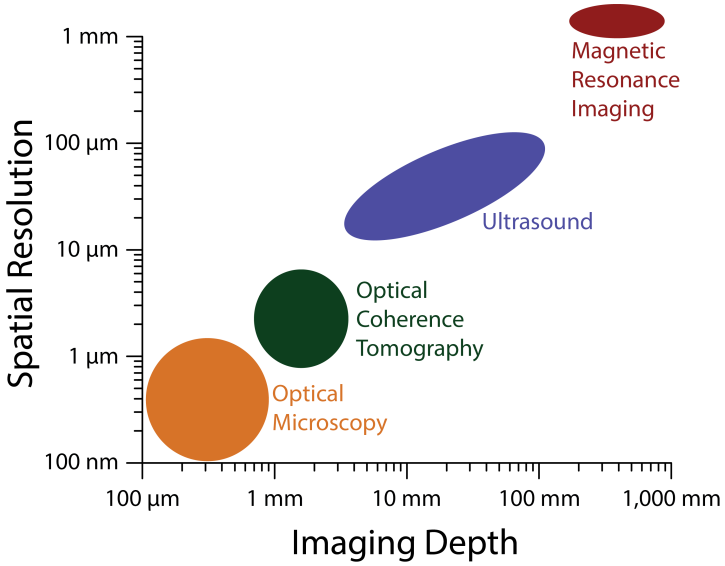


Figure 1.1: *In vivo* brain imaging modalities spatial resolution versus imaging depth. Image adopted from Fujimoto and Drexler [1].

the order of tens of millimeters and has a spatial resolution on the order of tens of microns. Optical coherence tomography (OCT) has an imaging depth on the order of microns and spatial resolution on the order of millimeters. Optical microscopy has an imaging depth exceeding 1 mm (as demonstrated in this dissertation) and spatial resolution on the order of microns. All four modalities are useful for studying various spatial extents of the brain. While MRI is revolutionizing the study of functional interconnectedness throughout the brain, it cannot observe an individual neuron. This dissertation focuses on optical microscopy for its ability to visualize single neurons and blood vessels. The limitation of optical microscopy is its imaging depth. I will describe these limitations in detail and demonstrate ways to extend the imaging depth.

## 1.3 Optical Imaging

Optical imaging uses light to probe and investigate a sample. Optical imaging has a broad range of applications, most notably to study living things. The principle of optical imaging is to manipulate the properties of light to discern information about a sample - whether that sample is a molecule, cell, tissue, or organ. To understand optical imaging and its advantages over other imaging modalities, we first must understand the unique properties of light, particularly laser light. Light is an electromagnetic wave as demonstrated by James Maxwell in the 1860's. Maxwell developed a theory for electromagnetic waves culminating in a set of equations termed "Maxwell's equations" which are derived in Appendix A. Based on Maxwell's theory for electromagnetism, we can describe light as having a wavelength $\lambda$, frequency $f$, energy $E$, and speed $v$. The speed of light can be described by

$$v = f\lambda, \tag{1.1}$$

where the speed is assumed to be from the reference of the medium in which the light is traveling. It is important to note that the medium in which light is traveling affects its speed. In vacuum, light travels at $v = c = 299{,}792{,}458$ meters per second. The index of refraction, $n$, relates the speed of light in vacuum to other media: $n = c/v$. Light travels slower in media with higher indices of refraction. Interestingly, speed is also dependent on the wavelength of the light, thus red light travels faster than blue light. This will be discussed later in detail as ultrafast laser pulses are comprised of a spectrum of wave-

lengths, thus the redder portion of the wave packet will lead the bluer portion in non-vacuum media.

In the late 1800's, Max Planck noticed a discrepancy in the implications of Maxwell's theory of electromagnetism. Planck observed that the experimental measurements of the distribution of energy from blackbody radiation disagreed with the predictions of classical physics. Classical physics was rooted in the idea that light was an electromagnetic wave. To remedy the discrepancy, Planck proposed the revolutionary notion that light is emitted in quantized amounts. The smallest quanta of energy is referred to as Planck's constant $h$. We can relate energy, which is traditionally used to describe a particle, and frequency, which is traditionally used to describe a wave, through Planck's constant:

$$E = hf. \tag{1.2}$$

This is referred to as Planck's equation and serves to bridge the gap between the classical electromagnetic theory of light as a wave and the quantum mechanical description of light as a particle.

In 1905, Einstein used Planck's idea to explain the photoelectric effect which refers to the emission of electrons from a surface when illuminated with light. Einstein explained that there is a minimum quanta of energy, or photon energy, required to eject an electron from a surface; the photon energy must be greater than the energy binding the electron to the surface. The photoelectric effect is vital for the detection scheme in multiphoton microscopy systems.

Both of light's wave and particle characteristics make it unique for imaging applications. Particularly useful for biological imaging applications is laser light. Laser stands for "**L**ight **A**mplification by the **S**timulated **E**mission of **R**adiation." Lasers are typically characterized as illustrating three properties. One, laser light is coherent meaning the electromagnetic wave is in phase in both time and space. Second, laser light is directional, meaning the wave is traveling in a highly collimated manner. This is in contrast to sources of light such as the sun or a light bulb which emit light isotropically instead of in a single direction. And third, laser light is typically monochromatic meaning the electromagnetic wave has a single wavelength. For example, a helium-neon laser emits light at 632.8 nm which the human eye perceives as red. However, laser light does not have to be monochromatic. Ultrafast lasers, which are required for multiphoton excitation, emit short pulses of light that contain a spectrum of wavelengths. Many optical imaging techniques attempt to visualize features on the microscopic scale. This branch of optical imaging is referred to as optical microscopy. The characteristics of coherence and collimation enable laser light to be focused down to a small focal spot and gather information about samples on the microscopic level.

## 1.4 Multiphoton Microscopy

Optical microscopy offers non-invasive, high-resolution *in vivo* techniques to observe intact brain tissue and its surrounding environment with cellular resolution. Traditional fluorescence microscopy, including confocal

microscopy, using one-photon excitation is limited to imaging the superficial tissue surface due to the scattering of short excitation wavelength light in heterogeneous brain tissue. To overcome depth limitations, nonlinear multiphoton excitation is widely used. Two-photon fluorescence microscopy (2PM), developed in the 1990's [16], is the most widely adopted method for minimally invasive *in vivo* brain imaging due to its ability to image in three dimensions. Recent *in vivo* imaging of neuronal circuits [17–19] and vascular networks [20,21] in the brain with micron scale resolution has revealed significant new insight into cortical function and organization. Three-dimensional multiphoton imaging is possible because of a nonlinear dependence on excitation intensity, which confines two-photon fluorescence generation to the focal volume [22]. The resulting imaging depth is significantly greater than in confocal fluorescence microscopy due to the longer excitation wavelength [23] and the ability to detect multiply scattered emission photons. However, the imaging depth for most 2PM imaging studies is around 500 $\mu$m, which is sufficient to image superficial cortical layers in rodent experiments. This limitation on penetration depth arises from light scattering and absorption of tissue, both of which are wavelength dependent.

2PM is certainly the most common non-unity order excitation used in microscopy, however higher order excitations are also possible. Three-photon excitation has certain advantages over two-photon excitation such as improved localization of the emitted fluorescence [23]. I will use the term multiphoton microscopy (MPM) to collectively refer to fluorescence microscopy using two-

photon or three-photon excitation, or any higher order excitation.

A MPM image is formed by scanning a focused laser beam across a sample as fluorescence is detected. MPM requires ultrafast lasers to generate sufficient photon density to cause multiphoton excitation. Traditional 2PM relies on Ti:Sapphire (Ti:S) lasers because of their ability to output mode-locked ultrafast pulses with high average powers, and their ability to excite a variety of fluorophores with one-photon absorption peaks in the visible range. Due to their reliability and robustness, Ti:S lasers have served as the workhorse of 2PM for the last 25 years and are commercially available from multiple laser companies as turn-key systems. Ti:S oscillators typically have a maximum pulse energy of 20 nJ (1.5 W average power at repetition rate of 76 MHz) and temporal pulse widths around 100 femtoseconds (fs). Ti:S oscillators provide a tunable excitation wavelength between 700 and 1,000 nm, which covers the peak two-photon absorption of a myriad of common fluorophores thus contributing to the popularity of Ti:S oscillators. 2PM performed with Ti:S oscillators has been shown to reach a maximum imaging depth of 800 $\mu$m in the neocortex [22]. While 2PM with Ti:S lasers substantially increases imaging depth relative to other optical microscopy approaches like confocal microscopy, Ti:S lasers are not optimized for deep imaging. To push the imaging depth further and visualize the entire mouse cortex (which is about 1 mm thick) and beyond, many new tools have been developed.

To appreciate the recent development of tools that extend the imaging depth of 2PM, it is important to understand that the optical properties of

the biological sample serve as the fundamental limiting factors for imaging depth. Both excitation light and emission light are attenuated by absorption and scattering in biological tissue. Scattering and absorption effects vary by wavelength; thus, approaches to extend imaging depth focus on optimizing the excitation wavelengths, emission wavelengths, or a combination of both. The development of longer wavelength laser sources aims to reduce the scattering of excitation light. The advent of brighter fluorophores aims to both increase the amount of excitation light absorbed by the fluorophore as well as increase the likelihood that the fluorophore emits a fluorescent photon after absorption, and red-shifted fluorophores reduce the scattering effects of the emission light.

## 1.5 Tissue Optical Properties

Scattering and absorption, characterized by the scattering coefficient ($\mu_s$) and the absorption coefficient ($\mu_a$), respectively, impact imaging depth by attenuating both the excitation laser light and emitted fluorescence, ultimately reducing the number of signal photons that reach the detector. The amount of scattered light decreases with increasing wavelength; however, absorption due to water increases significantly near 1,500 nm and beyond 1,800 nm. Figure 1.2 illustrates this wavelength-dependent effect by showing the normalized fraction of photons (blue line) that reach a depth of 1 mm for wavelengths from 700 to 2,400 nm. Any scattered excitation light does not contribute to the multiphoton absorption process, so the fraction of photons of wavelength $\lambda$ reaching a depth $z$ can be modeled as $\exp[-(\mu_a(\lambda)+\mu_s(\lambda))z]$. The

wavelength dependence of absorption is governed by water absorption, while the wavelength dependence of scattering is significantly more complex and difficult to measure, but is commonly approximated as $\mu_s(\lambda)=a/(1\text{-}g)(\lambda/500)^{-b}$, where $g$ is the scattering anisotropy and is usually assumed to be approximately 0.9 for biological tissues [2]. Under this approximation, the scattering coefficient is determined by the values of $a$ and $b$, which can vary considerably, even for brain tissue [2]. The scaling factor $a$ and scattering power $b$ are parameters used to characterize the scattering coefficient.

Figure 1.2 illustrates the contributions of scattering and absorption in biological tissue. The solid blue line is calculated using average values for brain optical properties (g=0.9, a=1.1 $mm^{-1}$, b=1.37, water content=75%) [2]. The plot demonstrates that 15 times more photons reach a depth of 1 mm using a wavelength of 1,300 nm versus 800 nm, and 1.8 times more photons at 1,700 nm versus 1,300 nm. There is an additional peak near 2,200 nm, however, it is in a red shaded region indicating that more than 50% of the photons are absorbed by tissue. Although scattering and absorption attenuate photons with equal magnitude from a physics perspective, they are not equal from a physiological perspective. Excessive absorption is harmful to biological samples because it causes tissue heating. Wavelength regions in which greater than 50% of photons are absorbed may not be viable for deep imaging without significant cause for concern due to excessive heating of tissue; thus, the peak at 2,200 nm is not feasible for deep imaging. However, the peaks near 1,300 nm and 1,700 nm are viable and are the optimal wavelengths for deep imaging. At

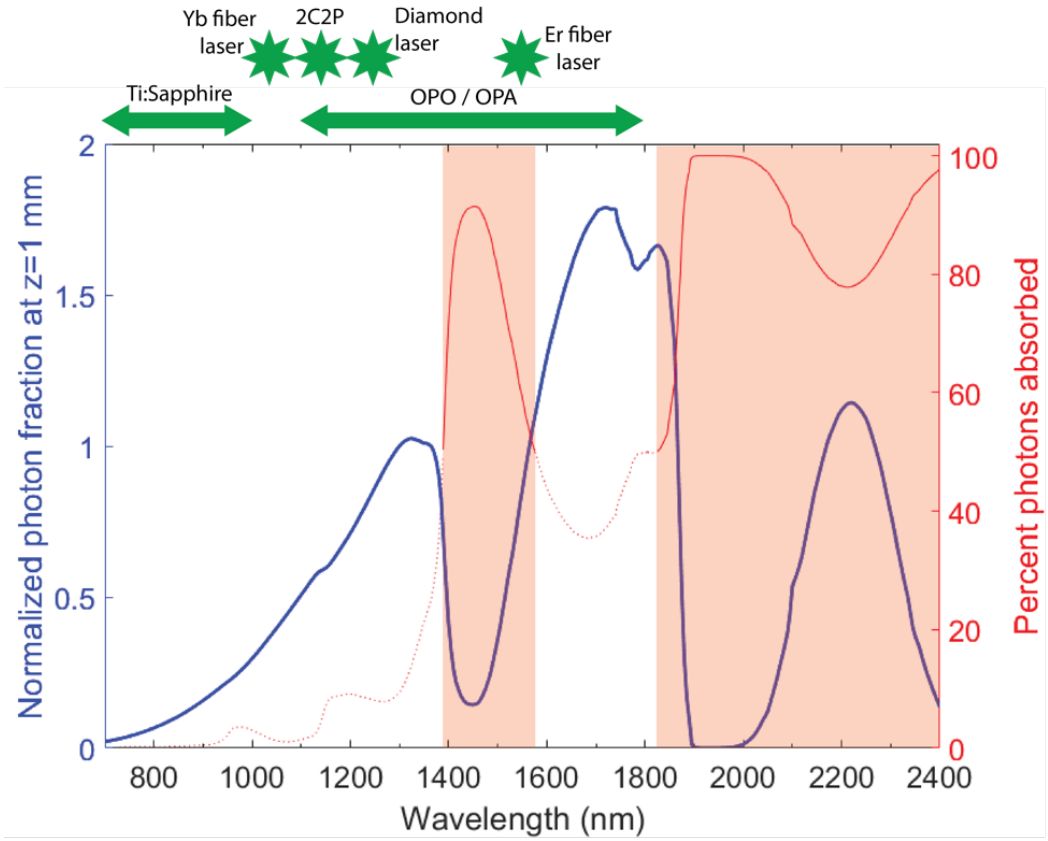


Figure 1.2: **Effects of scattering and absorption**. Photon fraction at a depth of 1 mm for average brain tissue optical properties (g=0.9, a=1.1 mm-1, b=1.37, water content=75%) [2] is demarcated by the blue line. Regions shaded in red indicate areas in which 50% or more of photons are absorbed, as calculated by the red line (dashed red indicates below 50%; solid red indicates over 50%). Available laser options are outlined for their respective wavelength range (Yb = ytterbium, 2C2P = two-photon two-color of Yb fiber laser and diamond laser, Er=Erbium, OPO=optical parametric oscillator, OPA=optical parametric amplifier).

1,300 nm, conventional fluorophores may undergo two-photon or three-photon excitation depending on the fluorophore absorption characteristics, whereas most fluorophores undergo three-photon excitation at 1,700 nm.

## 1.6 Laser sources for multiphoton microscopy

Multiphoton excitation requires high peak power to significantly increase the probability that a molecule will absorb two or more photons simultaneously. To obtain high peak power, ultrafast lasers are used which output pulses on the order of 100 fs. To understand the theory underlying how ultrafast pulses are generated, see Appendix B.

Ti:S lasers have dominated the 2PM field because they reliably produce wavelength-tunable ultrafast pulses with high average power. Modern Ti:S lasers are robust, turn-key systems that enable routine 2PM imaging; however, they are not the optimal source for deep imaging within biological tissue. The imaging depth for most 2PM imaging studies is around 500 $\mu$m, whereas the mouse cortex is about 1 mm thick. There is a large push from neuroscientists for the ability to chronically image the entire mouse cortex in order to better understand the circuitry of neural circuits and the blood vessel networks that supply neural circuits with energy. Many neurological disorders have a neural and vascular basis.

There are several approaches to increase imaging depth by reducing the effects of scattering in brain tissue while avoiding deleterious water absorption regions. A recent approach, adopted from astronomy, is the use of adaptive optics to shape the wavefront of excitation light to overcome tissue scattering [24]. An imaging depth of 700 $\mu$m was reached in mouse cortex using adaptive optics [25]. Another approach is to increase the pulse energy of a laser source such that a greater number of photons per pulse penetrate to

deeper tissue. Ti:S lasers typically produce pulse energies on the order of 10 nJ for repetition rates around 80 MHz. Using a Ti:S laser as a seed for a regenerative amplifier, pulse energies on the order of microjoules can be attained for repetition rates between 100-500 kHz. Using a regeneratively amplified Ti:S laser at a wavelength of 925 nm and repetition rate of 200 kHz, Theer et al. (2003) achieved an imaging depth of 1 mm [26]. A third approach to deep *in vivo* imaging is to use longer excitation wavelengths for which scattering effects are not as significant. Ti:S lasers typically have a wavelength maximum near 1,000 nm. An optical parametric oscillator (OPO), typically pumped by a Ti:S laser, offers a tunable wavelength range from ∼1,000 nm to 1,600 nm and beyond in some setups. Kobat et al. (2011) demonstrated an imaging depth of 1.6 mm using an OPO at 1,280 nm with a pulse energy of 1.5 nJ [27]. A fourth approach is to utilize a long wavelength source with high pulse energy. To achieve wavelengths near 1,700 nm with high pulse energy, Horton et al. (2013) pumped a photonic-crystal rod with a 1,550 nm erbium fiber laser to soliton self-frequency shift the wavelength to 1,675 nm [23]. The output soliton had a pulse energy of 67 nJ, with which Horton et al. demonstrated an imaging depth of 1.4 mm. Ouzounov et al. recorded spontaneous activity from GCaMP6-labeled neurons in the hippocampus at a depth of 1 mm using a noncolinear optical parametric amplifier at 1,300 nm with a 1,250 nJ pulse energy (400 kHz repetition rate) [28].

Driven by advances in fiber laser technology, there are many turn-key systems that provide longer excitation wavelengths. Common systems include

ytterbium fiber lasers ($\lambda$ = 1,030 - 1,070 nm, pulse energy = 1 nJ - 40 $\mu$J, repetition rate = 500 kHz - 100 MHz) as well as fiber-laser-pumped optical parametric oscillators ($\lambda$= 1,000 - 1,600 nm, pulse energy = 1 nJ - 1 mJ, repetition rate = 1 kHz - 80 MHz) and optical parametric amplifiers ($\lambda$ = 1,000 - 1,600 nm, pulse energy = 10 nJ - 10 $\mu$J, repetition rate = 1 kHz - 10 MHz). These systems are being widely adopted for neuroscience investigations due to their reliability and increased imaging depth capabilities.

In this dissertation, I will detail the construction and results of an optical parametric amplifier (OPA) system. I take the approach of using both high energy pulses and longer excitation wavelength with an increased laser repetition rate to achieve fast image acquisition throughout the entire mouse cortex.

## 1.7 Availability of Fluorophores

The discovery and development of bright, biocompatible contrast agents that excite at longer wavelengths is a crucial aspect to the advancement of *in vivo* MPM [29]. Fluorophores that excite near 1,300 nm or 1,700 nm are of particular interest due to minimal absorbance by water and reduced scattering. Exogenous fluorophores used for MPM can be categorized in two groups: organic and inorganic contrast agents [30]. The former class encompasses conventional organic dyes such as Texas red, fluorescein, and Indocyanine green, which are extremely popular due to minimal aggregation issues and low cytotoxicity [31]. However, it is difficult to control the excitation and emission

wavelengths of these dyes since their spectra are dependent on their chemical structure. In addition, fluorescent dyes commonly exhibit low quantum yields in aqueous environments, which reduces brightness in biological settings [30]. The latter category, inorganic probes, includes the well-established quantum dot, bright fluorescent semiconductor nanocrystals with broad absorption and discrete, tunable emission wavelengths that are highly resistant to photobleaching [32, 33]. Recently, the polymer dot has emerged as an even brighter, comparable alternative to quantum dots with decreased cytotoxicity [34–36]. Endogenous fluorescent proteins (FPs) offer a viable alternative to both organic and inorganic external contrast agents and can be used to label specific structures either by functionalization or genetic encoding. The selection of an appropriate FP for an imaging experiment involves careful consideration of factors such as brightness, photostability, and specificity [37]. In the past, the adoption of far-red variants of FPs has been obfuscated by their low brightness, but mKate, the pseudo-monomeric tdKatushka2, and td-Tomato collectively represent a new generation of bright, far-red emitters with substantial potential for deep *in vivo* imaging [38, 39]. Figure 1.3 summarizes the peak two-photon absorption cross sections of various fluorophores reported in the literature.

Importantly, a probe can provide functionality beyond simply providing contrast; for instance, more sophisticated fluorescent sensors can be used to report on oxygen distributions*in vivo* [40, 41] or monitor the activity of distinct neurons in brain tissue [42]. Indicators of neuronal activity rely on

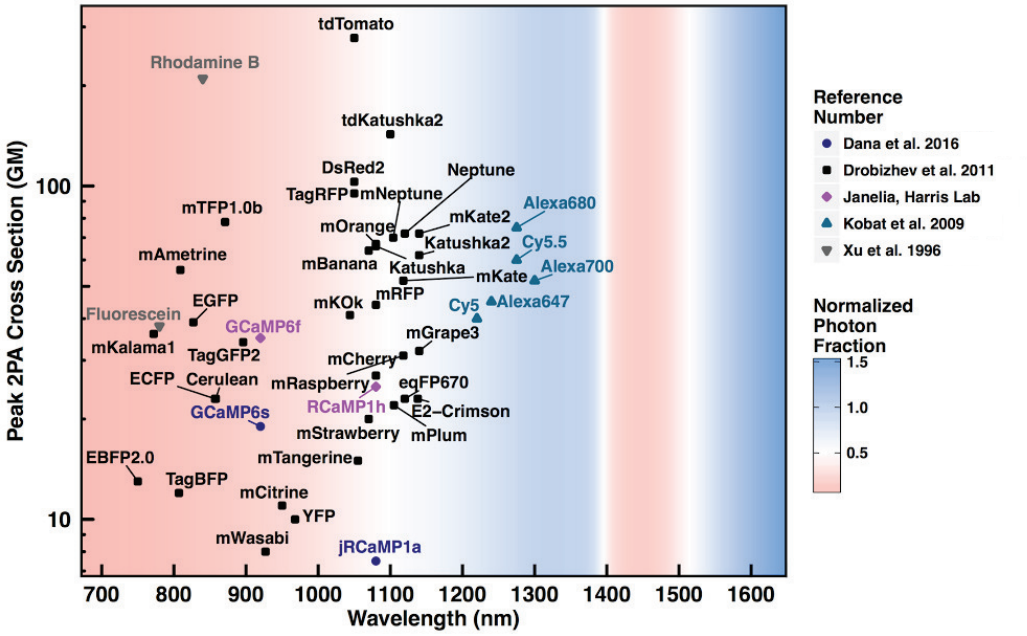


Figure 1.3: **Cross Sections of various fluorophores.** Peak two-photon absorption cross sections of common fluorophores compiled from published literature. Dark blue circles are from Dana et al. (2016) [3], black squares are from Drobizhev et al. (2011) [4], pink diamonds are from Janelia Harris [5], teal triangles are from Kobat et al. (2009) [6], and gray inverted triangles are from Xu et al. (1996) [7]. The calculated normalized photon fraction of excitation light that reaches 1 mm into brain tissue (normalized to 1300 nm, analogous to Figure 1.2 solid blue line) is overlaid as background fill, where the color scale ranges from 0.01 (red) to 0.5 (white) to 1.6 (blue).

sensitivity to calcium ions (a proxy for action potentials), membrane potentials, or neurotransmitters [43]. In particular, genetically encoded calcium indicators (GECIs) have garnered attention and popularity within the neuroscience community despite challenges related to rapid calcium dynamics and low peak calcium accumulations [44]. Advances in protein engineering, structure based-design, and mutagenesis has produced a family of ultrasensitive

protein calcium sensors (GCaMP6) that vastly outperform other indicators in terms of both sensitivity and reliability [45–47]. These sensors can be used to visualize large groups of neurons in addition to smaller synaptic protrusions, and remain stable for months [48]. The GCaMP6 family will undoubtedly be used to answer significant questions in neuroscientific research and recent work has even enabled functional imaging of the hippocampus at a  1 mm depth in mice [28]. Nevertheless, optimization of red GECIs has not kept pace with GFP-based designs and future research efforts will hopefully continue to improve the properties and application of these sensors [49].

Regardless of their function, characterization of the nonlinear properties of existing contrast agents to determine their compatibility with longer-wavelength excitation sources is a crucial first step towards their adoption as probes for MPM. There is a myriad of properties by which one can evaluate fluorophores, but action cross-section measurements, a product of absorption cross-section and quantum yield, are a particularly useful metric to evaluate brightness [50]. Unfortunately, accurate determination of cross-sections is a complicated endeavor that requires detailed information of the spectral properties of a chromophore, sample concentration, and a well-characterized standard [4,51]. As a result, the nonlinear properties of very few fluorophores have been reported, and in those limited instances, analysis has been limited to non-physiological solvents at wavelengths below 1,300 nm [52–56]. This wavelength limitation is in part due to the absence of reliable longer wavelength, ultrafast laser systems; however, given recent technological advances, two-photon and

three-photon cross section measurements near 1,300 nm and 1,700 nm are now achievable. Thus, the MPM community is engaged in a broad push to report cross-section values at higher order regimes in order to take full advantage of the potential of available contrast agents and optimize experimental designs. Recent work has demonstrated three-photon imaging of Texas Red and RFP at 1,700 nm [23], three-photon cross section measurements of fluorescein ($\lambda$ = 1,300 nm), wtGFP ($\lambda$ = 1,300 nm), Indocyanine green ($\lambda$ = 1,550 nm), and SR101 ($\lambda$ = 1,680 nm), and four-photon cross section measurements of fluorescein ($\lambda$ = 1,680 nm) and wtGFP ($\lambda$ = 1,680 nm) [10, 57]. Simultaneous efforts have focused on the development of compounds with enhanced multiphoton properties [58]. In addition, improved red-shifted calcium indicators with advantages for deep *in vivo* imaging are being designed to rival the sensitivity of GCaMP6 [3]. Together, the characterization of existing contrast agents and the development of novel chromophores for MPM will identify and produce probes that are sufficiently bright and photostable to overcome background fluorescence and scattering *in vivo*.

In this dissertation, I investigate the properties for the fluorophores Texas Red, Indocyanine Green, Fluorescein, Rhodamine B, Ruthenium, and YFP.

## 1.8 Quantum Theory in Multiphoton Microscopy

Multiphoton microscopy depends on a fluorophore undergoing multiphoton absorption, and the emitted fluorescence of that fluorophore reaching

a detector. Multiphoton absorption occurs when a single molecular fluorophore absorbs multiple photons simultaneously. Albert Einstein first theorized multiphoton absorption in his 1905 paper "Concerning an Heuristic Point of View Toward the Emission and Transformation of Light" [59]. In this paper, Einstein proposed that light was quantized to explain the photoelectric effect, for which he received the Nobel Prize in Physics in 1921. In the paper, Einstein proposes multiphoton absorption when considering deviations from Stokes's Rule:

> ... deviations from Stokes's Rule are conceivable in the following cases:
>
> 1. when the number of simultaneously interacting energy quanta per unit volume is so large that an energy quantum of emitted light can receive its energy from several incident energy quanta; (Einstein 143)

Einstein recognized that the emitted fluorescence wavelength of an atom solely depends on the final electronic state of the atom after the excitation process, not the intermediate states. Einstein built on this concept to generalize how an atom can transition between electronic states. In his 1916 paper "Emission and Absorption of Radiation in Quantum Theory," Einstein makes the assumption that an atom has two defined electronic states during a transition [60], which deviated from the classical physics view that an atom oscillated between different states [61]. Einstein pioneered quantum theory by

explaining that an atom is either in the ground state or the excited state, and that there are three ways for an atom to transition between the ground and excited state, depicted in Fig. 1.4. The first is for an atom to transition from

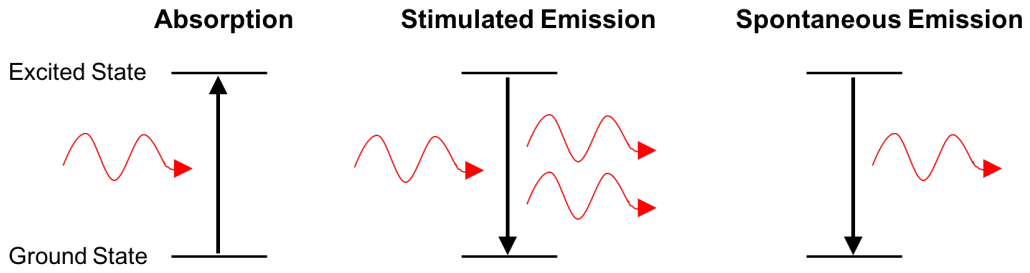


Figure 1.4: The three radiation methods for an atom transitioning between the ground and excited state: absorption, stimulated emission, and spontaneous emission. Each red wave indicates a single photon.

the ground state to the excited state by absorbing a photon equal to the energy gap between the states - this is termed *absorption*. The second is for an atom to transition from the excited state to the ground state upon incidence of a photon equal to the energy gap between the states - this is termed *stimulated emission*. The atom emits a photon equal in energy, direction, phase, and polarization of the incoming photon. Stimulated emission is the underlying principle behind lasers as it enables the amplification of coherent light. The third transition is again from the excited state to the ground state but without the presence of an incoming photon - this is termed *spontaneous emission* or fluorescence. I note here that Einstein applied these principles to individual atoms, but the concept can be generalized to molecules. Atoms have individual quantized energy levels, while molecules have energy bands which contain

a range of energy levels. Thus, we can refer to both atoms and molecules as having energy levels, albeit atoms have quantized energy levels.

Each of these three processes plays a role in developing the theory for multiphoton microscopy.

### 1.8.1 Multiphoton Absorption

Multiphoton absorption occurs when a molecular fluorophore absorbs more than one photon simultaneously. This process is depicted in a Jablonski diagram in Fig. 1.5. In the Jablonski diagram, the ground state $S_0$ and excited state $S_1$ are depicted by horizontal solid lines vertically offset to indicate an energy gap. Virtual states are indicated by dotted horizontal lines. In one-photon absorption, a molecule absorbs a photon of energy $E_1$ and transitions from the ground state to the excited state. For most common fluorophores, this energy corresponds to a wavelength in the visible spectrum. For the sake of example, let us say the molecule absorbs a photon of wavelength $\lambda_1 = 400$ nm or equivalently $E_1 = 3.10$ eV. In two-photon absorption, a molecule absorbs two-photons simultaneously. Each photon must have an energy $E_2$ half of $E_1$ to undergo the same transition as absorbing a single photon of energy $E_1$ (assuming degenerate two-photon absorption). Thus, in our example $\lambda_2 = 800$ nm or equivalently $E_2 = 1.55$ eV. In three-photon absorption, a molecule absorbs three-photons simultaneously. Each of the three photons must have an energy $E_3$ that is a third of $E_1$ to undergo the same transition as absorbing a single photon of energy $E_1$ (assuming degenerate three-photon absorption). So,

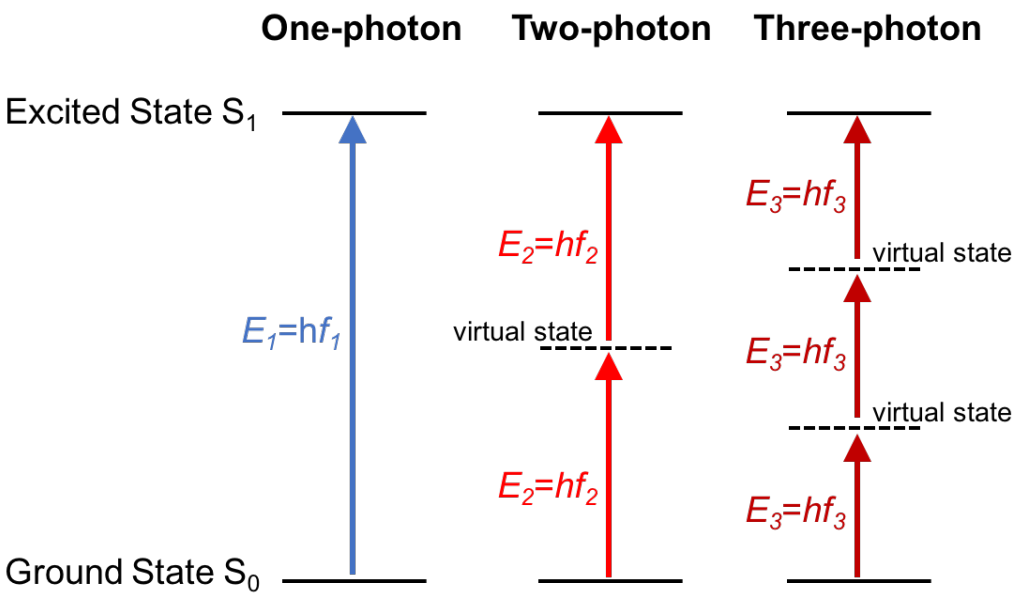


Figure 1.5: Jablonski diagram for one-photon, two-photon, and three-photon absorption. In one-photon absorption, a single photon of energy $E_1$ is absorbed. In two-photon absorption, two photons both of energy $E_2$ are absorbed simultaneously by the same molecule, where $E_1 = 2E_2$. In three-photon absorption, three photons each of energy $E_3$ are absorbed simultaneously by the same molecule where $E_1 = 3E_3$.

in our example $\lambda_3 = 1200$ nm or equivalently $E_3 = 1.03$ eV. It is important to note that in our example, the molecule enters the same excited state regardless if absorbing a single photon of energy $E_1$, two photons of energy $E_2$, or three-photons of energy $E_3$. Thus, the emitted fluorescent photon would be the same in each situation; the only difference is the mechanism for the molecule to reach the excited state.

It is interesting to consider what "simultaneously" means in this context. In other words, what is the actual timescale for a molecule to absorb

multiple photons and enter an excited state via virtual states. To estimate the time scale for which two photons must interact with a single molecule to both be absorbed to fill an energy gap of their summed energy, we can apply Heisenberg's uncertainty principle which states that

$$\Delta E \; \Delta t = \frac{\hbar}{2} \tag{1.3}$$

where $\Delta E$ is the difference in energy of the electronic transition energy gap and the incident photon energy, $\Delta t$ is the time scale for the photon and molecule interaction, and $\hbar$ is the reduced Planck's constant: $\hbar = h/(2\pi) = 6.582 \times 10^{-16}$ eV·s. For a typical two-photon absorption event, the electronic transition energy gap is within the visible light range and the intermediate state is close in energy to the final state assuming no extreme non-degenerate situations [62]. Thus, the difference in energy of the electronic transition energy gap and the incident photon energy is on the order of 1 eV. Thus, the time scale for which two photons must interact with a single molecule for two-photon absorption to occur is

$$\begin{aligned} \Delta t &= \frac{\hbar}{2 \cdot \Delta E} \\ &= \frac{6.582 \times 10^{-16} \text{ eV} \cdot \text{s}}{2 \text{ (1 eV)}} \\ &\approx 10^{-16} \text{ s} \, . \end{aligned} \tag{1.4}$$

Thus, the time scale is about 0.1 femtoseconds which is why ultrafast lasers are required to efficiently cause two-photon absorption.

Building on Einstein's earlier work, Maria Göppert-Mayer worked out the quantum mechanics in 1931 in her doctoral thesis [63], for which she would

win the Nobel Prize in Physics in 1963 - joining Marie Curie as the only other woman to win the Nobel Prize in Physics. Since multiphoton absorption is an extremely rare process in nature, it was not until the experimental realization of lasers in the 1960's that Göppert-Mayer's predictions could be confirmed. To cause multi-photon absorption, a large amount of photons must be confined in both time and space. Two-photon absorption only occurs about once every 10 million years due to Sunlight, thus ultrafast lasers are used. Göppert-Mayer is honored in MPM by having the two-photon cross section named after her; 1 Göppert-Mayer or 1 GM equals $10^{-50}$ cm$^4$ seconds per photon.

The benefit of multiphoton absorption for MPM is the localization of fluorescence. One-photon excitation is a linear process, meaning the fluorescence is proportional to the intensity. Thus, fluorescence will occur everywhere where the beam is focused. On the other hand, two-photon absorption is a non-linear process, meaning that the fluorescence is proportional to the intensity squared. This is useful because fluorescence is only generated at the focal plane at which the intensity is highest. Therefore, fluorescence from two-photon absorption is inherently three-dimensional; moreover, three-dimensional images can be reconstructed since we know that the fluorescence originated from the focal volume.

Let us revisit the example above to demonstrate the benefit of fluorescence localization in MPM. To confine a high density of photons in time, we will use an ultrafast laser that outputs pulses at 100 fs. To confine the photons in space, we will use a high numerical aperture ($NA$) objective which focuses

the light to a diffraction-limited spot. We will presume that the molecule fluorophore has an energy transition corresponding to $\lambda_1$=400 nm as in the above example and a a two-photon energy transition of $\lambda_2$=800 nm; however, this assumption is not typically valid for two-photon absorption spectra as the quantum selection rules differ for one-photon and two-photon absorption. Figure 1.6 compares the fluorescence from one-photon and two-photon absorption for this example of illuminating a volume of fluorophores with 100 fs pulses at $\lambda_1$=400 nm and $\lambda_2$=800 nm focused by a high $NA$ objective. The confine-

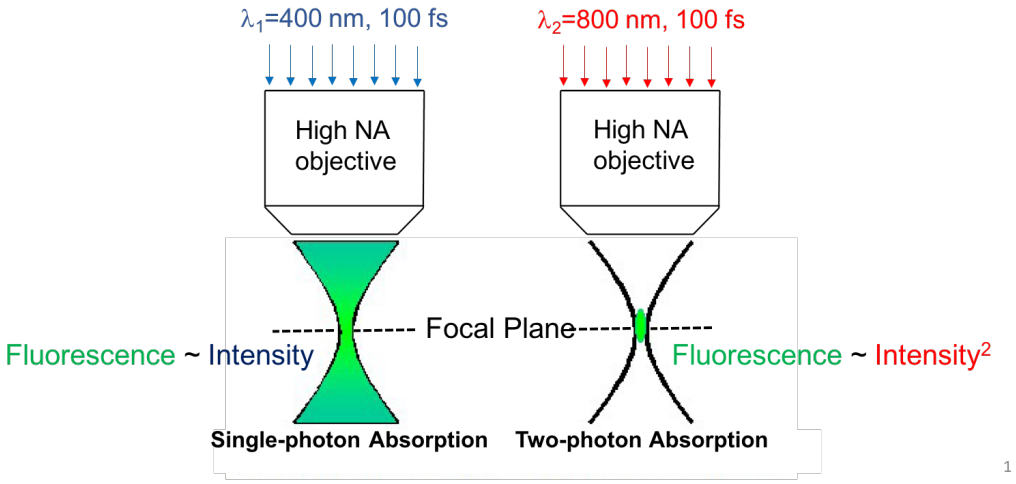


Figure 1.6: Fluorescence generated from single-photon and two-photon absorption. The fluorescence from two-photon absorption is confined to the focal volume, thus enabling three-dimensional imaging in MPM. Image adapted from University of Pennsylvania Two-Photon Center [8].

ment of the fluorescence to the focal volume enables inherent three-dimensional imaging with MPM. Techniques that use single-photon absorption like confocal microscopy must use a pinhole to block the out-of-focus fluorescence which

causes a significant deduction in the amount of signal photons collected, resulting in a reduced imaging depth. Note that using ultrafast excitation light is not sufficient to cause two-photon absorption in the example, the wavelength of the light must also be such that the energy of two photons sums to fill the fluorophore's energy gap.

### 1.8.2 Stimulated Emission

Stimulated emission occurs when a molecule in the excited state drops to the ground state after interacting with a photon equal in energy to the transition between the excited and ground state. The molecule emits a photon equal in energy, direction, phase, and polarization of the incident photon. Through stimulated emission, coherent light can be amplified to create laser light. A gain medium is required to create a laser cavity. The gain medium provides the source of excited molecules to create the cascade of stimulated emission. In Ti:S lasers, the gain medium is a crystal doped with $Ti^{3+}$ ions, which has a large bandwidth that enables Ti:S lasers to be tuned from 600 to 1,100 nm, though the output power falls off at the edges of the spectrum.

### 1.8.3 Spontaneous Emission

Spontaneous emission occurs when an excited molecule *spontaneously* drops from the excited state to the ground state and emits a photon of seemingly random direction, phase, and polarization. For fluorescence, which is a subset of spontaneous emission when the molecule enters the excited state via

absoprtion, the energy of the emitted photon is less than the absorption energy by an amount defined by the Stokes shift. Fluorescence is incoherent and isotropic. The principles of fluorescence are crucial for MPM as the fluorescent photons are collected by a detector to create an image.

We should think seriously about why fluorescence occurs - why does an excited state molecule "spontaneously" drop to the ground state? Claiming that the molecule naturally wants to return to the lowest energy state ignores the mechanism for this process to occur. The mechanism, from a quantum physics perspective, is quantum fluctuations of the ground state energy of the universe, deemed *zero-point energy*. These fluctuations create "virtual" photons that interact with the excited state molecule and cause the molecule to transition from the excited state to the ground state - releasing a photon equal in energy, direction, phase, and polarization of the incident "virtual" photon. With this perspective, fluorescence is merely stimulated emission for which the incident photon is a photon originating from the quantum fluctuations of the ground state energy of the universe.

## 1.9 Overview of Dissertation

In this dissertation, I present routine *in vivo* deep-tissue multiphoton imaging in mouse cortex using an optical parametric amplifier that is tunable between 1,100 and 1,400 nm with an output pulse energy of 400 nJ and a repetition rate of 511 kHz. The tunability of the OPA across a wide spectrum enables efficient excitation of many common fluorophores. I demonstrate deep-

tissue imaging of vasculature labeled with Texas Red, Indocyanine Green, and Fluorescein, and of neurons expressing tdTomato and yellow fluorescent protein (YFP). The combined high repetition rate (511 kHz) and high pulse energy (400 nJ) of the OPA enables fast image acquisition due to the increased signal-to-background ratio (SBR) with a single laser pulse. This allows for entire stacks (even beyond 1 mm) to be acquired with small axial step sizes (5 $\mu$m) to achieve fluid 3D reconstruction of vessels and neurons. Since the brightness of many common fluorophores has not been characterized near 1,300 nm, I measure the cross sections of Texas Red, Indocyanine green (ICG), and Fluorescein across the OPA spectrum to determine their optimal excitation wavelengths, as well as investigate the excitation characteristics of Rhodamine B, Ruthenium, and YFP.

# Chapter 2

# Multiphoton Microscope System Design

As previously discussed, Ti:S lasers are most popular within MPM due to their reliability and robustness. Ti:S lasers can cover the wavelength range from 700 to 1,000 nm. As demonstrated in Fig. 1.2, the optimal excitation wavelength windows for deep imaging are near 1,300 nm and 1,700 nm. This chapter details the design of the optical parametric amplifier (OPA) laser system used for imaging and the optical design of the multiphoton microscope.

Parts of this chapter are adapted from "Deep tissue imaging with multiphoton fluorescence microscopy" Vol 4, pp. 32–39, Copyright (2017) with permission from Elsevier [12] for which David Miller performed the literature search, developed the model for Figure 1 in the article, and wrote a majority of the manuscript; and adapted with permission from David Miller and The University of Texas at Austin from "Extending the depth limit of multiphoton microscopy for in vivo brain imaging" [64] for which David Miller wrote the manuscript and performed the research described within.

## 2.1 Laser Design

An ultrafast OPA has the advantage that it is tunable across a wide spectrum range while maintaining high pulse energy. The spectrum range of the OPA depends on the nonlinear crystal used for parametric amplification. Since longer wavelengths are scattered less in the brain, $\beta$-barium borate (BBO) crystals are desirable for multiphoton microscopy to obtain a tunable wavelength range from 1,100 nm to 1,400 nm. Additionally, BBO crystals have a high nonlinearity promoting more efficient parametric amplification, and have small dispersion effects for ultrafast pulses [65].

An OPA requires intense input pulses on the order of a few microjoules to allow efficient conversion to longer wavelengths in the BBO crystal. This is done by regeneratively amplifying a Ti:S oscillator seed. Regenerative amplifiers typically have a maximum repetition rate of 250 kHz, which also limits the OPA to a repetition rate of 250 kHz. A faster repetition rate enables faster imaging speed, or longer pixel dwell times. This is advantageous for deep imaging of vasculature labeled with fluorescent dyes because the time at which the vasculature contains a high concentration of the dye is maximized. Many dyes will clear quickly which significantly reduces the fluorescent signal and consequently imaging depth. To increase the repetition rate of a standard OPA system, a custom synchronization and delay generator was implemented to control the injection of the Ti:S oscillator seed into the regenerative amplifier. By controlling the injection of the seed pulse with an external clock trigger instead of using a clock derived from the Ti:S oscillator repetition rate,

the regenerative amplifier can operate at a repetition rate up to 511 kHz while maintaining pulse energies above 5 $\mu$J.

During amplification of ultrafast pulses at high repetition rates such as 511 kHz, third-order dispersion becomes an issue. Third-order dispersion is difficult to compensate for in a compressor and causes significant reduction in the efficiency of parametric amplification inside the OPA. In the initial design of the regenerative amplifier, the pulse was stretched during the amplification process by passing through a $TeO_2$ Q-switch which is highly dispersive. The pulse was then compressed by a holographic grating in a 4-pass configuration after amplification. Using this mechanism of stretching and compressing, I observed that doubling the repetition rate of the regenerative amplifier from 250 kHz to 511 kHz also doubled the output power from 1.5 W to 3 W. Thus, I expected the OPA to follow the same trend; however, I observed little increase in the OPA average power at double the repetition rate. Looking at an autocorrelation trace of the regenerative amplifier pulse, it was obvious that the pulse contained third-order dispersion wings, which indicated the pulse was not properly being stretched and compressed. This reduced the photon density at the interaction site in the OPA BBO crystal and consequently reduced the conversion efficiency of the 800 nm input light to longer wavelengths. To reduce the effects of third-order dispersion, the Ti:S oscillator seed pulse was externally stretched by a grating before entering the regenerative amplifier instead of stretching the pulse during each round-trip of amplification inside the regenerative amplifier. This enabled the use of a non-dispersive Q-switch

in the regenerative amplifier that was optimized to handle the bandwidth of the Ti:S oscillator seed, resulting in significantly less third-order dispersion. Additionally, a new grating compressor was installed on a motorized stage which allows the user to minimize third-order dispersion based on the OPA output power.

The OPA laser system is shown in Figure 2.1. A $\lambda$=800 nm mode-locked Ti:S oscillator (Mira 900, Coherent) is externally stretched to seed a regenerative amplifier (RegA 9000, Coherent) that is custom-modified to operate at a tunable repetition rate up to 511 kHz. The seed pulse is amplified to a pulse energy of 6 $\mu$J (average power of 3 W at 511 kHz) and then externally compressed. Next, the compressed 800 nm high-energy pulse is converted to a longer wavelength by an OPA (OPA 9800, Coherent) that is tunable between 1,100 and 1,400 nm with a maximum pulse energy of 400 nJ at 511 kHz. The OPA output is pre-chirped by a pair of prisms before entering the microscope such that the pulse is nearly Fourier-transform limited at the focus of the microscope objective.

## 2.2 Laser Characteristics

To achieve efficient multiphoton excitation, laser pulses near 100 fs or shorter are desirable. The OPA laser system pulse width is dictated by the Ti:S oscillator seed because the seed's bandwidth determines the lowest possible pulse width of the compressed regenerative amplifier pulse. The regenerative amplifier compressed pulse width significantly affects not only the OPA pulse

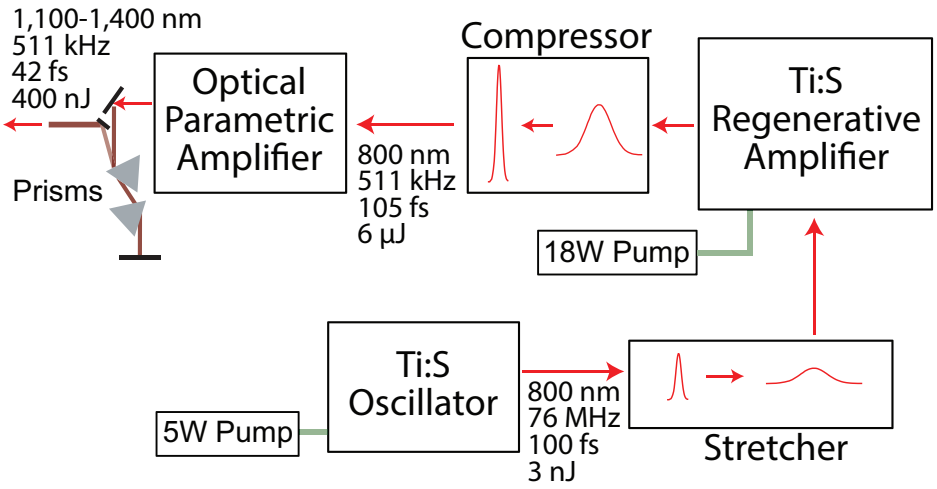


Figure 2.1: The optical parametric amplifier (OPA) laser system. A Ti:S oscillator seeds a regenerative amplifier, which is tunable up to 511 kHz. The amplified pulse is converted to a longer wavelength by the OPA. The OPA output pulse is tunable between 1,110 nm and 1,400 nm and has a maximum pulse energy of 400 nJ at 511 kHz.

width but also the OPA output power as discussed above. The Ti:S oscillator is optimized to operate at the minimum angle of deviation for both of its Brewster prisms to achieve the largest bandwidth. I regularly achieve a bandwidth of 12 nm full-width half-maximum (FWHM) in the Ti:S oscillator, equating to a minimum pulse width of roughly 70 fs after the compressor assuming a time-bandwidth product of 0.4 (in between a Gaussian and hyperbolic secant squared pulse shape). I measured the pulse width after the compressor to be 105 fs, which is approaching Fourier-transform limited.

The laser pulse is then broadened during the wavelength shift process in the OPA. To extend the wavelength, the beam is first tightly focused causing it to undergo self phase modulation which generates a white-light continuum

containing a spectrum from the infrared to the ultraviolet. The ultrafast white light continuum is combined with the 800 nm beam in the OPA BBO crystal. The beams are aligned both spatial and temporally such that they undergo type II phase matching. The BBO crystal angle dictates which wavelength from the white light continuum is selected for amplification. During the white light continuum generation, the pulse undergoes self-phase modulation which broadens the bandwidth of the pulse. After the optical parametric amplification, I measured the pulse to have a bandwidth of 60 nm FWHM and pulse width of 110 fs. A bandwidth of 60 nm FWHM suggests the pulse can be compressed to about 35 fs. Thus, a pair of prisms is placed after the OPA output to further compress the pulse. As the pulse travels from the OPA to the sample inside the microscope, it undergoes dispersion as it interacts with each optical element; most of the dispersion occurs within the microscope objective as it contains numerous optical elements. Thus, the pulse width is measured through the objective via an autocorrelator, and the prism pair is adjusted to achieve the smallest pulse width at the output of the microscope objective; this technique is referred to as "pre-chirping" because the prism pair negatively chirps the pulse to compensate for the positive chirp of the microscope objective. The OPA temporal pulse width, as measured by *in situ* second order autocorrelation [66], at the output of the microscope objective was measured to be $\tau$=42 fs, as shown in Fig. 2.2(a).

Fig. 2.2(b) shows the OPA spectrum used for imaging various fluorophores: tdTomato ($\lambda$=1,140 nm), Texas Red ($\lambda$=1,215 nm), Texas Red and

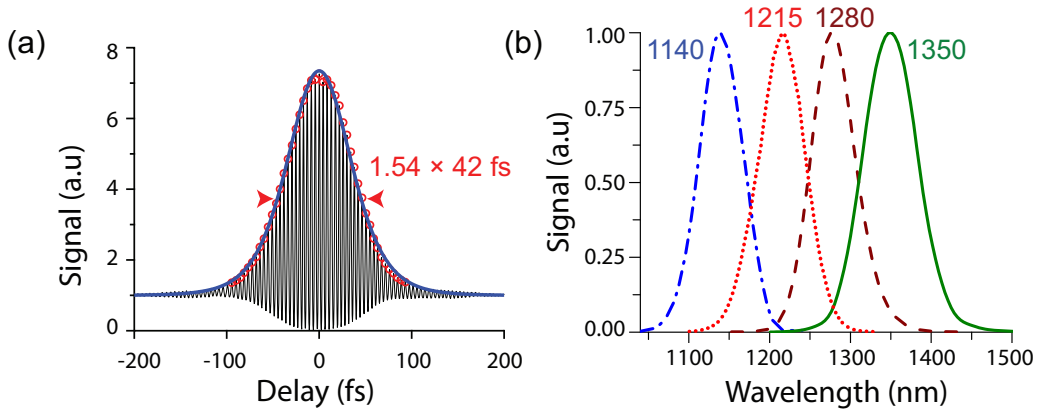


Figure 2.2: **OPA temporal and spectral characteristics.** (**a**) Interferometric autocorrelation trace of the OPA pulse after the microscope objective; red dots indicate peaks of the autocorrelation trace and the blue line is a $\text{sech}^2$(t) fit to the autocorrelation envelope. The measured temporal pulse width of the OPA was $\tau$=42 femtoseconds, calculated by assuming a $\text{sech}^2$ pulse (the autocorrelation width is 1.54 times longer than a $\text{sech}^2$ pulse). (**b**) Spectrum of OPA for imaging tdTomato at 1,140 nm, Texas Red at 1,215 nm, Texas Red and YFP simultaneously at 1,280 nm, and ICG at 1,350 nm.

YFP simultaneously ($\lambda$=1,280 nm), and ICG ($\lambda$=1,325 nm). The OPA can consistently output an average power above 150 mW for the tuning range from 1,140 nm to 1,330 nm, and can operate down to 1,100 nm and up to 1,400 nm with the average power falling off to approximately 50 mW.

## 2.3 Scanning Optics

Before my tenure in the Dunn lab at UT Austin, a custom upright two-photon microscope was built as described in [67]. The microscope optics were designed for Ti:S oscillator excitation wavelengths between 800 and 900 nm, and the microscope was not optimized for large scan angles which resulted

in vignetting when trying to image more than a 400 $\mu$m by 400 $\mu$m area. In preparation for deep-tissue imaging with the OPA, I modified the microscope for longer excitation wavelengths and optimized the scanning optics.

### 2.3.1 Design 1

The previous microscope used a f=20 mm bi-convex scan lens (NIR-coated) and f=125 mm bi-convex tube lens (NIR-coated) to expand the beam by 6X such that the incoming 3 mm laser beam would fill the 18 mm back aperture of the microscope objective. To avoid vignetting, the scan lens was designed to be placed a focal length away from the scanning galvanometer mirrors such that there is no lateral displacement of the expanded beam on the back aperture of the objective. Due to the short focal length of the scan lens, vignetting occurred when scanning over large areas. Additionally, the design was prone to alignment error as the optical path between the galvanometer mirrors and scan lens would vary by about 4 mm, resulting in alignment error up to 20%.

To remedy the problem, I investigated using a longer focal length scan lens. The previous microscope expanded the beam by 6X, however I found that the beam had diverged to a diameter between 4 and 4.5 mm when it reached the galvanometer mirrors, thus only a 5X expansion was needed to back fill the 18 mm aperture. In choosing the focal length of the scan and tube lens, the microscope casing posed a restriction to the amount that the galvanometer mirrors could be raised to accommodate longer focal lengths. I

found that the maximum focal lengths allowed to expand the beam 5X while fitting within the microscope casing was a f=40 mm scan lens and f=200 mm tube lens.

A second design consideration was avoiding lenses that contain significant amount of metal dopant ions, namely short focal length lenses and doublets, which undergo luminescence at near infrared wavelengths [9]. To achieve high indices of refraction, rare-earth elements are often added to the optical glass; while this enables lenses to be made thinner and thus reduce spherical aberration, the dopant ions undergo upconversion and luminesce in wavelength regions that interfere with the detection of intended fluorescent signal [9]. The upconversion process involves real energy states, not virtual states as in two-photon excitation. Thus, the likelihood of the unwanted luminescence increases with the amount of spatial interaction of the laser pulse and glass, as opposed to locations of high peak pulse energy due to focusing of the beam. Therefore, luminescence was more likely occurring in the tube lens rather than the scan lens since the beam is about 20 mm when it reaches the tube lens compared to 4 mm when it reaches the scan lens. I chose to implement a Plössl eyepiece design for the scan lens which uses identical achromatic doublets placed symmetrically around a minute air gap. For multiphoton microscopes, a Plössl design outperforms a single achromatic doublet in terms of reducing aberrations [68]. To investigate whether to use an achromatic doublet or plano-convex lens for the tube lens, I modeled each design in the ray-tracing program Zemax. Design A used a f=40 mm Plössl scan lens

and a f=200 mm achromatic doublet tube lens, while Design B used a f=40 mm Plössl scan lens and a f=200 mm plano-convex tube lens. Although one would expect better performance with an achromatic doublet for the tube lens (Design A), the plano-convex lens (Design B) uses significantly less dopants and thus would alleviate concerns about unwanted luminescence generated in the lens.

I modeled the scan angle for three different configurations: on-axis, 3° off-axis in the x-direction, and 3° off-axis in the y-direction. I used a paraxial approximation of the Olympus XLUMPLFLN20XW 20X microscope objective in the Zemax model to determine the wavefront aberration at the focus of the objective using a custom merit function. While I wanted to optimize the multiphoton microscope for the OPA excitation wavelengths between 1,100 and 1,400 nm, the microscope is also used for imaging at 800 nm with a Ti:S oscillator and near 1,050 nm with a fiber laser. For this reason, I chose to use Thorlabs' B-coating for the optics, which has greater than 99.5% transmission from 700 to 1080 nm and greater than 95% transmission out to 1,400 nm. While the Thorlabs C-coating would be more ideal for the OPA wavelengths as it has a transmission above 99.5% from 1,100 to 1,400 nm, the C-coating performs poorly at 800 nm (85% transmission). Table 2.1 shows the RMS wavefront aberration at the focus of the objective for Design A and B for 800, 1,000, and 1,300 nm over the three aforementioned scan angles. Note that a wavefront error RMS of 0.072 waves or less is considered diffraction-limited [68].

Table 2.1: RMS wavefront aberration (in units of waves) at the objective focus for Design A and B, displayed as Design A / Design B.

| | **Design A / Design B** | | |
|---|---|---|---|
| $\lambda$ (nm) | On-Axis | 3° in X | 3° in Y |
| 800 | .087/.198 | .076/.191 | .162/.295 |
| 1,000 | .031/.031 | .031/.129 | .085/.073 |
| 1,300 | .068/.200 | .012/.299 | .089/.281 |

The results of Table 2.1 indicate the difficulty in optimizing scanning optics over a large wavelength range from 800 nm to 1,300 nm for large scan angles as neither design achieves diffraction-limited resolution for all wavelengths over all scan angles. The best wavelength for both designs is 1,000 nm, which is likely a product of it being in the middle of the three selected wavelengths and the choice of Thorlabs B optical coatings, which are optimized for wavelengths from 700 to 1,100 nm. Design A clearly out performs Design B as only a few configurations in Design A are far from diffraction-limited, whereas just 2 of 9 configurations are diffraction-limited for Design B. However, Design B does not lag too far behind Design A. I chose Design B to ensure luminescence would not disrupt the collection of intended fluorescent signal. With this design, I experimentally measured the maximum field of view to be 731 $\mu$m $\times$ 731 $\mu$m when scaning the XY galvanometer mirror pair at $\pm 12°$.

Another necessary improvement was the collection efficiency of the fluorescent light. The previous microscope used a 740dccxr dichroic (Chroma) to reflect the fluorescent light toward the detector while letting the excitation light pass through. The 740dccxr dichroic has a transmission of greater

than 98% from 750 to 850 nm, making it ideal for Ti:S oscillator wavelengths. However, the 740dcxxr has less than 1% transmission above 1275 nm. The 740dcxxr dichroic was thus replaced with a 775 nm edge multiphoton dichroic (Semrock) that has greater than 96% transmission from 780 nm to 1600 nm, thus allowing both the OPA excitation wavelengths to pass through as well as the Ti:S oscillator (800 nm) and fiber laser (1,050 nm).

For some deep imaging experiments, fluorescent dyes that emit fluorescence longer than 780 nm are desirable. For example, Indocyanine Green (ICG) emits near 830 nm. Dyes with red-shifted emission spectrum such as ICG have the benefit that the fluorescence is less scattered by heterogenous brain tissue. For these experiments, a dichroic that would pass the OPA wavelengths but reflect fluorescence below about 850 nm is needed. I opted for a 875 nm edge multiphoton dichroic (Semrock) that has greater than 96% transmission from 900 nm to 1500 nm. Additionally, a detector that was sensitive to fluorescence near 800 nm was needed. The previous microscope used photomultiplier tube (PMT) detectors with peak sensitivity at $\lambda$=580 nm (H10770PB-40, Hamamatsu Photonics) in both detection channels. While the -40 PMTs are adequate for detecting fluorescence in the visible range, which is typical for fluorophores excited by Ti:S oscillators, they are weakly sensitive to fluorescence near 800 nm. Thus, the option of using a PMT with peak sensitivity at $\lambda$=800 nm (H10770PB-50, Hamamatsu Photonics) was installed.

Figure 2.3 shows the microscope design. The laser is scanned with an XY-galvanometer mirror pair (Cambridge Technologies, 6125H), and then ex-

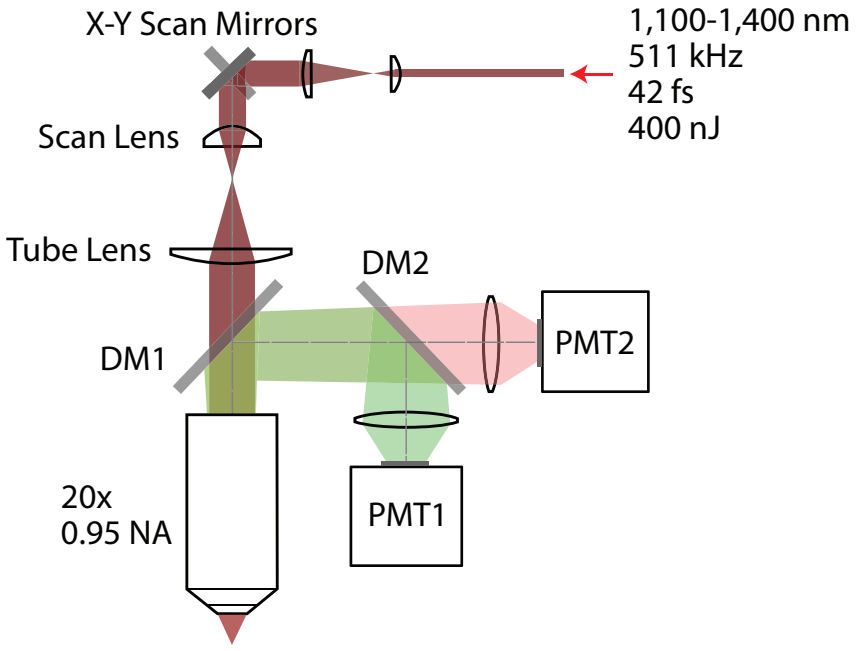


Figure 2.3: Custom-built upright multiphoton microscope. The laser beam is controlled laterally by XY scan mirrors. Dichroic mirror 1 (DM1) transmits the laser light to a high numerical aperture objective with low magnification. Fluorescence is epi-collected back through the objective and directed to the detector arm by DM1. Dichroic mirror 2 (DM2) splits the fluorescence into two channels: red and green. The green channel fluorescence is measured by photomultiplier tube 1 (PMT1) and the red channel fluorescence is measured by photomultiplier tube 2 (PMT 2).

panded via a Plössl scan lens (40 mm) and tube lens (200 mm) to fill the back aperture of the microscope objective (XLUMPLFLN20XW 20X, Olympus). Fluorescence is epi-collected and directed to the PMT detectors by dichroic mirror DM1 and split into two channels by dichroic mirror DM2. The collected PMT signal is synchronized with the regenerative amplifier. Custom LabVIEW software, which is described in Section 2.7, controls the image ac-

quisition.

### 2.3.2 Design 2

In effort to perform wide field of view (FOV) deep-tissue imaging, I redesigned the scanning optics with the purpose to both increase FOV without vignetting on the edges and decrease the optical aberrations on the edges of the images. For Design 2, I approached the design with the notion that the limiting factor should be the microscope objective acceptance angle at the back aperture, $\theta_o$, or equivalently the optical invariance of the objective's back aperture; this approach was motivated by Bumstead et al.'s exquisite journal article detailing the design of large field of view microscopes for MPM [69]. The optical invariant, $I$, is related to the acceptance angle of collimated light, $\theta_o$, via the relationship

$$I = r_o \sin(\theta_o) \tag{2.1}$$

where $r_o$ is the beam radius of the collimated light [69]. To determine $\theta_o$ at the back aperture of the microscope objective, we must relate it to values that are provided by the manufacturers of microscope objectives. Typical values provided are the microscope NA, magnification $M$, and field number FN. The diameter of the FOV for a microscope objective can be calculated using the field number and magnification via the relationship

$$\text{FOV} = \frac{\text{FN}}{M} \ . \tag{2.2}$$

And the acceptance angle of collimated light at the back aperture of the objective can be calculated using the field number via the relationship

$$\theta_o = \sin^{-1}(\frac{\text{FN}}{2f_t}) \tag{2.3}$$

where $f_t$ is the focal length of the tube lens.

I designed the scanning optics assuming that the Olympus XLUMPLFLN20XW 20X microscope objective would be used as this has proven to be the most reliable objective for deep-tissue *in vivo* imaging. The Olympus XLUMPLFLN20XW 20X has a magnification of $M$=20X, field number FN=22 mm, 18 mm back aperture diameter, 2 mm working distance, and a numerical aperture of $NA$=1.0. The high numerical aperture is crucial for deep-tissue imaging and the 2 mm working distance enables a possible imaging depth of about 1.7 mm before concerns arise for the objective to hit the cranial window. There is an inherent trade off between high $NA$ for deep-tissue imaging and wide FOV imaging. The goal of the optical design is to maximize the FOV while imaging at least 1 mm deep within mouse brain tissue, thus the high $NA$ objective is prioritized over a larger FOV. Therefore, the scanning optics are dictated by the choice of using the Olympus XLUMPLFLN20XW 20X microscope objective.

The maximum acceptance angle at the back aperture for the objective is

$$\begin{aligned} \theta_o &= \sin^{-1}(\frac{\text{FN}}{2f_t}) \\ &= \sin^{-1}(\frac{22 \text{ mm}}{2(180 \text{ mm})}) \\ &= 3.5^\circ \ , \end{aligned} \tag{2.4}$$

corresponding to a maximum field of view of

$$\begin{aligned} \text{FOV} &= \frac{\text{FN}}{M} \\ &= \frac{22 \text{ mm}}{20} \\ &= 1.1 \text{ mm} . \end{aligned} \tag{2.5}$$

I note here that microscope manufacturers quote a field number that corresponds to minimal optical aberrations and vignetting; larger field of views are possible albeit with increased aberrations and possible vignetting.

The optical invariant of the back aperture of the objective is

$$\begin{aligned} I_{obj} &= r_o \sin(\theta_o) \\ &= (9 \text{ mm}) \sin(3.5^\circ) \\ &= 0.550 . \end{aligned} \tag{2.6}$$

Following the analysis of Bumstead et al [69], I next evaluated the scan angle of the galvanometer mirrors. There are two galvanometer mirrors corresponding to X and Y translation of the beam. The X-galvo is a 6M2105X60 mirror (Cambridge Technology) and Y-galvo is a 6M2105R60 (Cambridge Technology) with dimensions shown in Fig 2.4. Both mirrors are driven by respective single axis analog servo drivers (671 Series, Cambridge Technology). The absolute maximum scan angle for the galvanometer mirrors is $\pm 15^\circ$. To avoid routinely causing the galvanometer mirrors to scan at their maximum scan angle which may cause them to fail, the maximum scan angle typically used during imaging is $\pm 12^\circ$ corresponding to a $\pm 4$ Volt scan angle on the LabVIEW software. The mirrors overscan the desired field of view by 10% along

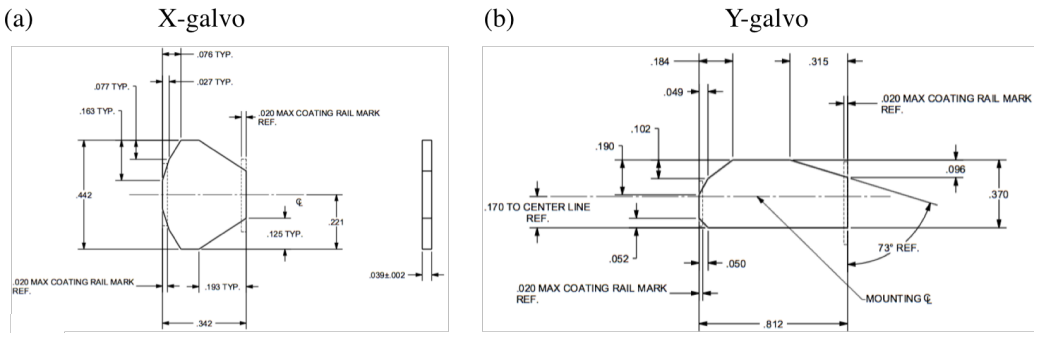


Figure 2.4: Galvanometer mirror dimensions for the (a) X-galvo and (b) Y-galvo.

the "fast axis" in order to ensure the image is collected over the linear portion of the galvanometer mirror waveforms; thus, the fast axis galvanometer mirror scans at $\pm 13.2°$ for an image collection over $\pm 12°$.

An important design consideration is that the incident beam footprint is not larger than either galvanometer mirror at the maximum scan angle. The beam is first incident upon the X-galvo (the "fast axis") at an angle of 45° relative to the optical axis. The beam is then directed to the Y-galvo (the "slow axis") which is at 45° to the X-galvo, equating to a sum total of a 90° turn of the beam, illustrated in Fig. 2.5. Based on Fig. 2.4(a), the X-galvo has a clear aperture, $W$, of 8.7 mm. The maximum scan angle of the X-galvo, $\theta_{g(\text{X-galvo})}$, relative to the optical axis for a $d$=4 mm diameter incident beam is

$$\begin{aligned} \theta_{g(\text{X-galvo})} &= 2[\cos^{-1}(\frac{d}{W}) - 45°] \\ &= 2[\cos^{-1}(\frac{4 \text{ mm}}{8.7 \text{ mm}}) - 45°] \\ &= 35.3° \end{aligned} \tag{2.7}$$

before the incident beam size would have a footprint larger than the aperture

of the X-galvo.

The same evaluation applies for the Y-galvo. Based on Fig. 2.4(b), the Y-galvo has a clear aperture, $W$, of 9.4 mm. The maximum scan angle for the Y-galvo, $\theta_{g(\text{Y-galvo})}$, relative to the optical axis for a $d$=4 mm diameter incident beam is

$$\begin{aligned} \theta_{g(\text{Y-galvo})} &= 2[\cos^{-1}(\frac{d}{W}) - 45^\circ] \\ &= 2[\cos^{-1}(\frac{4 \text{ mm}}{9.4 \text{ mm}}) - 45^\circ] \\ &= 39.6^\circ \end{aligned} \tag{2.8}$$

before the incident beam size would have a footprint larger than the aperture of the Y-galvo. In summary, a 4 mm beam will pose no footprint issues with the XY-galvo pair.

I note here that for a 4.5 mm beam diameter, $\theta_{g(\text{X-galvo})}$=27.7° and $\theta_{g(\text{Y-galvo})}$=32.8°. And for a 5 mm beam diameter, $\theta_{g(\text{X-galvo})}$=19.8° and $\theta_{g(\text{Y-galvo})}$=25.7°. Thus even for a 5 mm diameter beam, footprint issues do not arise until scanning at ±19.8°.

The next consideration is to compare the optical invariance at the back aperture of the objective, which I determined to be $I_{obj}$=0.550, to the optical invariance at the galvanometer mirror pair. Assuming a beam radius of 2 mm and maximum scan angle of ±12°, the optical invariance at the galvanometer mirror pair, $I_{gm}$, is

$$\begin{aligned} I_{gm} &= r_o \sin(\theta_o) \\ &= (2 \text{ mm}) \sin(12^\circ) \\ &= 0.4158 \text{ ,} \end{aligned} \tag{2.9}$$

which is less than $I_{obj}$. To remedy this, the beam can be expanded to 5 mm at the XY-galvo pair without any footprint issues to result in an optical invariance of

$$\begin{aligned} I_{gm} &= r_o \sin(\theta_o) \\ &= (2.5 \text{ mm}) \sin(12^\circ) \\ &= 0.520 \ . \end{aligned} \tag{2.10}$$

$I_{gm}$=0.520 is still slightly below the optical invariance at the back aperture of the objective found to be $I_{obj}$=0.550. Another possibility is to slightly increase the maximum scan angle from the cautious $\pm 12^\circ$. To account for the overscan along the fast axis, the maximum scan angle for which the image could be acquired is $\pm 13.6^\circ$, resulting in an optical invariance of

$$\begin{aligned} I_{gm} &= r_o \sin(\theta_o) \\ &= (2.5 \text{ mm}) \sin(13.6^\circ) \\ &= 0.588 \ , \end{aligned} \tag{2.11}$$

which is indeed greater than $I_{obj}$=0.550. A scan angle of $\pm 13.6^\circ$ would not pose any footprint issues and would fulfill the requirement that the galvanometer mirrors not limit the microscope objective acceptance angle. However, we only need $I_{gm}$ to equal $I_{obj}$, not exceed it; this would enable the galvanometer mirrors to scan at slightly less than their absolute maximum which is favorable for longevity of the mirrors. I find that a scan angle of $\pm 12.7^\circ$ is sufficient to match $I_{obj}$=0.550 for a 5 mm beam.

Next, I evaluated various configurations of scan and tube lenses to ensure they would not further limit the acceptance angle of the objective. In

Design 1 of the scanning optics, I was worried about a mysterious luminescence signal reported in Dr. Estrada's dissertation [9]. Dr. Estrada hypothesized that the signal was due to the laser "excitation source exciting metal dopant ions in the optical glass material and that these ions subsequently return to their ground states via radiative decay." Thus, I opted to use a plano-convex lens for the tube lens in Design 1 instead of an achromatic doublet since plano-convex lens use significantly less dopants. However, I had not witnessed any signs of the mysterious luminescent signal during imaging after upgrading the scanning optics to Design 1, likely because I used an OPA at an output wavelength near 1,300 nm instead of a Ti:S laser with an output at 800 nm. Since an achromatic doublet has significantly less aberrations than a plano-convex lens, I explored designs using achromatic doublets. I found the best tube lens design to be two achromatic doublets each with f=400 mm (Thorlabs AC508-400-C) in a Plössl design configuration for an effective focal length of f=200 mm. I chose 2 inch outer diameter optics instead of 1 inch for the tube lens to ensure the beam would not clip. I opted for the Thorlabs C-coating from 1050-1700 nm to optimize the transmission for the OPA system, ytterbium fiber laser, and diamond laser.

For the scan lens, I explored various lenses and configurations. The constraints were that:

1) the effective focal length needed to be between 40 and 50 mm to ensure the beam expanded to overfill or nearly overfill the microscope back aperture,

2) the maximum scanning angle of the scan lens match or exceed the accep-

tance angle of the objective back aperture,
3) the pupil diameter match or exceed the maximum beam diameter at the galvanometer mirrors which is 5 mm, and
4) the antireflective coating (AR) needs to be optimized for wavelengths between 1,000 and 1,400 nm.

Unfortunately, no scan lens satisfies all of these constraints. It is difficult to create a scan lens with a short focal length and large acceptance angle; further, few lenses have AR coatings optimized for the OPA wavelengths. I opted to use the Thorlabs SL50-2P2 scan lens as it satisfies requirements #1, 3, and 4, and nearly satisfies #2. The SL50-2P2 scan lens has an effective focal length of 50 mm, pupil diameter of 5 mm, $\pm 11.5^\circ$ maximum scanning angle, and wavelength range from 680 to 1600 nm such that it can be used with Ti:S laser systems, ytterbium and erbium fiber laser systems, optical parametric amplifier systems, and diamond lasers.

I used Zemax to model the optical layout of Design 2: Thorlabs SL50-2P2 scan lens and two Thorlabs AC508-400-C in a Plössl design configuration for the tube lens. The modeled 3D layout is shown in Fig. 2.5. It assumes that the laser beam is collimated and has a 5 mm beam diameter incident on the X-galvo mirror (which has a clear aperture of $W$=8.7 mm), then is directed at the Y-galvo mirror (which has a clear aperture of $W$=9.4 mm) at 45° relative to the optical axis and separated by the X-galvo mirror by 9 mm, and then directed to the scan lens at 45°. The Zemax lens "blackbox" file for the scan lens is from Thorlabs since the SL50-2P2 is proprietary. The tube lens file

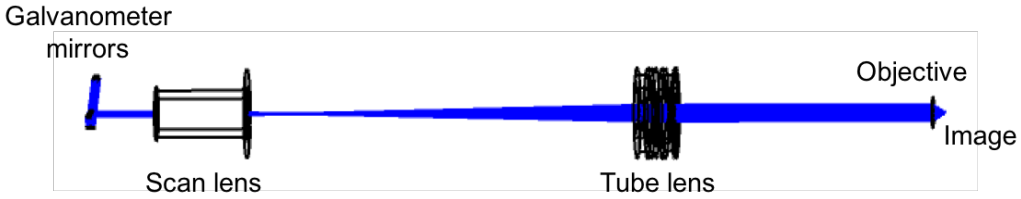


Figure 2.5: 3D layout for the Design 2 scanning optics. The scan lens is a Thorlabs SL50-2P2 with an effective focal length of 50 mm and the tube lens is two Thorlabs AC508-400-C in a Plössl design configuration with an effective focal length of 200 mm.

is provided by Thorlabs in its entirety; a gap of 1 mm is assumed between the two achromatic doublets for the Plössl configuration. The objective is approximated with a paraxial approximation. The Zemax lens data is shown in Fig. 2.6.

| | Surf:Type | | Comment | Radius | Thickness | Material | Coating | Semi-Diameter | |
|---|---|---|---|---|---|---|---|---|---|
| 0 | OBJECT | Standard | | Infinity | Infinity | | | 0.000 | |
| 1 | | Standard | Incoming beam | Infinity | 50.000 | | | 2.500 | U |
| 2 | | Coordinate Break | 45 deg about Y | | 0.000 | - | | 0.000 | |
| 3 | (aper) | Standard | Galvo Mirror 1 | Infinity | 0.000 | MIRROR | | 4.350 | U |
| 4 | | Coordinate Break | 45 deg about Y | | -9.000 | - | | 0.000 | |
| 5 | | Coordinate Break | -45 deg about X | | 0.000 | - | | 0.000 | |
| 6 | (aper) | Standard | Galvo Mirror 2 | Infinity | 0.000 | MIRROR | | 4.700 | U |
| 7 | | Coordinate Break | -45 deg about X | | 0.000 | - | | 0.000 | |
| 8 | | Standard | d_1 | Infinity | 37.779 | | | 15.500 | U |
| 9 | (aper) | Black Box Lens | SL50-2P2.ZBB | | <50.890> | | | 15.500 | U |
| 10 | | Standard | d_2 | Infinity | 221.600 | | | 25.400 | U |
| 11 | (aper) | Standard | 1st Plossl start | -376.250 | 3.000 | N-SF6HT | THORCSLAH64 | 25.400 | U |
| 12 | (aper) | Standard | | 161.500 | 6.500 | N-BAF10 | | 25.400 | U |
| 13 | (aper) | Standard | AC508-400-C | -125.600 | 0.000 | | THORC | 25.400 | U |
| 14 | | Standard | gap of 1mm | Infinity | 1.000 | | | 25.400 | U |
| 15 | (aper) | Standard | AC508-400-C | 125.600 | 6.500 | N-BAF10 | THORC | 25.400 | U |
| 16 | (aper) | Standard | | -161.500 | 3.000 | N-SF6HT | | 25.400 | U |
| 17 | (aper) | Standard | 2nd Plossl end | 376.250 | 0.000 | | THORCSLAH64 | 25.400 | U |
| 18 | (aper) | Standard | d_3 | Infinity | 116.268 | | | 25.000 | U |
| 19 | STOP | Paraxial | objective approx | | 6.996 | | | 9.000 | U |
| 20 | IMAGE | Standard | | Infinity | - | | | 2.392E-04 | |

Figure 2.6: Zemax lens data for Design 2 of the scanning optics.

In Zemax, I optimized the design for wavelengths at 1,000 nm and 1,300 nm, weighting the performance of 1,300 over 1,000 nm by two times. I evaluated the optimal distances between the:

1) second galvanometer mirror and front surface of the scan lens or $d_1$,

2) back surface of the scan lens and front surface of the tube lens or $d_2$, and

3) back surface of the tube lens and back aperture of the objective or $d_3$.

Using a custom merit function, I found the optimal distances to be $d_1$=37.78 mm, $d_2$=221.6 mm, and $d_3$=116.27 mm.

I analyzed the wavefront errors of the design. Fig 2.7 plots the RMS wavefront error for the X- and Y-axis as a function of scan angles. For both

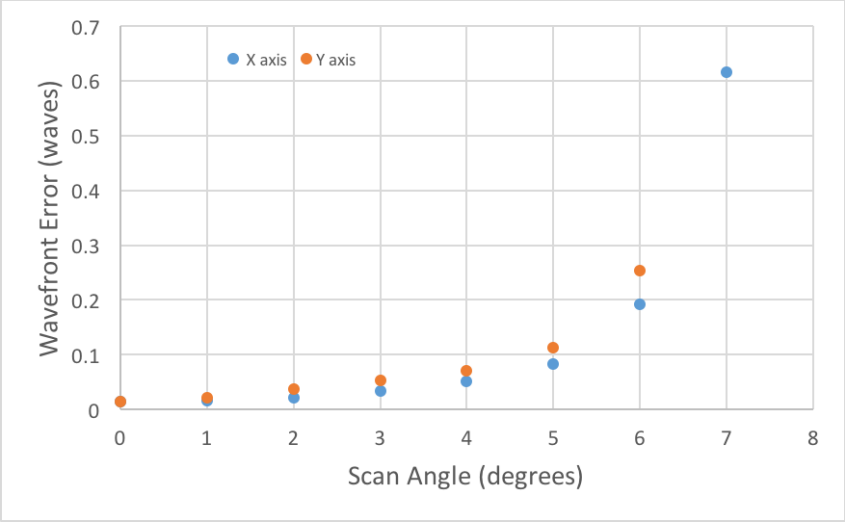


Figure 2.7: Wavefront errors (RMS) for Design 2 as function of scan angles.

the X- and Y-axis, the design is diffraction-limited for scan angles of 4° and below. This is likely an artifact of the paraxial approximation of the objective

breaking down at scan angles near 5° and greater. For scan angles greater than 7°, vignetting starts to occur.

## 2.4 Collection Optics and Photomultiplier Tube Module

Collection optics of the microscope should relay as much light as possible from the back aperture of the microscope objective to the photomultiplier tube (PMT) detectors. The collection optics were originally designed by Dr. Arnold Estrada and are outlined in his dissertation [9]. In Dr. Estrada's thesis, he outlines that to achieve the best combination of high quantum efficiency and low dark current in photomultiplier tubes, manufacturers place a thermoelectric cooling unit on the PMT casing. Unfortunately, the cooling unit reduces the acceptance angle of the PMT photocathode, which is the part of the PMT that converts the light into electron signal via the photoelectric effect (Thanks Einstein!). There is thus a trade off between acceptance angle of the photocathode, which determines the percentage of the collected light that can be detected by the PMT, and the dark current. In Dr. Estrada's first design iteration using a PMT module with a thermoelectric cooler (H7422P-40, Hamamatsu), the cooling unit created a 7.2 mm diameter aperture located 8.9 mm from the photocathode which equates to a numerical aperture of $NA$=0.37. To improve upon this design, Dr. Estrada opted to use a PMT assembly that contained the same photocathode unit but without a thermoelectric cooler (H10770PB-40, Hamamatsu). The PMT assembly has a 10 mm

diameter aperture that is 1.5 mm from the photocathode, resulting in an effective $NA$ of 0.95 - a marked improvement in $NA$. The improved $NA$ comes at the cost of a 60X greater dark current, but due to the low pixel dwell time of approximately 2 $\mu$s when scanning at 511,000 kHz there is still less than one dark count per second per pixel.

Here, I note that while Dr. Estrada's calculation of an effective $NA$ of 0.95 is a valid approach, it is not an approach that makes it easy to compare different collection designs in effort to optimize light collection. I will outline Dr. Estrada's reasoning and assumptions, which he detailed to me in-person (private communication, 19 January 2018), and then detail a more standardized approach to motivate my design of the collection optics. In his thesis, Dr. Estrada shows the following diagram (Fig. 2.8) of the PMT H10770PB-40. Based on Fig. 2.8, Dr. Estrada assumes there is a 1.5 mm spacing between the window and photocathode. And from that calculates an $NA$ of 0.95 based on the following calculation, where $n$ is the index of refraction of the medium (assumed to be 1.0 for air) and $\theta$ is the half-angle of the opening aperture:

$$\begin{aligned} NA &= n \times \sin(\theta) \\ &= 1.0 \times \sin(\tan^{-1}(\frac{5}{1.5})) \\ &= 0.957 \\ &\simeq 0.95 \ . \end{aligned} \tag{2.12}$$

While this is valid, this is the $NA$ of the center of the photocathode to the *back* surface of the window. A more useful $NA$ would be from the photocathode to the *front* surface of the window as the front surface is the limiting aperture,

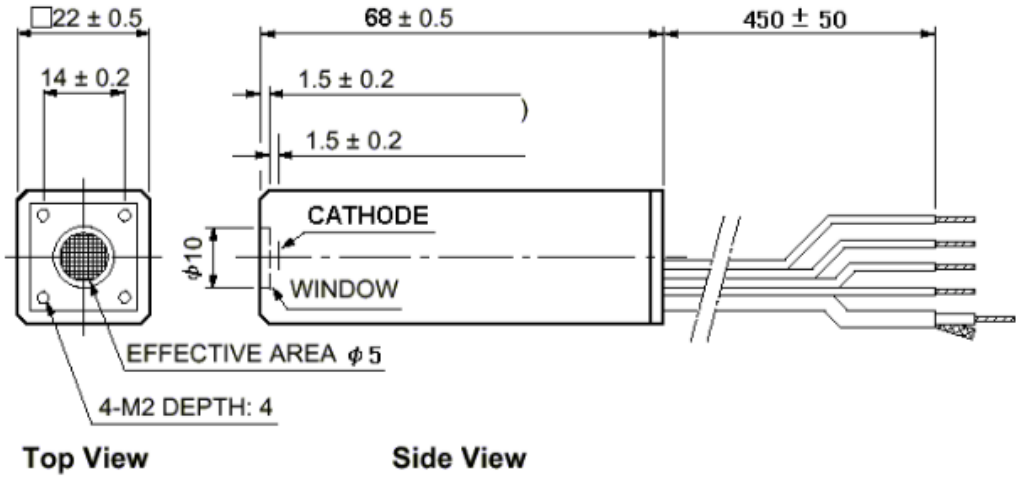


Figure 2.8: Image of PMT H10770PB from Dr. Estrada's doctoral dissertation [9]

.

not the back surface. Looking at Fig. 2.8, the window has a physical size of 1.5 mm and thus the spacing from the photocathode to the front surface of the window is 3 mm. This results in an effective $NA$ of 0.86 for the center of the photocathode. However, since the photocathode has a surface area of 5 mm, numerical aperture is not the ideal characterization because the $NA$ will be spatially dependent - that is, the $NA$ at the center of the photocathode is the greatest, and the $NA$ at the edges of the photocathode is lower because it is being restricted more by the window. The effective $NA$ at the top of the photocathode, where $\theta_1$ is the half-angle from the top of the photocathode to the top of the window and $\theta_2$ is the half-angle from the top of the photocathode

to the bottom of the window, is:

$$\begin{aligned} NA &= n \times \sin(\theta) \\ &= 1.0 \times (\frac{\sin(\theta_1)}{2} + \frac{\sin(\theta_2)}{2}) \\ &= 1.0 \times (\frac{\sin(\tan^{-1}(\frac{2.5}{3}))}{2} + \frac{\sin(\tan^{-1}(\frac{7.5}{3}))}{2}) \\ &= 1.0 \times (\frac{0.640}{2} + \frac{0.928}{2}) \\ &= 1.0 \times (0.320 + 0.464) \\ &\simeq 0.78 \ . \end{aligned} \tag{2.13}$$

We thus find that the effective $NA$ of the top of the photocathode to the front surface of the window is 0.78 whereas the effective $NA$ of the center of the photocathode to the front surface of the window is 0.86. Due to the spatial dependence of the $NA$ across the photocathode, an approach that is spatially independent would be better for standardizing. An alternative approach is to use the acceptance angle of the photocathode based on the limiting aperture. Since the front surface of the window is the limiting aperture, the angle we are interested in is from the front top surface of the window to the top of the photocathode, or equivalently from the front bottom surface of the window to the bottom of the photocathode. This is the same angle we calculated above referred to as $\theta_1$, which I will calculate again here for completeness:

$$\begin{aligned} \theta_1 &= \tan^{-1}(\frac{2.5}{3}) \\ &= 39.81^\circ \ . \end{aligned} \tag{2.14}$$

Due to the symmetry of the distances between the top front surface of the window to the top of the photocathode and the bottom front surface of the

window to the bottom of the photocathode, the acceptance angle of the photocathode is 2 times $\theta_1$. Thus, we can conclude that the acceptance angle of the photocathode for PMT H10770PB-40 is 79.6°.

With this acceptance angle, we can optimize the amount of light relayed from the back aperture of the objective to the PMT. The front surface of collection lens #1 (f=100 mm lens, Thorlabs AC508-100-A) is positioned 100 mm from the back aperture of the objective. Collection lens #2 consists of first a f=50 mm lens (Edmund Optics, NT32-971) and second a f=40 mm aspheric lens (Optosigma, 023-2550) for an effective focal length of 25 mm. The front surface of the first lens in collection lens #2 is positioned 120 mm from the back surface of collection lens #1. PMT H10770PB-40 is positioned 40 mm from the back surface of the second lens in collection lens #2. This results in over 90% of the light from the back aperture of the objective reaching the PMT.

### 2.4.1 Upgrade of PMTs

The unfortunate flood on Christmas of 2017 may have damaged the sensitivity of the pair of H10770PB-40 PMTs. I took this opportunity to explore other options for PMTs. The same constraints applied as discussed above, however I also wanted to avoid an issue I experienced with the H10770PB-40 PMTs. The H10770PB-40 PMT does not come wired to detect the current output, thus I had to wire the current output to a BNC cable. Since the pair of PMTs are positioned close to each other in the microscope, the current output

wires are also close to each other and they contain no casing until they reach the BNC connectors. I thus suspect there was crosstalk between the two PMT current signals, which could be seen in the resulting images. Though the cross talk was weak, it would be apparent at low signal levels such as deep imaging.

To avoid this problem, the H10770PB-40 PMTs were replaced with the Thorlabs PMT2101. A diagram of the photocathode and electronic schematic for PMT2101 is show in Fig. 2.9. The acceptance angle of the photocath-

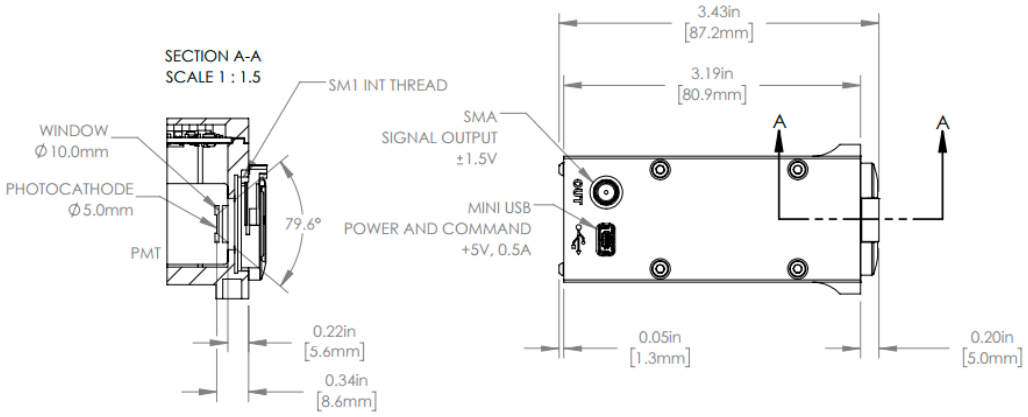


Figure 2.9: Schematic diagram of PMT 2101 from Thorlabs. On the left is the photocathode schematic. On the right is the electronic schematic.

ode for PMT2101 is 79.6°, which matches exactly that of the previous PMT H10770PB-40. This makes sense because PMT2101 contains the Hamamatsu PMT H10770PB-40 module inside of an outer casing that Thorlabs attached. I determined the acceptance angle of the PMT H10770PB-40 above for this reason - to compare it with the Thorlabs PMT2101 module to ensure the microscope collection optics would still be optimized for PMT2101, and indeed they are. The benefit of the PMT2101 module is seen on the right side

of Fig. 2.9 outlining the electronics. The PMT2101 contains a built-in transimpedance amplifier to convert the PMT output current signal to a voltage signal, and there is a SMA connector on the PMT module such that a BNC cable can be directly attached to the casing of the PMT. This eliminates any stray wires carrying the current signal, and thus mitigates crosstalk between the PMT channels.

## 2.5 Z-translation system

In order to reconstruct three-dimensional images, the laser focal spot needs to move axially in the Z-direction. In the initial design of the microscope, Z-translation was performed by moving the microscope objective up and down along the Z-axis. This has the benefit that it does not require the sample to move, however it changes the length between the tube lens and objective ($d_3$) while imaging. To reduce optical aberrations and vignetting, $d_3$ should be set to 142.5 mm and not altered. From an optics perspective, it is better to move the sample along the Z-axis while keeping $d_3$ constant.

To implement a Z-translation system that moves the sample vertically instead of the objective, I placed a Z-translation system under the sample. I opted for a motorized vertical stage from Thorlabs with a travel range of 50 mm and 20 kg max load (MLJ150, Thorlabs); I will refer to this stage as the "LabJack." The LabJack is controlled by the LabVIEW software (discussed below) such that the mouse moves in the Z-axis during image acquisition. The LabJack can perform axial steps down to 100 nm, however I typically

take 5 $\mu$m steps during imaging as a trade off between speed of acquisition and resolution.

## 2.6 Data Acquisition

A high speed data acquisition (DAQ) device (PCI-6259, National Instruments) synchronizes the laser source, scanning mirrors, and detector collection within the MPM system. The PCI-6259 has four 16-bit analog outputs and 32 16-bit analog inputs; the analog inputs can be sampled at 1 MS/s. The PCI-6259 is housed within a computer (CPU #1) and connected to two breakout boards (BNC 2100, National Instruments) through PCI (Peripheral Component Interconnect) slots. The breakout boards have BNC connections to send analog voltage outputs and measure analog voltage inputs. Two of the analog outputs are used to control the pair of galvanometer mirrors. When using the OPA laser, the galvanometer mirrors are synchronized with the OPA laser pulses such that each pixel in the image corresponds to one or a few laser pulses. To perform fast image acquisition with the OPA, each laser pulse will equate to a single pixel in the MPM image - that is, the galvanometer mirrors scan each successive OPA laser pulses a distance of one pixel (the distance of one pixel is determined by the field of view and number of pixels in the image as input by the user through the software control). This is in contrast to MPM imaging with light sources that have repetition rates on the order of tens of millions of pulses per second such as a Ti:S laser. The seed Ti:S laser in the OPA system has a repetition rate of 76 MHz. For imaging at a repetition

rate of 76 MHz, each pixel corresponds to about 200 pulses, and thus there is not a need to precisely control the galvanometer mirrors with each Ti:S laser pulse as the detector measures a sum of the collective fluorescence at each associated pixel in the image. However, in the case of OPA imaging, the detector measures the fluorescence from a single OPA laser pulse and thus must be synchronized with the OPA laser clock which also drives the galvanometer mirrors.

During *in vivo* deep-tissue imaging, the OPA laser source is typically operated at its maximum repetition rate of 511 kHz - equating to each laser pulse spaced by 1.96 $\mu$s. A synchronization clock is used to properly time the OPA laser pulse, galvanometer mirrors, and detector. The synchronization clock originates from the regenerative amplifier's custom synchronization and delay generator (SDG). The SDG enables the regenerative amplifier to operate at a repetition rate up to 511 kHz by controlling the injection of the Ti:S seed pulse with an external clock that it creates internally. This clock defines the repetition rate of the regenerative amplifier and thus the OPA. The SDG outputs a trigger pulse at the repetition rate of the regenerative amplifier, and it is this clock that it used to synchronize the OPA pulse with the galvanometer mirrors - I will refer to this trigger as the "RegA clock." The RegA clock is connected to one of the analog input channels of the PCI-6259 DAQ through a breakout board.

The RegA clock dictates the timing of the galvanometer mirror pair waveforms. The galvanometer mirror waveforms are shown in Fig 2.10. One

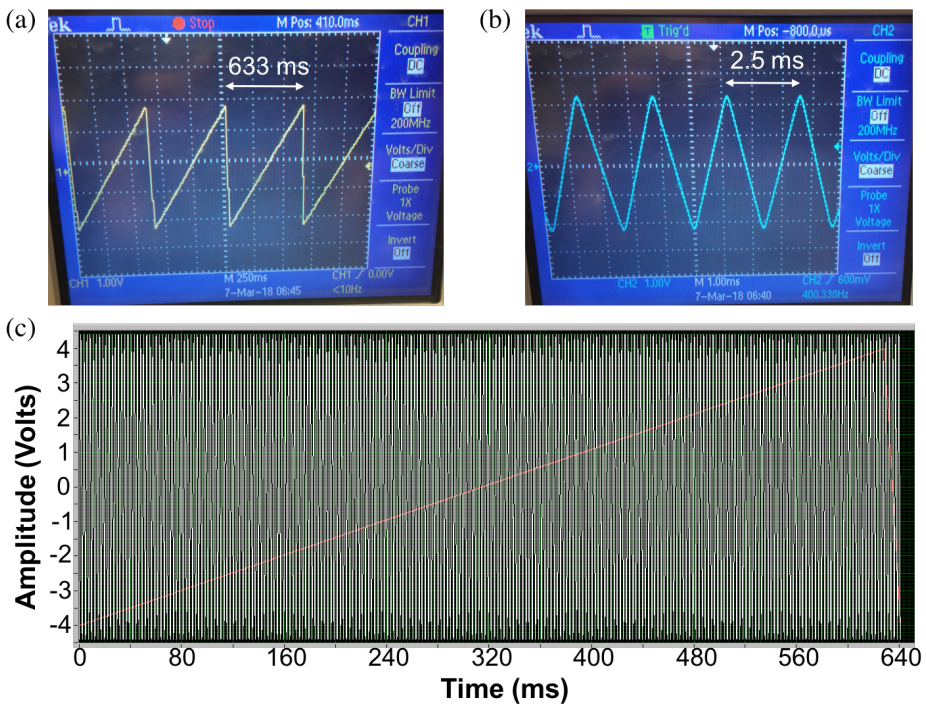


Figure 2.10: Waveforms to drive the galvanometer mirrors for MPM imaging with the OPA operating at a repetition rate of 511 kHz. (a) Triangle waveform for the slow axis. Each triangle represents the scanning of one image and extends 633 ms in time, equating to a frame rate of 1.58 Hz. (b) Sawtooth waveform for the fast axis. Each rise and fall correspond to a new scan line. The scan rate is approximately 400 Hz for the fast axis. (c) The slow (red line) and fast axis (white line) waveforms overlaid for a ±4 Volt scan.

of the mirrors, termed the "slow axis," has a triangle waveform (Fig 2.10(a)) such that the mirror scans the beam linearly down one axis of the image. When it finishes the line, it returns to the top of the line and repeats. Each triangle thus represents a single image. The time length of a single trial is 633 ms when operating at 511 kHz. The other mirror, termed the "fast axis," has a sawtooth waveform (Fig 2.10(b)) such that the mirror raster scans the beam

back and forth across the axis. Each rise and fall of the sawtooth represents a single line in the reconstructed image. When imaging with the OPA at 511 kHz, the line rate is approximately 800 Hz, equating to a scan rate of 400 Hz and frame rate of 1.58 Hz.

The amplitude of the waveforms is dictated by the image field of view requested by the user through the software control. Fig 2.10(c) shows both waveforms overlaid for a single maximum field of view image which is a ±4 Volt scan of the galvanometer mirrors. For a single image, the slow axis (red line) has one linear ramp from -4 to 4 Volts while the fast axis (white line) oscillates quickly in a sawtooth fashion from -4.4 to 4.4 Volts; the fast axis mirror is overscanned by 10%, equating to 0.4 Volts for a ±4 Volt scan, on each side of the sawtooth in order to ensure the image is collected over the linear part of the sawtooth waveform.

A diagram of the data acquisition connections is shown in Fig. 2.11. The PMT detector sources also need to be synchronized with the OPA clock in order to sample the fluorescent signal at its peak. A digital delay generator (DDG) performs this synchronization and time offset. The RegA clock is connected to the input of the DDG, whose output is then connected to the DAQ breakout box. The DDG enables the RegA clock to be adjusted in time with picosecond temporal resolution. The proper timing offset is determined by adjusting the timing to find the maximum signal count which corresponds to the detector sampling immediately after the laser pulse has excited the fluorophores within the focal volume.

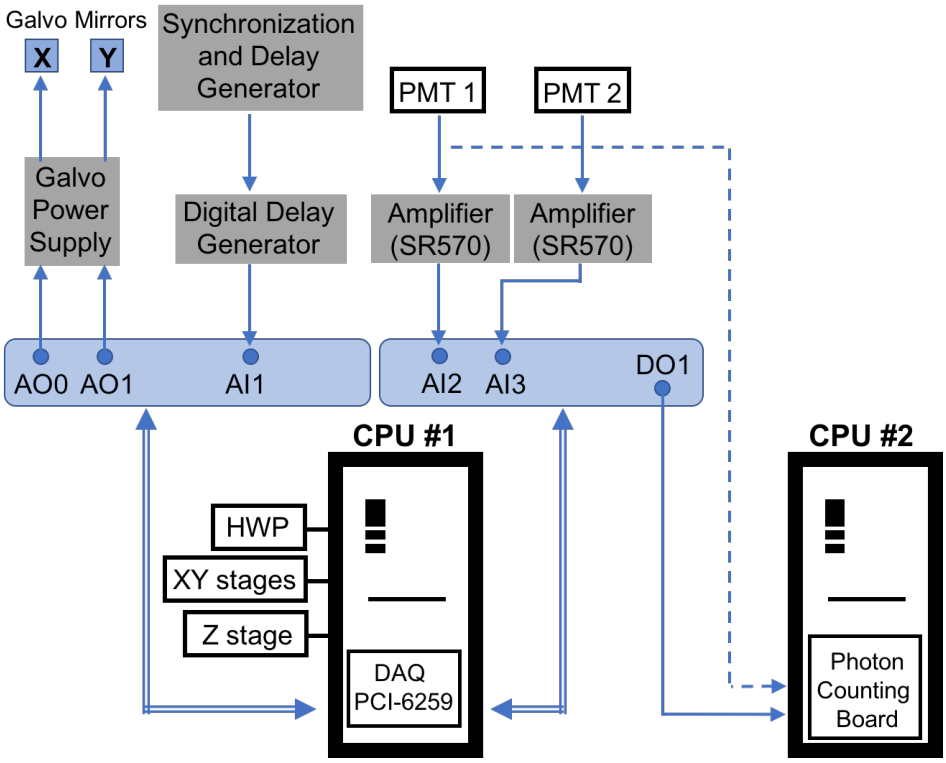


Figure 2.11: Schematic of the hardware connections to acquire data with the MPM system. The PCI-6529 data acquisition (DAQ) card interfaces the hardware connections with computer (CPU) #1. Two breakout boards house the physical analog output (AO), analog input (AI), and digital output (DO) connections. The galvanometer (galvo) mirrors are connected through AO0 and AO1. The clock for the OPA timing comes from the synchronization and delay generator through AI1. PMT 1 and 2 are connected to AI2 and AI3, respectively. The half-wave plate (HWP), and X,Y, and Z linear stages are connected through USB to CPU #1. The photon counting board is located in CPU #2. PMT 1 or 2 can be connected to the photon counting board for lifetime acquisition; DO1 serves as the trigger from the LabVIEW software on CPU #1.

The PMT detector output is a current proportional to the measured fluorescent signal. To convert the current to a voltage to be read by the

DAQ, the PMT current is sent to a transimpedance amplifier (SR570, Stanford Research Systems). It is important to have the proper settings for the transimpedance amplifier to ensure the bandwidth and noise settings are optimized. The output voltage of each transimpedance amplifier, corresponding to the two respective PMT channels, is sent to the DAQ breakout box. The detector channels, termed "PMT 1" and "PMT 2," take up two of the analog input channels. The software reconstructs the 2D images based on the digitized reading of the analog voltage inputs.

A photon counting board (DPC 230, Becker and Hickl) is also integrated into the MPM system. A switch, controlled by the software, can redirect the PMT output from a single channel to the photon counting board which is connected to a second computer (CPU #2).

## 2.7 Software Control

The software control for the MPM system was developed in LabVIEW (**Lab**oratory **V**irtual **I**nstrument **E**ngineering **W**orkbench), a graphical programming environment from National Instruments. The user interface (UI) of LabVIEW is called the *front panel*. The graphical code is on the *block diagram* which is the associated back end for the front panel.

To handle the various desired imaging abilities of the MPM system, the LabVIEW software architecture is configured in a *state machine*. A state machine allows the software to enter different "states" or modes depending on the user requested action. The desired imaging capabilities are:

1) Acquire a 2D image,

2) Acquire a 3D stack,

3) Acquire lifetimes at multiple points in a 2D image, and

4) Acquire a linescan in a 2D image.

To handle the desired imaging capabilities, the LabVIEW software contains the following states:

0) Timeout (idle state),

1) Initialization (initializes necessary variables),

2) Configure Hardware (connects to hardware devices),

3) 2D or 3D Scan (sets up waveforms for image acquisition),

4) 2D Acquisition (executes 2D image acquisition),

5) Lifetime Acquisition (executes lifetime acquisition),

6) Linescan Acquisition (executes linescan acquisition),

7) 3D Acquisition (executes acquisition of 3D image stack), and

8) Main Stop (resets hardware controls and ends program).

When the program starts, it enters “Initialization” to initialize all necessary variables. Next, it enters ”Configure Hardware” to establish connections with the hardware components of the MPM system, which include:

1) Motorized half-wave plate to control the OPA laser power,

2) Shutter to block the OPA laser from entering the microscope,

3) XY galvanometer mirror pair,

4) X and Y linear stages which the sample is positioned on,

5) LabJack Z-translation system, and

6) Linear stage which controls the moving arm of the autocorrelator.

The hardware configuration UI is shown in Fig. 2.12. In the "Imaging Channels" box, the analog output channels for the galvanometer mirror waveforms are selected ("XY Analog Out Physical Channels") which correspond to the BNC connections on the DAQ breakout board. For imaging with lasers besides the OPA, the user can select a sampling rate that is internally generated.

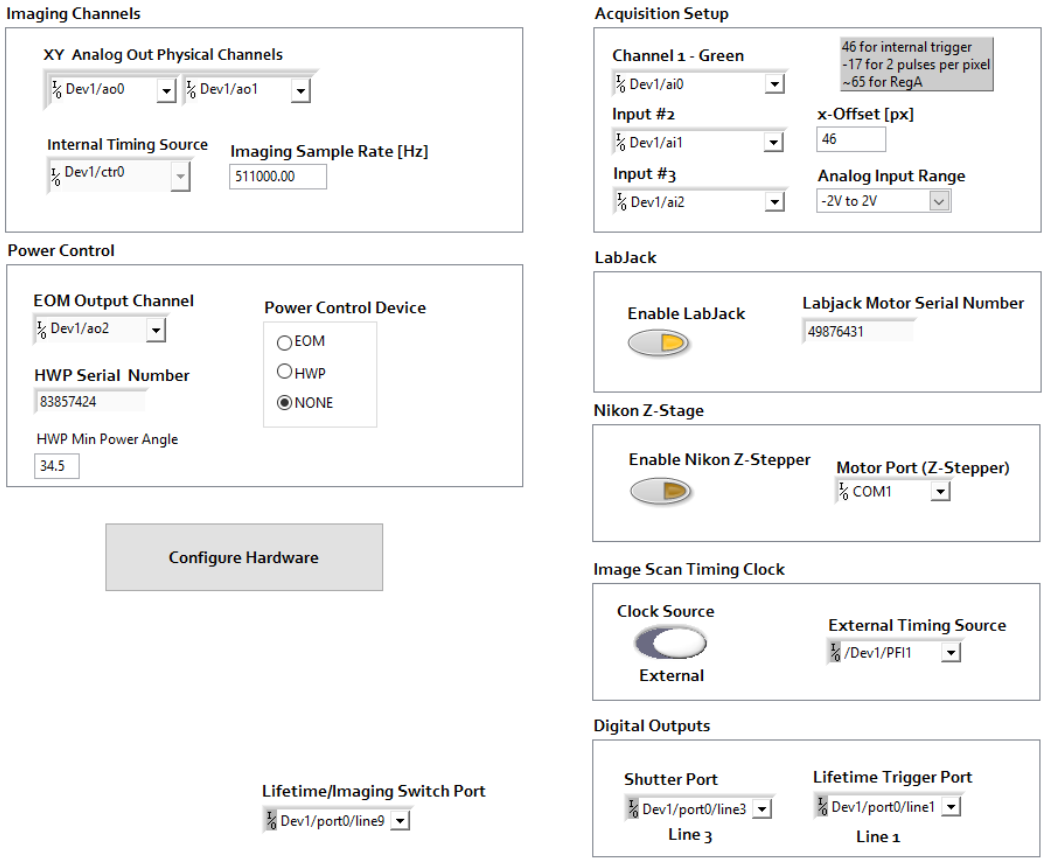


Figure 2.12: Configuration tab on the front panel of the LabVIEW software. The hardware connection channels associated to the DAQ break out board are selected here, as well as imaging parameters associated to the hardware connections.

In the “Power Control” box, the user can select to use the HWP (half-wave plate) to control the OPA output power, or the EOM to control the Ti:S or regenerative amplifier power. In the “Acquisition Setup” box, the user can select the PMT channels. Currently, only the top two channels are used for the two PMTs housed in the microscope, however the software is ready to incorporate a third PMT. The user can select the proper pixel offset for the image which depends on the laser repetition rate and timing scheme. In the “LabJack” box, the user can toggle the connection to the LabJack. Similarly in the ”Nikon Z-Stage” box, the user can toggle the connection to the Nikon Z-stage. The Nikon Z-stage was used previously to move the objective during imaging, however as mentioned above, this method was replaced by moving the sample with the LabJack. Nonetheless, the LabVIEW software has the capability to connect to the Nikon stepper. In the “Image Scan Timing Clock” box, the user can select to use the external RegA clock for timing the image acquisition which is used for OPA imaging, or the user can select internal triggering at any requested sampling rate which is used for imaging with a Ti:S laser or other laser for which each pixel will be associated with tens or hundreds of laser pulses. In the “Digital Outputs” box, the user selects the channel for the shutter to block the laser entry into the microscope. The shutter is automatically closed at the end of each image acquisition to ensure the laser beam is not parked on the brain surface, which can cause significant damage to the brain. Also in the “Digital Outputs” box, the user can select the channel to trigger the acquisition of lifetime data. Any changes to the hardware configuration

UI are made by pressing the "Configure Hardware" button.

After initialization and hardware configuration, the LabVIEW program waits in the "Timeout" idle state for the user to select an action. Typically, the user will next want to acquire a 2D or 3D image. The parameters for either 2D or 3D image acquisition are selected by the user on the "Image" tab of the UI shown in Figure 2.13. The user can press the "2D Scan" for 2D image


Figure 2.13: "Image" tab on the front panel of the LabVIEW software.

acquisition or "3D Scan" for 3D image acquisition. By pressing either button, the program enters the "2D or 3D Scan" state to prepare the waveforms for the

image acquisition. Then, the program enters the "2D Acquisition" state if "2D Scan" was selected or the "3D Acquisition" state if "3D Scan" was selected. In "2D Acquisition" or "3D Acquisition," the image acquisition waveforms are sent to the hardware to perform 2D or 3D imaging, respectively. In both the "2D Scan" and "3D scan" box, the user can select whether to image continuously and save the images, and the number of frames to average at each axial location. The parameters below the "2D Scan" and "3D scan" box are shared for 2D and 3D image acquisition. If the user selects to save the images, the file path is selected in the "Save Path" box. The name of the file is selected in the "Suffix" box; the axial location and time are automatically added to the file name to organize the data and ensure files are not overwritten. In the "2D Scan Setup" box, the user selects the field of view of the image (corresponding to the amplitude of the galvanometer mirror waveforms) and the number of pixels to sample in a single axis for a square image. In the "3D Acquisition Parameters" box, the user selects the start and stop Z-position of the 3D stack, and the axial step size. These distances are relative to the axial locations set in the "LabJack Z-Positioning" box, in which the user can select the relative zero Z-position. In the "Velmex XY Stepper Control" box, the user can move the X and Y stages in both fine and coarse steps. The code for the X and Y stepper buttons lives outside of the state machine architecture such that the user can operate them at any time, even during imaging.

During imaging, pop-up window boxes show the image for PMT #1 and PMT #2. These boxes are toggled with the controls in the "Enable PMT

#1" and "Enable PMT #2" boxes; the false color of the images can also be selected in the boxes - the default is red and green, respectively. The intensity scaling for each image is controlled in the "Intensity Scaling Control" box. The pop-up windows perform real-time averaging if the user selects frame averaging such that each frame is updated in real-time to show the average of the images at each axial location. A metadata file is saved for each image acquisition with the parameters shown in the "Metadata Information" box; this helps the user identify the imaging setup in post-processing.

After "2D Acquisition" or "3D Acquisition," the program enters back into the idle state. If "2D Scan" was previously selected, the most recent image is loaded into both the "Lifetimes" and "Line Scanning" tabs.

The "Lifetimes" tab is show in Fig 2.14. To perform lifetime measurements, the user first selects the button "Select Locations for Lifetime Acquisition..." and then selects the points on the image where to acquire lifetime data. Each point is automatically updated in the "Point Information" table. When the user is finished selecting points, the user clicks the "Finished Picking Points..." button which deactivates the ability for the user to add more points and prepares the waveforms to move the galvanometer mirrors to each location. The user can adjust the amount of time for which lifetime data is acquired at each point in the "Acquisition Time (s)" box. If the user made a mistake selecting points, the user can press the button "Clear Selected Points..." to clear the points from the image and table and then restart the selection process. If the user has selected points and is ready for acquisition

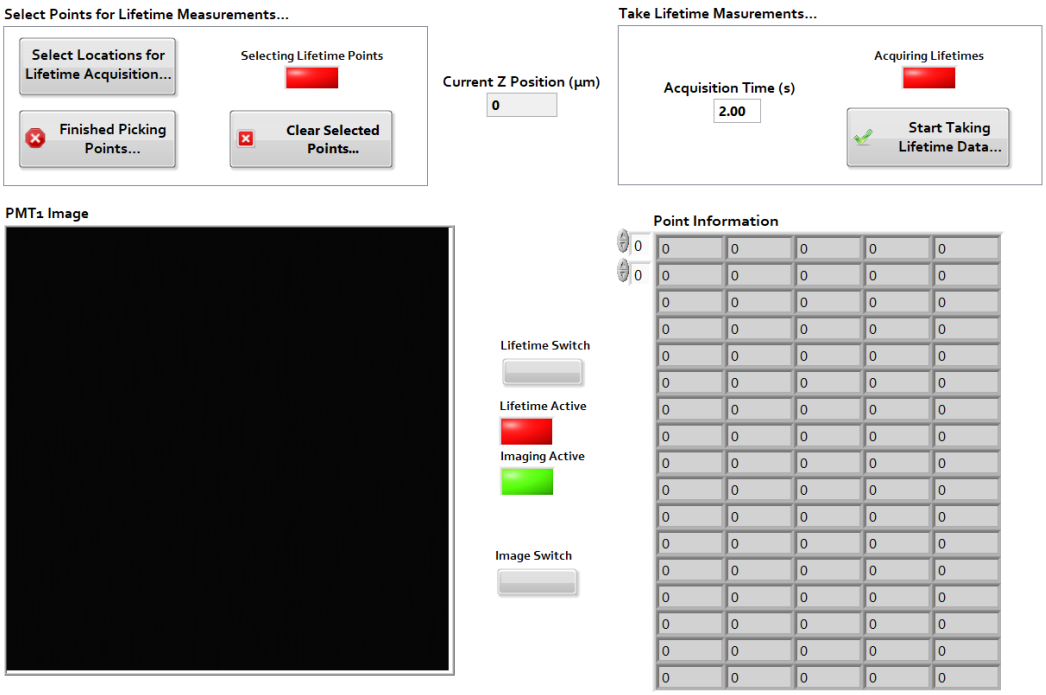


Figure 2.14: "Lifetimes" tab on the front panel of the LabVIEW software.

of lifetime data, the user presses the "Start Taking Lifetime Data..." box; this activates the Becker and Hickl lifetime software to perform lifetime acquisition at each point. The Becker and Hickl software must be configured to start on the falling edge of the trigger pulse.

The "Line Scanning" tab is shown in Fig. 2.15. To perform a line scan, the user selects two points on the left image, which will be the most recent acquired image. The software automatically draws a line between the points and updates the pixel and voltage information of the points on the screen. The user can select the number of lines in the scan ("NumberOfLines"), the image sampling rate ("ImgSamplingRate_Linescan[Hz]"), and the number of

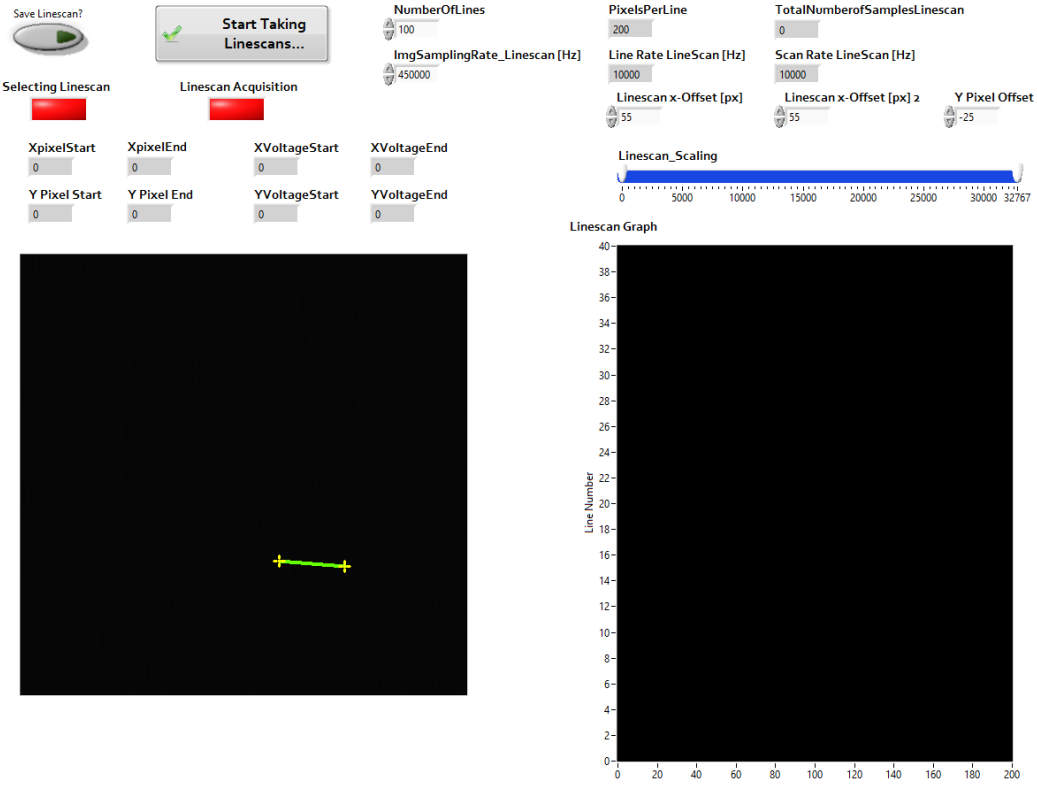


Figure 2.15: "Line Scanning" tab on the front panel of the LabVIEW software.

pixels per each line ("PixelsPerLine"). To save the line scan, the user must select the "Save Linescan?" button before acquiring the line scan. To acquire the line scan, the user selects the "Start Taking Linescan..." button at which point the controls are deactivated until the line scan is completed. After the line scan acquisition, the scan appears in the "Linescan Graph" for the user to visually inspect the image.

# Chapter 3

# Fluorophore Characterization

To maximize imaging depth, it is crucial to know what fluorophores are brightest and at what excitation wavelengths such that the excitation light is tuned to the absorption peak. The two-photon action cross sections for most common fluorophores have been characterized for the Ti:S oscillator wavelength range from 700 to 1,000 nm [7,70–72], including for fluorescent proteins [4]; many of these results are illustrated in Fig. 1.3. This has lead to a rise in popularity of 2PM with Ti:S oscillators because users can quickly identify the ideal fluorophore for their application. Unfortunately, there is little literature characterizing the two- and three-photon cross sections of fluorophores for wavelengths beyond 1,000 nm.

Based on Fig. 1.2, an excitation wavelength near 1,300 nm minimizes the effects of scattering in brain tissue while avoiding deleterious water absorption regions. I sought to characterize numerous fluorophores across the OPA tuning range of 1,100 to 1,400 nm in order to identify promising fluorophores to maximize imaging depth for *in vivo* deep-tissue imaging with an excitation wavelength near 1,300 nm.

## 3.1 Two-photon and Three-photon Excitation of Common Fluorophores

I first identified multiple common fluorophores that undergo two- or three-photon excitation at longer wavelengths. To determine whether the fluorescence from each fluorophore was the result of two-photon excitation (2PE) or three-photon excitation (3PE), I measured the dependence of the fluorescence on excitation power in a cuvette. The slope of the logarithmic plot indicates whether the generated fluorescence is due to 2PE or 3PE. Figure 3.1 shows the power dependence for the fluorescent dyes: Fluorescein, Rhodamine B, Ruthenium, Texas Red, and ICG, and the fluorescent protein: yellow fluorescent protein (YFP). I note that the YFP sample was a thy1-YFP-H mouse brain slice, not a cuvette. The power dependence was determined by exciting Fluorescein, Ruthenium, and Rhodamine B at $\lambda$=1243 nm, Texas Red at $\lambda$=1296 nm, YFP at $\lambda$=1330 nm, and ICG at $\lambda$=1315 nm. A slope near 3.0 for Fluorescein, Rhodamine B, Ruthenium, and YFP indicate they undergo 3PE. A slope near 2.0 for ICG indicates it undergoes 2PE. Near an excitation wavelength of 1,280 nm, Texas Red undergoes 2PE at low excitation powers; however, Texas Red undergoes both 2PE and 3PE at higher excitation powers, indicated by a slope of 2.53.

## 3.2 Brightness Characterization of Common Fluorophores

To demonstrate deep-tissue *in vivo* multiphoton imaging, I opted to use the fluorescent dyes Texas Red and ICG for visualizing vasculature and

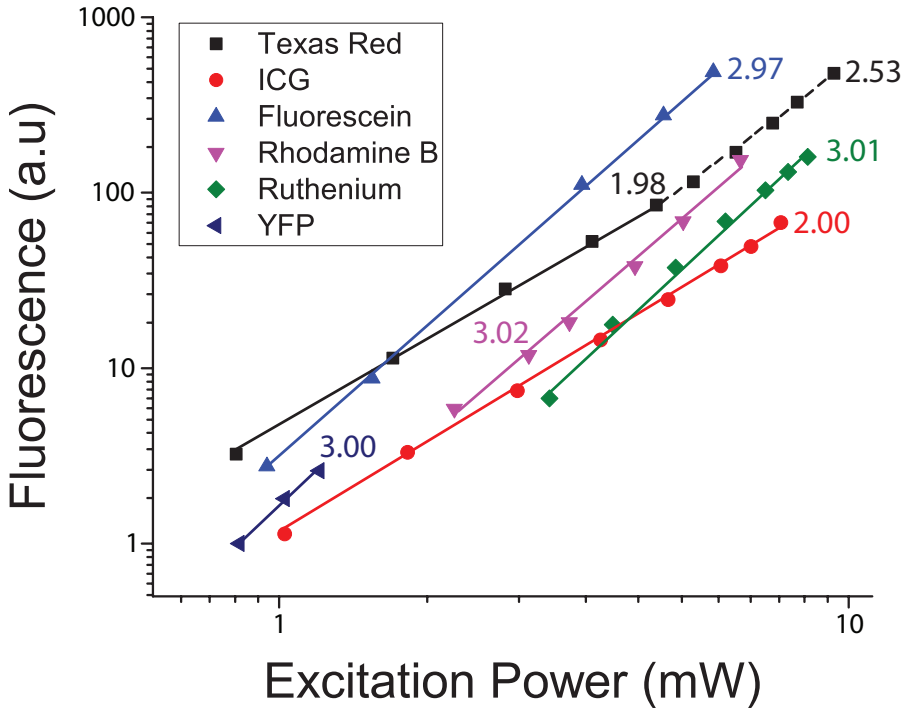


Figure 3.1: Logarithmic power dependence plot for common fluorophores. The slope indicates the n-photon excitation.

the fluorescent proteins YFP and tdTomato for neuron imaging. Two-photon absorption spectra near 1,300 nm were not previously reported for either Texas Red, ICG, or YFP. I characterized the absorption spectra of Texas Red and ICG, but was unable to do so reliably for YFP due to the inability to accurately measure a concentration of the amount of YFP in a sample. I did not characterize tdTomato as previous work by Drobizhev et al. demonstrated that tdTomato has a two-photon cross section of about 30 GM at 1,140 nm and falls off significantly above 1,200 nm [4].

## 3.3 Methods for Characterization of Common Fluorophores

The action cross section, a product of the n-photon absorption cross section, $\sigma_n$, and the fluorescence quantum efficiency, $\eta$, is a standardized measure of the brightness of a fluorophore. Accurately measuring the two-photon and three-photon action cross section of a fluorophore is difficult due to the many parameters that must be measured. The generalized n-photon action cross section is defined as

$$\eta\sigma_n = n\langle F^{(n)}(t)\rangle \frac{(f\tau)^{n-1}}{g_p^{(n)}} \frac{1}{\phi C n_o} \frac{8\pi^{3-n}\lambda^{2n-3}}{a_n (NA)^{2n-4}\langle P(t)\rangle^n} \tag{3.1}$$

where $n$ is the number of photons absorbed, $\langle F^{(n)}(t)\rangle$ is the time-averaged fluorescence photon flux, $f$ is the laser repetition rate, $\tau$ is the laser temporal pulse width, $\lambda$ is the excitation wavelength in vacuum, $g_p^{(n)}$ is the $\mathrm{n}^{\mathrm{th}}$ order temporal coherence of the laser source ($g_p^{(2)}$=0.664 and $g_p^{(3)}$=0.51 for Gaussian temporal pulse profiles), $\phi$ is the system collection efficiency, $C$ is the concentration of the fluorophore, $n_o$ is the refractive index of the sample media, $a_n$ represents the distribution of the excitation intensity within the diffraction-limited focal volume ($a_2$=64 and $a_3$=28.1), $NA$ is the numerical aperture of the objective, and $\langle P(t)\rangle$ is the time-averaged incident power [10, 62, 70]. I note two underlying assumptions for this definition of the action cross section. One, the fluorescence quantum efficiency is assumed to be irrespective of the n-photon excitation - that is, $\eta = \eta_1 = \eta_2 = \eta_3$. And two, the sample thickness is much greater than the Rayleigh length, $z_r$, defined as

$$z_r = \frac{\pi\omega_o^2}{\lambda} \tag{3.2}$$

where $\omega_o$ is the beam waist [62].

Using Equation 3.1, the two-photon action cross section $\eta\sigma_2$ is

$$\eta\sigma_2 = 2\langle F^{(2)}(t)\rangle \frac{(f\tau)^2}{0.664} \frac{1}{\phi C n_o} \frac{8\pi\lambda}{64(NA)\langle P(t)\rangle^2}. \tag{3.3}$$

Following the methods presented in Cheng et al. [10], I measured the two-photon action cross section of Texas Red and the relative cross section of ICG. First, I dissolved Texas Red (Thermo Fisher Scientific) in saline and placed 0.5 mL of a 48 $\mu$M solution into a cuvette. Similarly, I dissolved ICG (Sigma-Aldrich) in a 5% bovine serum albumin-saline solution and placed 0.5 mL of a 100 $\mu$M solution into a cuvette. The concentrations of Texas Red and ICG were determined via spectrophotometry (UV-3600, Shimadzu) using known extinction coefficients. I then measured the fluorescence from each cuvette using the setup shown in Fig. 2.3 replacing the objective with one with a smaller back aperture (CFI Plan 10X/0.25 NA, Nikon) to ensure the objective focus in the cuvette was diffraction-limited and added a photon counter (DPC-230, Becker and Hickl) to measure the number of fluorescent photons detected by the PMT. I then measured the dependence of Texas Red and ICG fluorescence on excitation power to determine whether the fluorescence was the result of two-photon excitation (2PE) or three-photon excitation (3PE) across the tuning range of the OPA. For these measurements, the excitation power was increased from about 0.3 mW to 1 mW. Next, I measured the cross sections of Texas Red and ICG with the same setup. For these measurements, 1 mW of power or less was used to ensure the same power range as the power

dependence measurements. Following the methods outlined in Cheng et al. [10], I measured the absolute action cross section of Texas Red using their reported value of 20.6 GM as the two-photon action cross section of SR101 at 800 nm to calculate the collection efficiency for Texas Red in our system, since SR101 and Texas Red have very similar emission spectra. I measured the relative cross section for ICG but was unable to measure the absolute cross section due to the absence of a dye with a known cross section and similar emission spectra to ICG. However, I note that Berezin et al. measured ICG in water to have a two-photon action cross section of 6.3 GM at 1.55 $\mu$m excitation [57].

Power dependence measurements for Texas Red and ICG are shown in Fig. 3.2(a). Between an excitation wavelength of 1,200 and 1,450 nm, ICG undergoes 2PE; Fig. 3.2(a) demonstrates this for 1,350 nm indicated by a slope of 2.03. Near an excitation wavelength of 1,280 nm, Texas Red undergoes 2PE as indicated by a slope of 1.97. I note that Texas Red can undergo both 2PE and 3PE at higher excitation powers as demonstrated in Fig. 3.1. However, for the imaging experiments with Texas Red shown in Figs. 4.1, 4.3, and 4.7, I expect that the excitation power at the samples focus is in the 2PE regime. Figure 3.2(b) shows the two-photon action cross section of Texas Red from 1,150 to 1,360 nm. Figure 3.2(c) shows the relative two-photon cross section of ICG from 1,200 to 1,450 nm. Measuring the system collection efficiency of the system is difficult, and the nonlinear dependences of the cross section on numerous parameters makes the measurements sensitive to errors. The estimated uncertainty for the cross section measurements is 30%. I chose exci-

tation wavelengths for *in vivo* imaging with Texas Red and ICG, respectively, as a compromise between maximizing the attenuation length in brain tissue, fluorophore brightness, and laser power.

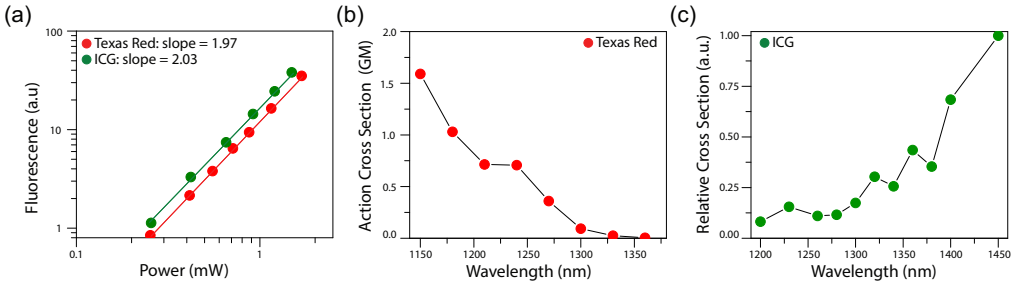


Figure 3.2: **Characterization of Texas Red and ICG.** (a) Logarithmic power dependence plot of Texas Red and ICG. ICG undergoes two-photon excitation at 1,350 nm indicated by a slope of 2.03. Texas Red undergoes two-photon excitation at 1,280 nm as indicated by a slope of 1.97. Note that the power was measured after the objective. (b) Two-photon action cross section of Texas Red in units of Goeppert-Mayer (GM). Solid line serves as a guide to the eye. (c) Relative two-photon cross section of ICG. Solid line serves as a guide to the eye.

Using Equation 3.1, the three-photon action cross section $\eta\sigma_3$ is

$$\eta\sigma_3 = 3\langle F^{(3)}(t)\rangle \frac{(f\tau)^2}{0.51} \frac{1}{\phi C n_o} \frac{8\lambda^3}{28.1(NA)^2\langle P(t)\rangle^3} \ . \tag{3.4}$$

Following the methods presented in Cheng et al. [10], I measured the three-photon action cross section of Fluorescein. First, I dissolved Fluorescein (Acros Organics) in deionized water within a cuvette, and added NaOH until I reached a pH value near 13; the measured value was 12.94. I then used spectrophotometry as described for Texas Red and ICG to determine the concentration of the Fluorescein cuvette was 68 $\mu$M. Next, I confirmed that the Fluorescein sample

underwent three-photon excitation across the OPA spectrum. Using Cheng et al.'s reported value of 32.8 GM for the two-photon action cross section of Fluorescein at 800 nm, I measured the system collection efficiency for the Fluorescein. The three-photon action cross section of Fluorescein is shown in Fig. 3.3. The measurement is in good agreement with one previously published value [10].

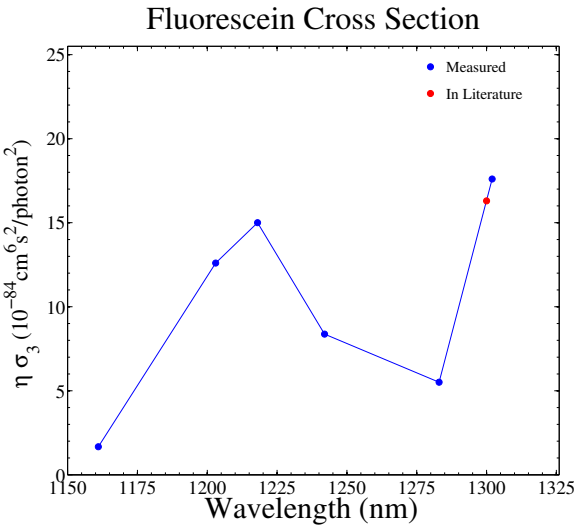


Figure 3.3: The three-photon action cross section for Fluorescein across the OPA excitation wavelengths. The literature value is from Cheng et al. [10].

# Chapter 4

# *In vivo* Multiphoton Microscopy Imaging of the Mouse Cortex

To demonstrate the ability of the OPA laser system to image deep tissue in the mouse cortex, I perform *in vivo* multiphoton microscopy imaging with a diverse array of fluorophores: Texas Red and ICG to label vasculature, and tdTomato and YFP to label neurons. The OPA laser system has the ability to image beyond 1 mm, extending the traditional depth limit in 2PM. Parts of this chapter are adapted with permission from the Optical Society of America from the journal article "*In vivo* multiphoton imaging of a diverse array of fluorophores to investigate deep neurovascular structure," Vol 8, Issue 7, pp. 3470–3481, Copyright (2017) [11] for which David Miller developed the microscope and laser instrumentation, designed and performed the experiments, analyzed the data, and wrote the manuscript.

## 4.1 Animal Preparation

All animal procedures were approved by The University of Texas at Austin Institutional Animal Care and Use Committee. Cranial window implants were prepared in C57 mice and left the dura intact as described in [73].

I note that for imaging Texas Red and YFP simultaneously, thy1-YFP-H mice from Jackson Laboratory expressing YFP in motor and sensory neurons (particularly layer V pyramidal cells) were used. Mice were anesthetized with isoflurane throughout surgery and imaging. Body temperature was maintained at 37.5° Celsius and 0.1 mL subcutaneous injections of 5% (w/v) glucose in physiological saline were applied every 2 hours. For imaging Texas Red and ICG, a retro-orbital injection of the fluorescent dye was performed to label blood plasma in the vasculature. For imaging tdTomato, neurons were labeled by cortical injection of adeno-associated viral (AAV) vectors carrying a tdTomato plasmid. Imaging sessions were performed a week following the delivery of the viral vectors.

## 4.2 Imaging Parameters

Multiphoton microscopy images were acquired with the custom microscope shown in Fig. 2.3. Images were separately acquired in different mice for each fluorophore. Appropriate emission filters were placed in front of each PMT. For imaging Texas Red, a 750 nm short pass (FF01-750/SP-25, Semrock) and 610 nm band pass (HQ/610/75M, Chroma) were used. For imaging ICG, a 594 nm long pass (BLP01-594R-25, Semrock) and 830 nm bandpass (RT-830, Edmund Optics) were used. For imaging tdTomato, a 750 nm short pass and 609 nm band pass (FF01-609/181-25, Semrock) were used. For imaging Texas Red and YFP simultaneously, I used the aforementioned parameters for Texas Red and a 680 nm short pass filter (FF01-680/SP-25, Semrock) and

510 nm band pass filter (FF01-510/84- 25, Semrock) for YFP. For imaging sessions with Texas Red and tdTomato, respectively, I used a dichroic with a cutoff at 775 nm (FF775-Di01-52x58, Semrock) for DM1 and removed DM2. For imaging ICG, I used a dichroic with a cutoff at 875 nm (FF875-Di01-52x58, Semrock) for DM1 and removed DM2. For imaging Texas Red and YFP, I used the 775 nm edge dichroic for DM1 and a custom 570 nm edge dichroic for DM2 to separate the Texas Red and YFP fluorescence. For all imaging sessions besides ICG, the -40 PMTs were used as they have peak sensitivity at $\lambda$=580 nm. For ICG imaging, the -50 PMTs were used which have peak sensitivity at $\lambda$=800 nm. Imaging sessions used either the XLUMPLFLN20XW 20X (referred to as 20X) or XLPLN25XSVMP2 25X (referred to as 25X) microscope objective, both from Olympus.

Heavy water was used as the immersion medium to reduce absorption of the OPA excitation light. All frames are 512 by 512 pixels and all stacks are in 5 $\mu$m depth increments. The laser power was adjusted throughout each stack with a half-wave plate and polarizing beam splitter to ensure sample damage did not occur [74]. I observed no damage to vasculature or neurons and was able to image the mice chronically. Rendering of three-dimensional (3D) stacks was performed with visualization software (Aviso standard, VSG; Fiji [75]; and ParaView [76]). For 3D stacks with yellow dotted lines, the line signifies the reference plane for which all frames below were normalized; all frames above were normalized individually.

## 4.3 Vasculature Imaging

Figure 4.1(a) demonstrates an imaging depth of 1,535 $\mu$m for vasculature labeled with Texas Red. I was able to acquire the entire stack in 5 $\mu$m

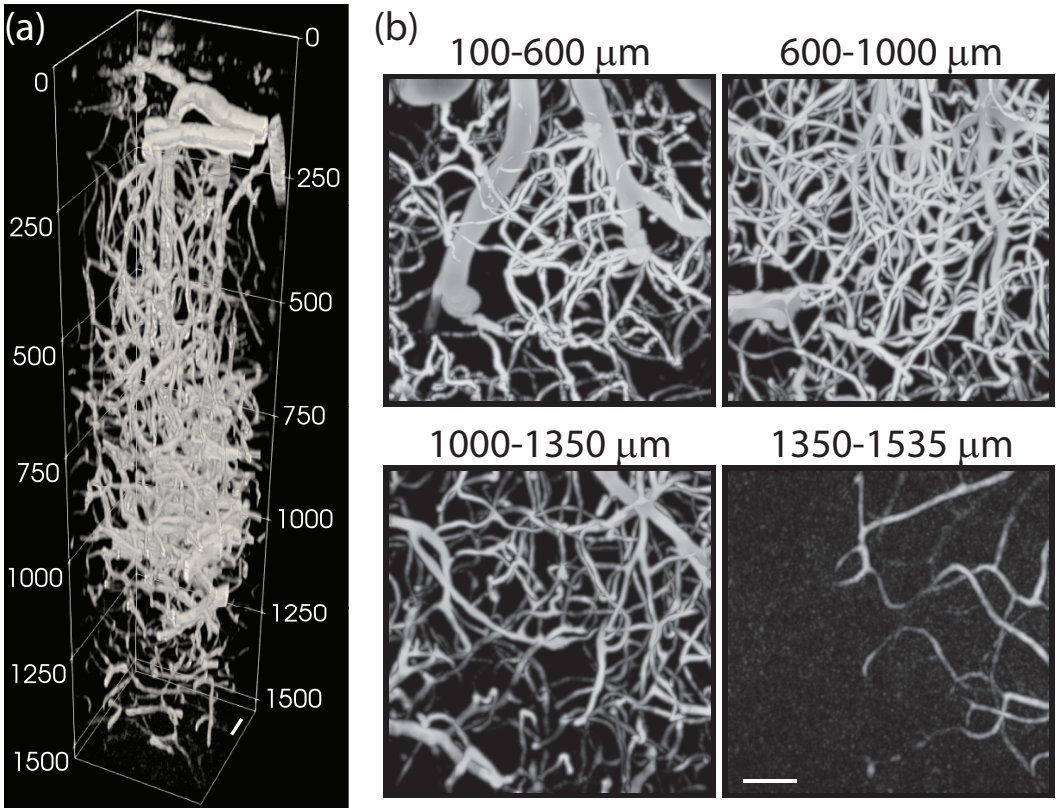


Figure 4.1: *In vivo* two-photon microscopy images of vasculature labeled with Texas Red. (a) Three-dimensional reconstruction of a 1,535 $\mu$m stack. (b) x-y intensity projections of stack shown in (a). All scale bars are 50 $\mu$m unless otherwise indicated.

depth increments because I performed reasonable averaging (3 frames from 0 to 500 $\mu$m, 5 frames from 500 to 700 $\mu$m, 7 frames from 700 to 900 $\mu$m, 9 frames from 900 to 1,100 $\mu$m, 11 frames from 1,100 to 1,300 $\mu$m, 14 frames

from 1,300 to 1,400 $\mu$m, 16 frames from 1,400 to 1,500 $\mu$m, and 24 frames from 1,500 to 1,535 $\mu$m) and imaged at a fast frame rate of 1.58 Hz. I attribute the minimal averaging, even at depths greaten than 1,000 $\mu$m, to the high pulse energy of the OPA. The excitation power was increased to maintain similar signal levels down to 1,000 $\mu$m, at which point full power was reached equating to 122 mW at the sample surface (transmission of the 25X objective at 1,215 nm is 67%). All frames were normalized individually. In Fig. 4.1(b), individual blood vessels can be seen with high contrast beyond 1,000 $\mu$m and still resolved beyond 1,350 $\mu$m.

In order to quantify the benefits of the high repetition rate excitation source, SBR analysis was performed at various imaging depths and laser repetition rates. For these measurements, the SBR was calculated from line profiles taken through vessels. Figure 4.2(a) compares the highest SBR value obtained at depths of 100, 300, 600, and 940 $\mu$m for repetition rates of 511 (red) and 255 kHz (blue). As the imaging depth increases, the benefits of a 511 versus 255 kHz repetition rate become apparent as an improvement by more than a factor of $\sqrt{2}$ arises. Figure 4.2(b) compares the SBR of a vessel at z=940 $\mu$m for imaging with a laser repetition rate of 511 kHz versus 255 kHz (the sampling rate was synchronized with the respective laser repetition rate). The raw images of the vessel for imaging at both 511 kHz and 255 kHz were averaged over 10 frames, and the yellow line indicates a 6 $\mu$m thick line over which the SBR was calculated. The line profile shows that the SBR is 12.0 for imaging at 511 kHz, and 5.5 for imaging at 255 kHz. Figure 4.2(c) shows the normalized

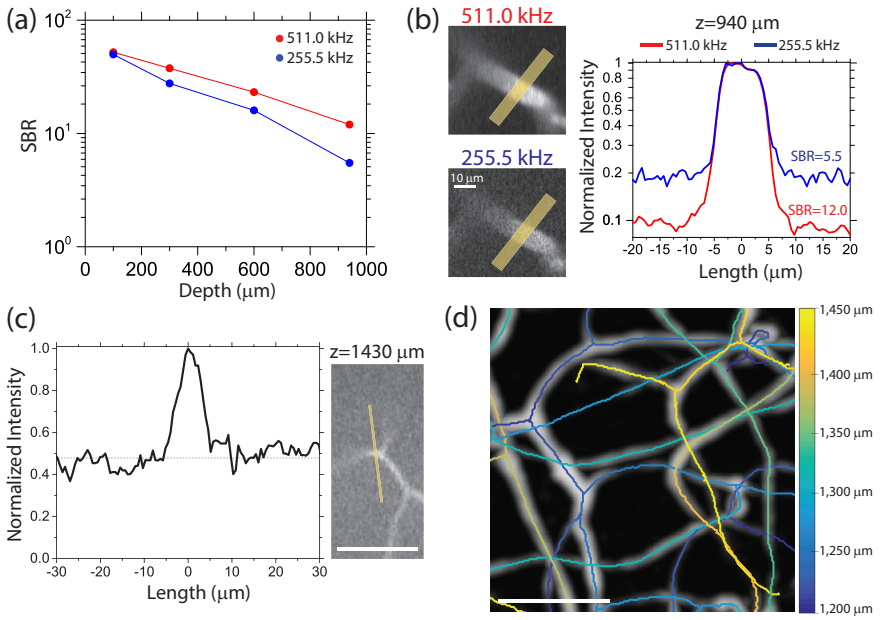


Figure 4.2: (a) The SBR as a function of depth for a laser repetition rate of 511 kHz (red) and 255 kHz (blue). The lines serve as guides for the eye. (b) Comparison of the SBR for a vessel at z=940 $\mu$m for laser repetition rates of 511 and 255 kHz. The vessel images are a 10-frame average at the respective repetition rate; the images are shown at full scale. The line profile is averaged over a 6 $\mu$m line indicated by the yellow lines in the vessel images. (c) Normalized intensity profile for a line through a blood vessel at z=1430 $\mu$m, demonstrating a SBR above 2 (the dotted black line indicates the calculated background). The yellow line on the vessel image, which is a 16-frame average, indicates where the line profile was taken. (d) Centerlines of vessels from 1,200 to 1,450 $\mu$m depth encoded by color . The centerlines are overlaid on a maximum intensity projection of the raw data from Fig. 4.1. All scale bars are 50 $\mu$m unless otherwise indicated.

intensity profile for a line through a blood vessel (indicated by yellow line) at a depth of z=1,430 $\mu$m for the stack shown in Fig. 4.1. The dotted line indicates the background value calculated by averaging pixel values outside of the vessel. A 1 pixel median filter was applied to the image before taking the line profile, however the image histogram was not stretched. The calculated SBR is 2.09. Due to the high SBR of the deep image data and the rapid stack acquisition at fine axial steps, the vascular network could be vectorized using Volumetric Image Data Analysis [77, 78]. Figure 4.2(d) depicts these results as centerlines of vessels from 1,200 to 1,450 $\mu$m for the stack shown in Fig. 4.1 overlaid on the maximum intensity projection of the raw data from 1,200 to 1,450 $\mu$m. The color of the centerlines encodes for depth according to the color map.

Fig. 4.3(a) demonstrates another imaging session of vasculature labeled with Texas Red for which an imaging depth of 1,200 $\mu$m is achieved; thus demonstrating the repeatability of the OPA to image beyond 1 mm in mouse cortex. The excitation power was increased to maintain similar signal levels down to 800 $\mu$m, at which point full power was reached equating to 34 mW at the sample surface (transmission of the 20X objective at 1,280 nm is 32%). In Fig. 4.3(b), individual blood vessels can be seen with high contrast beyond 800 $\mu$m, and still resolved beyond 1,100 $\mu$m. During the acquisition of the 3D stack, I averaged for 5 frames from 0 to 500 $\mu$m, 10 frames from 500 to 700 $\mu$m, and 30 frames from 700 to 1,200 $\mu$m. Fig. 4.3(c) demonstrates the system's ability to perform line scan in individual capillaries at an imaging

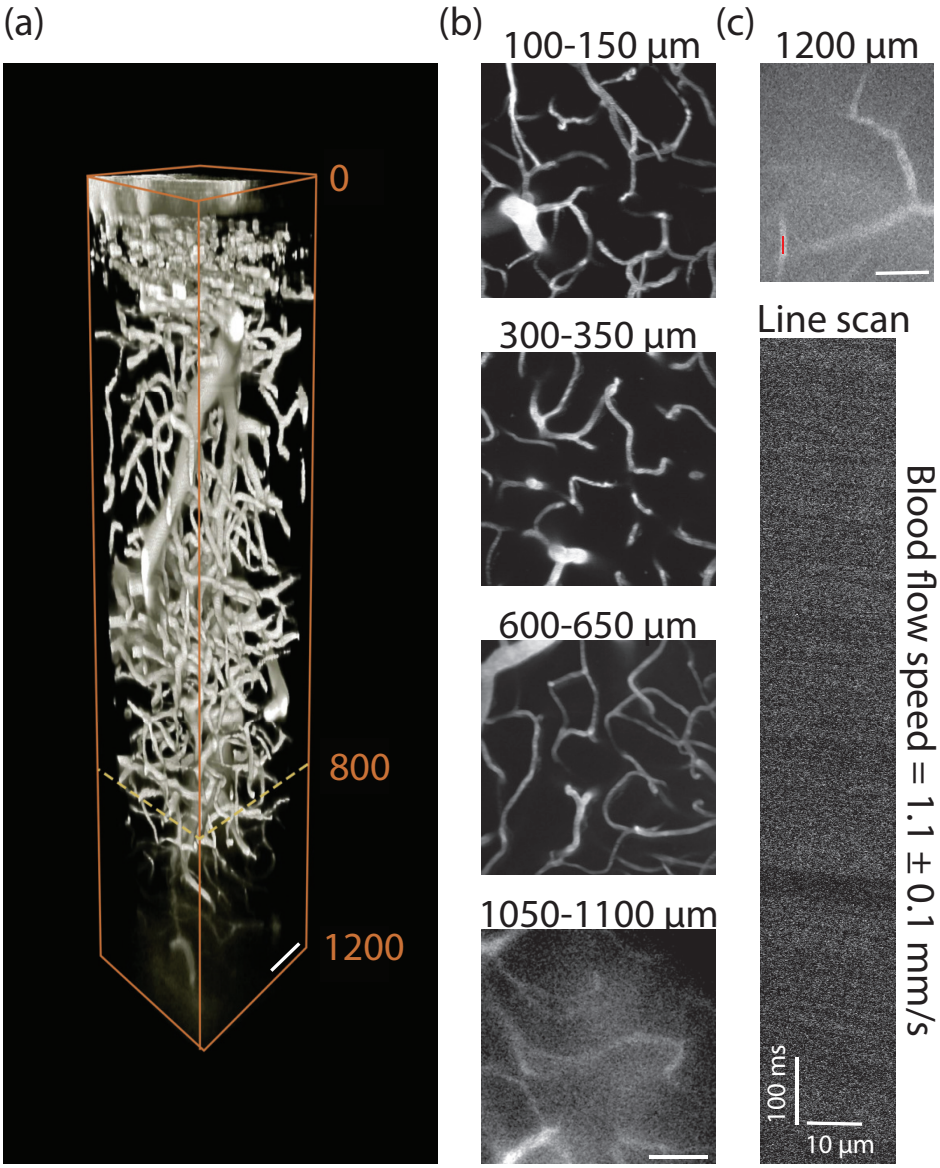


Figure 4.3: *In vivo* two-photon microscopy images of vasculature labeled with Texas Red. (**a**) 3D reconstruction of a 1,200 $\mu$m stack of vasculature labeled with Texas Red. (**b**) x-y intensity projections of stack shown in (a). (**c**) (top) x-y intensity projection at depth of 1,200 $\mu$m. A line scan was performed at the highlighted red line. (bottom) Line scan at depth of 1,200 $\mu$m. All scale bars are 50 $\mu$m unless otherwise indicated.

depth of 1,200 $\mu$m. During a line scan, the laser is scanned back and forth over a blood vessel, which causes red blood cells flowing through the vessel to appear as streaks. The streaks are analyzed to reveal the blood flow velocity in the vessel. In Fig. 4.3(c), the highlighted red line (top) indicates the position of the line scans (bottom). To the best of my knowledge, this is the deepest line scan performed *in vivo* to date. The blood flow speed was measured to be $1.1 \pm 0.1$ mm/s.

Figure 4.4(a) shows a 3D rendering of vasculature labeled with ICG to an imaging depth of 1,000 $\mu$m. Blood vessels can be resolved throughout the stack. Excitation power was increased to maintain similar signal levels down to 750 $\mu$m at which point full power was reached equating to 20 mW at the sample surface (the transmission of the 20X objective at 1,325 nm is 28%). ICG is FDA approved for human use and is commonly used for ICG angiography in ophthalmology; its far-red fluorescence emission near 830 nm reduces the scattering of the fluorescent light which makes it ideal for translational applications. I expect these results to be of particular interest to clinicians since ICG is FDA-approved as a contrast agent for humans and is a promising route to apply multiphoton microscopy to clinical applications [79, 80].

One draw back to ICG for deep imaging is its quick clearance time. I found that ICG was significantly cleared from cerebral vasculature after 30 minutes, which caused a heterogeneous distribution of fluorescence signal throughout the 3D reconstruction in Fig. 4.4(a). After the first injection of

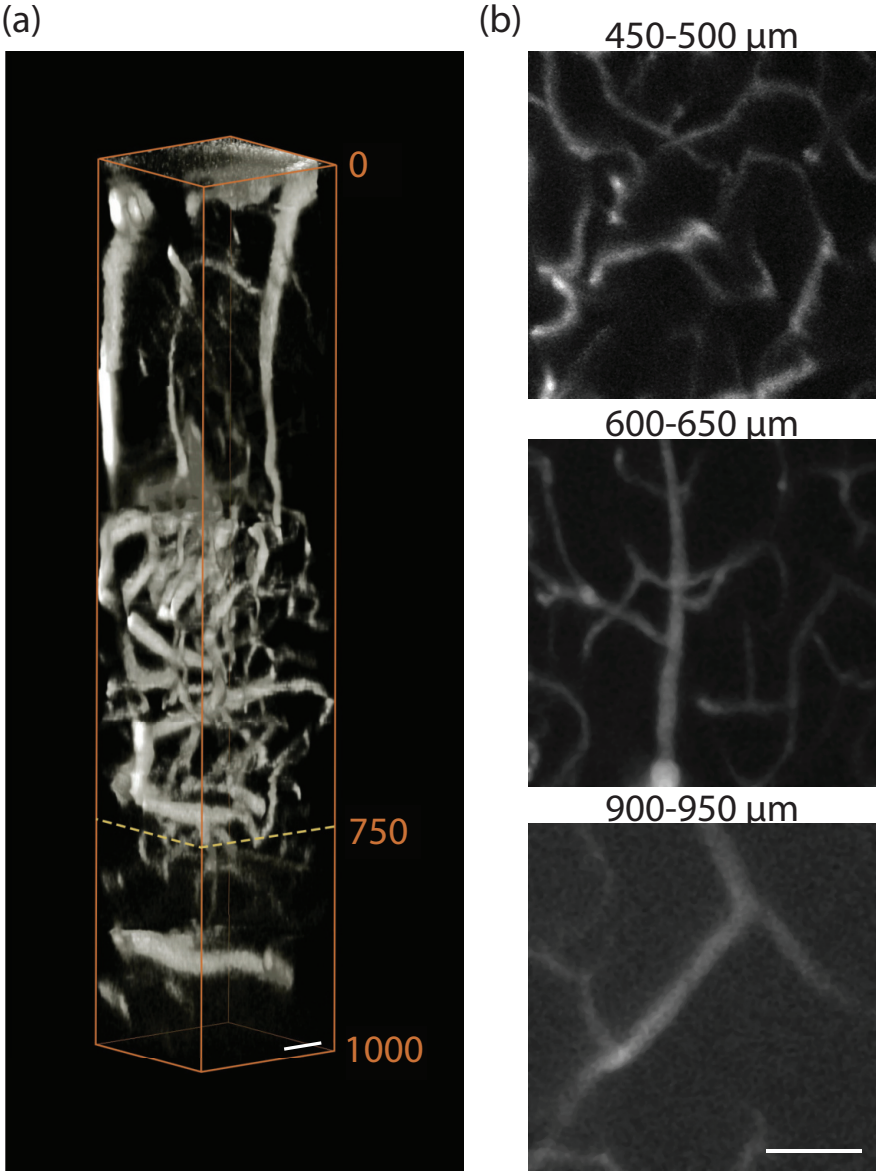


Figure 4.4: *In vivo* two-photon microscopy images of vasculature labeled with ICG. (**a**) Three-dimensional reconstruction of a 1,000 $\mu$m stack. (**b**) x-y intensity projections of stack shown in (a). All scale bars are 50 $\mu$m.

ICG, it took approximately 15 minutes to select a region of the brain without large surface vessels, which can cause significant out-of-focus fluorescence at deep imaging depths. Thus, the ICG dye had started to clear by the time the first 400 $\mu$m were imaged, which is why only large vessels are visible in the first 400 $\mu$m. At 400 $\mu$m, more ICG was injected and then imaging began immediately afterwards; thus, there is a clear increase in signal starting at 400 $\mu$m. Only two injections of ICG were performed to avoid injecting more than 20% of the mouse's total blood volume, which limited the number of frames over which I could average such that the stack could be acquired before the dye cleared. I performed a 5 frame average from 0 to 700 $\mu$m below the surface, 8 frame average from 700 to 800 $\mu$m, 10 frame average from 800 to 900 $\mu$m, and 12 frame average from 900 to 1,000 $\mu$m.

Figure 4.5 shows a 3D rendering from a second imaging session of vasculature labeled with ICG, again demonstrating the repeatability of the OPA for deep-tissue imaging. Excitation power at $\lambda$=1,350 nm was increased to maintain similar signal levels down to 750 $\mu$m at which point full power was reached equating to 58 mW at the sample surface (the transmission of the 25X objective at 1,350 nm is 74%). All frames throughout the stack were normalized individually. Figure 4.4(b) shows x-y intensity projections of the stack. Individual vessels can be seen with high contrast throughout the first half of the stack. The quick clearance of the ICG dye severely limited frame averaging throughout the stack. For the 3D reconstruction in Fig. 4.5(a), I performed a 6 frame average from 0 to 400 $\mu$m below the surface, 12 frame average from

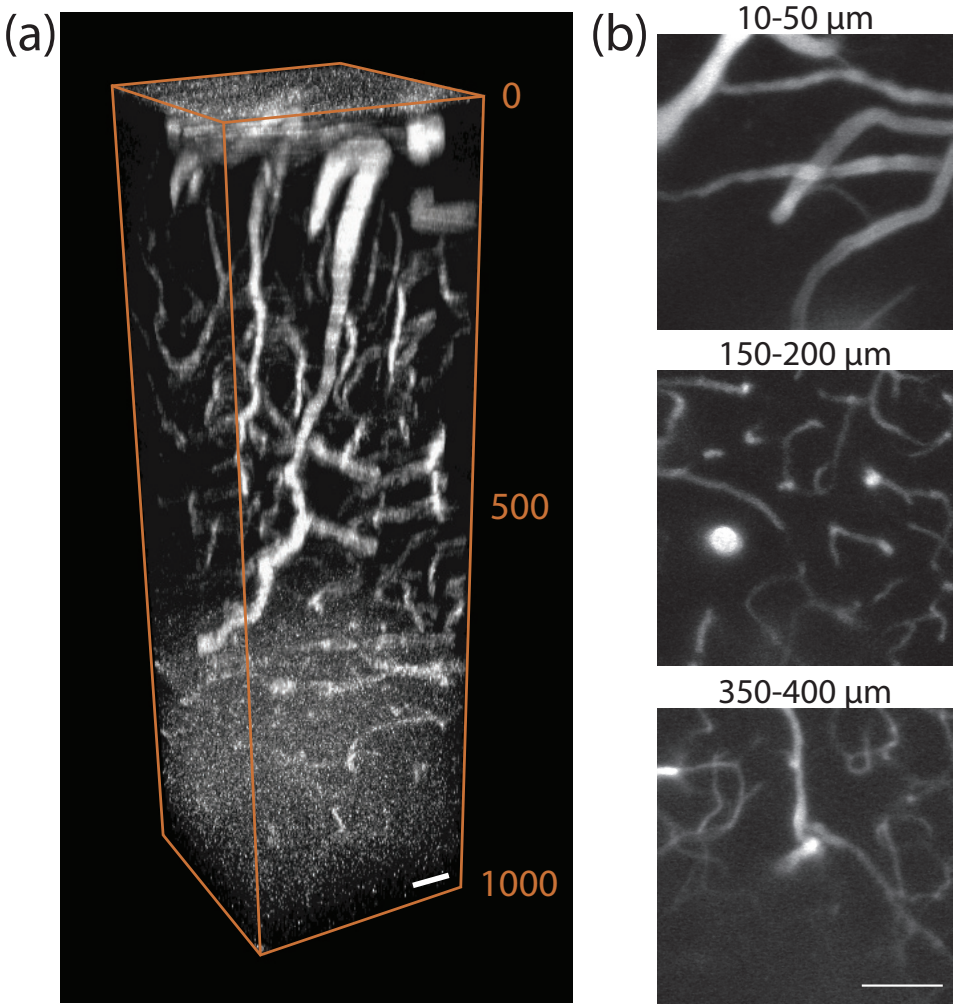


Figure 4.5: *In vivo* two-photon microscopy images of vasculature labeled with ICG. (a) Three-dimensional reconstruction of a 1,000 $\mu$m stack. (b) x-y intensity projections of stack shown in (a). All scale bars are 50 $\mu$m.

400 to 750 $\mu$m, and 15 frame average from 750 to 1,000 $\mu$m. Thus, the ICG dye was nearly cleared during the acquisition of the stack from about 700 $\mu$m to 1,000 $\mu$m which resulted in poor signal at these depths.

## 4.4 Neuron Imaging

Figure 4.6(a) demonstrates an imaging depth of 1,160 $\mu$m in neurons expressing tdTomato. Excitation power was increased to maintain similar

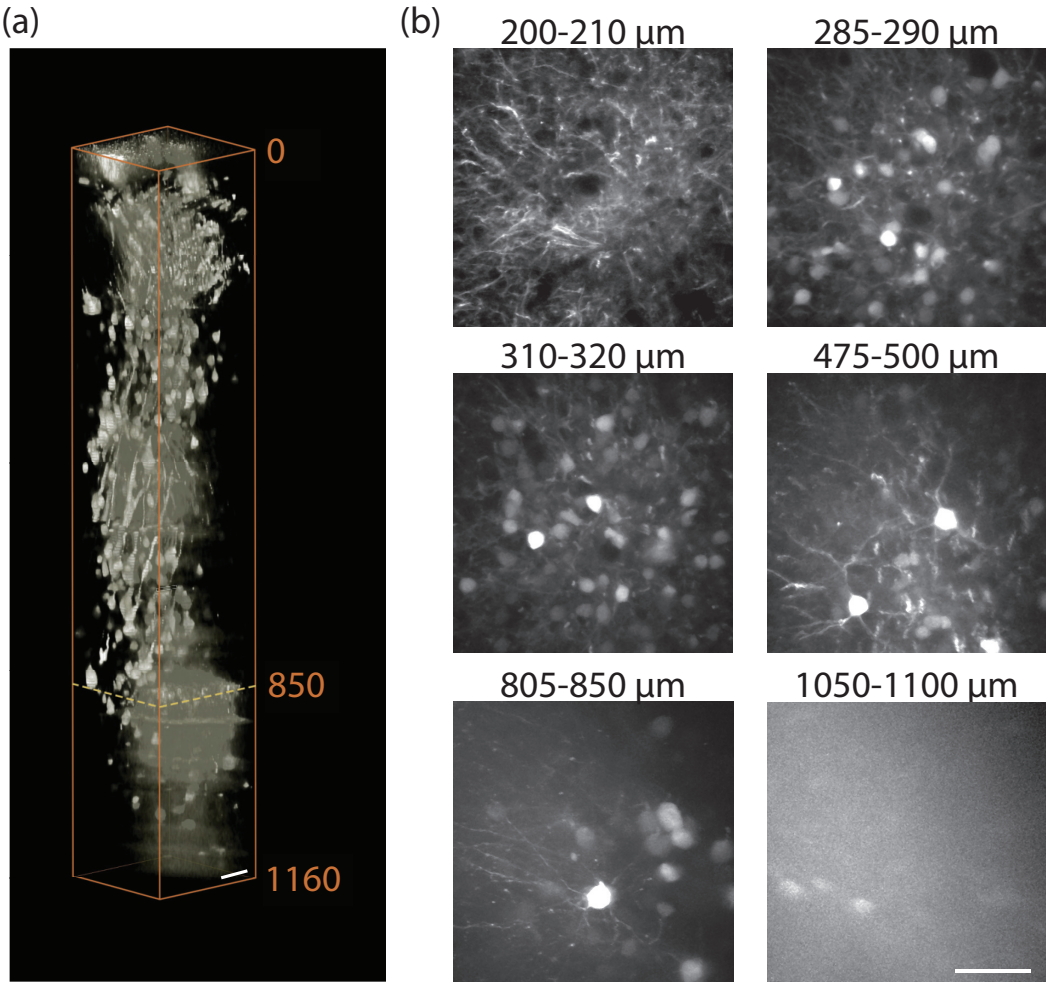


Figure 4.6: *In vivo* two-photon microscopy images of neurons labeled with td-Tomato. (**a**) Three-dimensional reconstruction of a 1,160 $\mu$m stack of neurons within a mouse brain. (**b**) x-y intensity projections from stack shown in (a). All scale bars are 50 $\mu$m.

signal levels down to 850 $\mu$m at which point full power was reached equating to 40 mW at the sample surface (the transmission of the 20X objective at 1,140 nm is 52%). The delivery of tdTomato causes roughly a 200 $\mu$m by 200 $\mu$m transverse area of expression after a week following injection. The expression is strongest in the center of the transverse area, which is why the 3D reconstruction in Fig. 4.6(a) appears saturated in the transverse center. Individual neuron bodies and their dendrites are visible throughout the stack, as shown in the x-y intensity projections in Fig. 4.6(b). Fluorescent proteins like tdTomato have the advantage that they are not cleared, and they are typically much brighter than fluorescent dyes. For the 3D reconstruction of neurons labeled with tdTomato in Figure 4.6(a), I averaged for 5 frames from 0 to 800 $\mu$m, 8 frames from 800 to 900 $\mu$m, 20 frames from 900 to 1,000 $\mu$m, and 25 frames from 1,000 to 1,1600 $\mu$m.

The previous imaging results were acquired at imaging sites 2.5 mm posterior and 2.5 mm lateral to the bregma. To investigate deep-tissue imaging closer to the bregma, I performed simultaneous imaging of Texas Red and YFP at a site 0.25 mm anterior and 1.5 mm lateral to the bregma, which is the most responsive forelimb region of the motor cortex [81]. Figure 4.7(a) shows a laser speckle contrast image of the mouse craniotomy - the red square indicates the two-photon imaging location. The bottom of Fig. 4.7(a) is a 300×300×400 $\mu m^3$ two-photon maximum intensity projection of the surface vasculature outlined by the red square. Figure 4.7(b) is an x-z intensity projection for a 1,330 $\mu$m stack acquired at the site outlined by the red square

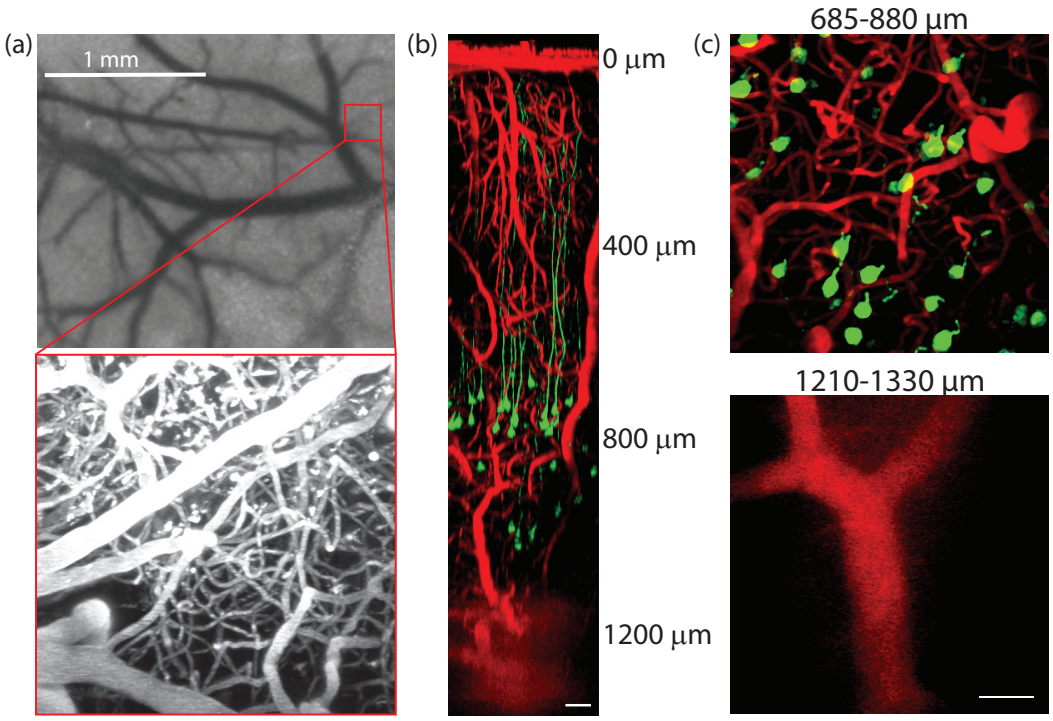


Figure 4.7: *In vivo* two-photon microscopy images of vasculature labeled with Texas Red and neurons labeled with YFP. (a) Laser speckle contrast image of mouse craniotomy. The red square indicates the two-photon imaging location. The zoomed view is a 300 × 300 × 400 $\mu$m$^3$ two-photon maximum intensity projection. (b) x-z intensity projection of a 1,330 $\mu$m stack of vasculature (red) and neurons (green). (c) x-y intensity projections of stack shown in (b) demonstrating neuron cell bodies in layer V and a large blood vessel at a depth of 1,330 $\mu$m. All scale bars are 50 $\mu$m unless otherwise indicated.

in Fig. 4.7(a). The vasculature (red) can be seen throughout the stack and the neurons (green) can be traced down to their cell bodies in layer V. For the 3D reconstruction in Fig. 4.7(b), I averaged for 3 frames from 0 to 745 $\mu$m, 6 frames from 750 to 1,000 $\mu$m, 12 frames from 1,000 to 1,300 $\mu$m, and 18 frames from 1,300 to 1,330 $\mu$m. The top image of Fig. 4.7(c) is an x-y

intensity projection showing the neuron cell bodies in layer V (green) overlaid with the microvasculature (red). The bottom image of Fig. 4.7(c) depicts a vessel at an imaging depth of 1,330 $\mu$m. I note that the OPA excitation wavelength was tuned to $\lambda$=1,280 nm which causes two-photon excitation of Texas Red and three-photon excitation of YFP; thus, the stack demonstrates simultaneous imaging of Texas Red undergoing two-photon absorption and YFP undergoing three-photon absorption.

## 4.5 Discussion of *In Vivo* Imaging Results

There are two primary advantages of the OPA laser system for deep imaging. First, the OPA wavelength can be tuned between 1,100 and 1,400 nm to match the peak two-photon or three-photon absorption of the target fluorophore. The wide tuning range allows for the excitation of numerous different fluorophores, as demonstrated in Figs. 4.1-4.7 with Texas Red, ICG, tdTomato, and YFP. Second, the regenerative amplifier can operate at a repetition rate up to 511 kHz while maintaining the same pulse energy as at lower repetition rates. Ti:sapphire based regenerative amplifiers typically used in other literature for multiphoton microscopy run at repetition rates at or below 250 kHz [26, 82]. Running at a faster repetition rate while maintaining a high pulse energy enables faster image acquisition and better signal-to-noise ratio. This is demonstrated in Fig. 4.2 for which I show there is an approximate $\sqrt{2}$ gain in SBR by doubling the repetition rate for depths between 300 and 600 $\mu$m, and interestingly, an even greater gain at deeper depths. Combining both

of these advantages - high pulse energy and long excitation wavelengths at which scattering in the mouse brain is minimized - enables the OPA system to extend the traditional imaging depth of 2PM and routinely obtain high quality images of vessels and neurons labeled with a variety of fluorescent dyes and proteins deep in mouse brain tissue.

The advantages of the OPA system add significant cost and complexity to the laser system. Many laboratories and clinics may prefer a simpler system that is more affordable and easier to use, though these systems typically lack the ability to tune the excitation light source. However, the cost and complexity enables new investigations into vascular morphology and dynamics. For example, I demonstrate an imaging depth beyond 1.5 mm (shown in Fig. 4.1) with 5 $\mu$m axial steps. Using fine axial steps, I capture the continuous changes of vasculature morphology and can track the centerlines of the vessels throughout the stack (shown in Fig. 4.2(a)). Another group has reached similar depths - 1.6 mm using 1,280 nm excitation light at 80 MHz (1.5 nJ pulse energy) to excite Alexa680 [27] - however, they average up to 224 frames to account for the low pulse energy and take 20 $\mu$m axial step sizes in order to capture the stack in a practical time limit. Large frame averaging and z-step sizes are not a practical method to chronically study vascular dynamics and morphology.

I am also able to discern functional information about the vasculature at depths beyond 1 mm. I determined the blood flow speed in a single vessel at a depth of 1.2 mm (shown in Fig. 4.3(c)), which can be useful for characterizing the health of blood vessels. The previous reported deepest line scan was at a

depth of 900 $\mu$m performed with a 82 MHz oscillator at 1,280 nm [6]; since line scans must be performed with little to no averaging in order to capture the dynamics of blood flow, a high pulse energy laser like the OPA is able to achieve better SBR in deep tissue and thus record deeper line scans.

An important consideration in choosing a fluorescent dye to label vasculature is the clearance time of the dye. Ideally, a dye would maintain a similar concentration in the blood plasma for the duration of an imaging session. However, dyes that clear quickly may limit the maximum pixel dwell time and frame averaging. I found that ICG was significantly cleared after 30 minutes which severely limited frame averaging throughout both deep imaging stacks in Figs. 4.4 and 4.5. It took approximately 90 minutes for Texas Red to clear, allowing for reasonable frame averaging in Figs. 4.1, 4.3, and 4.7. Fluorescent proteins like YFP and tdTomato have the advantage that they are not cleared, and they are typically much brighter than fluorescent dyes. For the 3D reconstruction of neurons labeled with tdTomato in Fig. 4.6, frame averaging was not an issue but instead the over-expression of tdTomato caused the image to appear saturated. Optimizing the expression of a fluorescent protein can be difficult yet is crucial for deep-tissue imaging. One strategy is to deliver the fluorescent protein only at imaging depths near 1 mm and not at shallower depths, thus there is limited out-of-focus fluorescence at the shallow imaging depths when the beam is focused to 1 mm below the surface. I had mixed success with this approach because it can be difficult to find the localized area of expression; however, Ouzounov et al. demonstrate the utility

of this technique by imaging hippocampal neurons labeled with an AAV virus injection [28].

Imaging depth could be significantly improved with the development and characterization of new fluorophores that are optimized to have their peak two-photon absorption near 1,300 nm at which the attenuation length in mouse brain cortex is maximized. Additionally, it would be advantageous for these fluorophores to have red-shifted emission spectra (similar to that of ICG) to reduce the attenuation of fluorescent photons traveling from the excitation volume to the microscope objective. I characterized the brightness of Texas Red and ICG, though neither are exceptionally bright fluorophores. Texas Red is an affordable option for deep imaging near 1,300 nm but not extremely bright, while Alexa680 is significantly brighter [6] but more expensive. Unfortunately, few other fluorophores have been characterized for excitation wavelengths beyond 1,100 nm. Future work in the MPM field should aim to identify and characterize fluorescent dyes that are both brighter near an excitation of 1,300 nm and more cost-effective.

# Chapter 5

# What is the Maximum Imaging Depth for Multiphoton Microscopy?

## 5.1 Theory of Limiting Factor for Imaging Depth

There are two competing theories to determine the maximum imaging depth, $z_{\max}$, for 2PM. The first defines the maximum imaging depth when the signal to background ratio (S/B), defined as

$$\frac{S}{B} = \frac{2\pi(NA)^2}{\lambda n l_s} z^2 \exp(-2z/l_s) \ , \tag{5.1}$$

becomes unity [26]. Here, $NA$ is the numerical aperture of the objective, $\lambda$ is the excitation wavelength, $n$ is the index of refraction of the medium, and $l_s$ is the scattering length of mouse brain cortex. The underlying assumption for this theory is that out-of-focus fluorescence generated at the surface due to the increasing beam cross section at the surface eventually overpowers the fluorescent signal generated at the focus. While this condition is certainly true if there are large surface blood vessels above the focus, the situation can be avoided by finding brain regions with no large surface vessels.

The second theory bases the maximum imaging depth on the signal-to-noise ratio, not the signal-to-background ratio. The maximum imaging depth

is defined as

$$z_{\max} = l_s \ln\left[\sqrt{\frac{\sigma_2}{n_{\min}\tau f}}\frac{\pi(NA)^2}{hc\lambda}\langle P\rangle\right], \tag{5.2}$$

where $\sigma_2$ is the two-photon absorption cross section, $n_{\min}$ is the minimum number of photon pairs absorbed per fluorophore per unit time, $\tau$ is the pulse width, $f$ is the repetition rate of the laser, $h$ is Planck's constant, $c$ is the speed of light in vacuum, and $\langle P\rangle$ is the average power of the laser [26]. This equation is more accurate as it accounts for the brightness of the target fluorophore $\sigma_2$ as well as the laser characteristics $f$ and $\tau$. The imaging results presented in Chapter 4 support this theory, indicating that for excitation pulses with high energy like the OPA, the limiting factor for imaging depth is the signal-to-noise ratio. This is in contract to excitation pulses with low energy but high repetition rate where the limiting factor for imaging depth may be the signal-to-background ratio.

## 5.2 Modeling Maximum Imaging Depth

To evaluate whether Eq. 5.2 agrees with experimental results, I evaluated $z_{\max}$ for a Ti:S oscillator, regenerative amplifier, optical parametric oscillator (OPO), and optical parametric amplifier for typical laser parameters shown in Table 5.1.

Figure 5.1 shows the maximum imaging depth for each laser assuming a numerical aperture of $NA$=1.0, fluorophore two-photon cross section of $\sigma_2$=50

Table 5.1: Imaging parameters used for modeling the maximum imaging depth for a titanium-doped sapphire oscillator (Ti:S), regenerative amplifier (RegA), optical parametric oscillator (OPO), and optical parametric amplifier (OPA). Note that $\langle P \rangle$ is the average power at the sample surface.

| | Ti:S | RegA | OPO | OPA |
|---|---|---|---|---|
| $f$ (MHz) | 76 | .250 | 80 | .500 |
| $\tau$ (fs) | 100 | 100 | 140 | 100 |
| $\langle P \rangle$ (mW) | 560 | 45 | 120 | 30 |
| NA | 1.0 | 1.0 | 1.0 | 1.0 |
| $\sigma_2$ (GM) | 50 | 50 | 50 | 50 |

GM, and $n_{min}$ such that

$$\frac{n_{min}}{f} \cdot N_p \cdot N_f = 50 \ , \tag{5.3}$$

where $N_p$ is the number of pulses per pixel and $N_f$ is the number of frames averaged at the maximum imaging depth.

Figure 5.1 is in general agreement with experimental results. The predicted maximum imaging depth for a: Ti:S oscillator is around 800 $\mu$m as found in [22], regenerative amplifier is around 1,000 $\mu$m as found in [26], and OPO is around 1,500 $\mu$m as found in [27]. The maximum imaging depth of the OPA is predicted to be about 150 $\mu$m more than the OPO at each wavelength, a result of higher energy pulses penetrating deeper into tissue. The imaging results displayed in Chapter 4 demonstrate an imaging depth of 1,535 $\mu$m, which is about 100 $\mu$m from the theoretical limit of 1,650 $\mu$m (assuming a 50 GM fluorophore). This demonstrates that the OPA results approach the predicted theoretical imaging depth limit. However, this model is highly sensitive to the imaging parameters. I modeled the OPA for typical daily operation

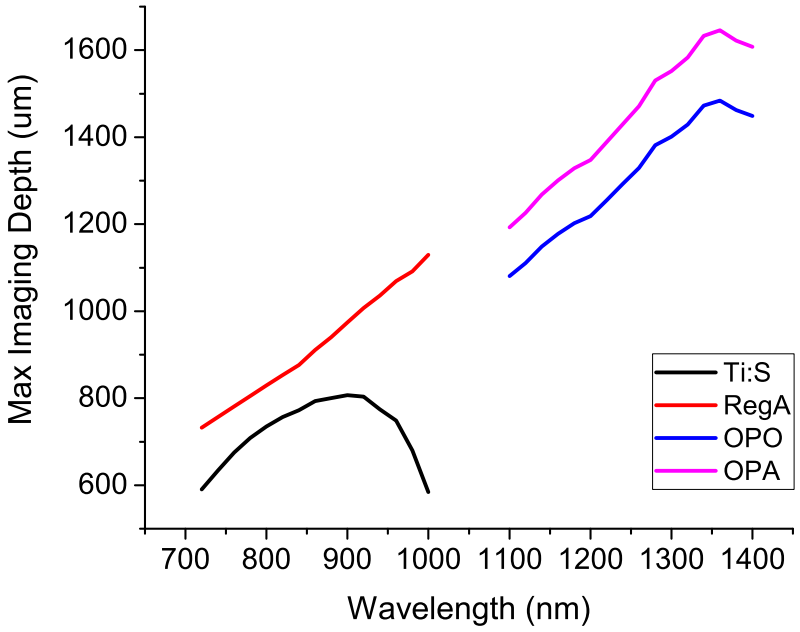


Figure 5.1: Maximum imaging depth for a Ti:S oscillator, regenerative amplifier (RegA), optical parametric oscillator (OPO) and amplifier (OPA).

laser parameters of $\tau$=100 fs and $\langle P \rangle$ = 30 mW at the back surface; however, the OPA can be optimized to have $\tau$= 42 fs (see Fig. 2.2) and $\langle P \rangle$=122 mW at the sample surface at 1,215 nm with the 25X objective, and indeed it is at these optimized laser parameters that I achieved an imaging depth of 1,535 $\mu$m, however the fluorophore brightness was significantly less than 50 GM.

Figure 5.1 assumes a fluorophore brightness of 50 GM, however it would be useful to characterize the imaging depth for each individual fluorophore based on its wavelength-dependent two-photon action cross section. A complete characterization of the brightness combined with a model predicting max-

imum imaging depth will help to identify the optimal wavelengths for deep imaging. Another parameter to consider is the wavelength-dependent output power of the OPA (only the Ti:S oscillator power was modeled as wavelength-dependent in Figure 5.1). A future model should incorporate the wavelength dependence of both absorption cross sections and laser power to better predict the maximum imaging depth of a laser system and its target fluorophore.

## 5.3 Toward Reaching the Maximum Imaging Depth for Multiphoton Microscopy

Maximizing the imaging depth limit for MPM requires optimizing the many variables that affect imaging depth. As indicated in Eq. 5.2, imaging depth depends on the excitation wavelength and the corresponding wavelength-dependent scattering length of mouse brain cortex, the brightness of the fluorophore, the numerical aperture of the objective and the immersion liquid, and the laser repetition rate, pulse width, and output power. Additionally, there are many more subtle parameters that affect the imaging depth such as the laser beam quality and alignment accuracy, the design and alignment of the scan optics and collection optics, and the wavelength-dependent absorption length of mouse brain cortex. Further, there are many practical considerations that impact imaging depth. These include the quality of the craniotomy and clarity of the optical window; inflammation due to the craniotomy surgery can severely hamper imaging depth and image quality. To maximize MPM imaging depth, each parameter needs to be optimized. These parameters can be

classified into four areas: laser, microscope, fluorophore, and animal parameters.

### 5.3.1 Laser parameters

The laser parameters to optimize for deep imaging include excitation wavelength, repetition rate, pulse width, and power output. As identified in Fig. 1.2, the optimal excitation wavelengths are $\lambda$=1,300 nm and 1,700 nm. The optimal repetition rate and output power are linked by the total amount of laser energy reaching the focal volume. Too much energy can cause harm to the mouse due to ablation. The laser ablation threshold is defined as the "minimum laser energy per unit surface (fluence) required to induce detectable changes in the material" [83]. In practice, it is obvious during MPM imaging when the laser power is significantly above the laser ablation threshold as cavitation bubbles appear in the image. Based on measurements of the laser ablation threshold in porcine corneal stroma [83], I estimate that the laser ablation threshold for mouse brain tissue across the OPA wavelength spectrum is 2 J/cm$^2$. The focused beam area for the OPA is about 1 $\mu$m$^2$, corresponding to a maximum pulse energy of 20 nJ to reach the laser ablation threshold of 2 J/cm$^2$. This is within close agreement to Tsai et al.'s calculation which estimates the ablation threshold to be 10 nJ for a 100 fs pulse focused to a 1 $\mu$m$^2$ area. These calculations are within the limits of experimental results presented by Nishimura et al. in which they found that a minimum pulse energy of 30 nJ was required to cut a vessel such that fluorescent dye

leaked out of the vessel but the vessel remained intact [84]. I used 20 nJ as the pulse energy upper limit within a focal volume for imaging experiments performed in Chapter 4.

While it is important to not exceed the laser ablation threshold, the laser pulse energy should be sufficiently high to saturate the focal volume to generate as much fluorescence signal as possible without causing any damage. The saturation pulse energy for ultrafast pulses for n-photon excitation, derived following [7, 10], is:

$$\frac{\langle P(t)\rangle}{f} = \left(\frac{\lambda^{2n}\tau^{n}}{g_p^n \sigma_n \pi^n \tau (NA)^{2n}}\right)^{1/n} . \tag{5.4}$$

For two-photon excitation (n=2), the saturation pulse energy is:

$$\frac{\langle P(t)\rangle}{f} = \frac{\lambda^2\sqrt{\tau}}{\pi (NA)^2 \sqrt{g_p^2 \sigma_2}} . \tag{5.5}$$

For parameters $\lambda$=1,300 nm, $\tau$=50 fs, $NA$=1.0, and $\sigma_2$=10 GM, the saturation pulse energy is 0.7 nJ for the OPA, which is well below the ablation threshold of 20 nJ. Performing this calculation for each imaging setup and controlling the power throughout the entire stack to ensure that the saturation pulse energy is achieved at each Z-position is a crucial step to not only maximizing imaging depth but also achieving high image quality throughout the stack; the 3D reconstructed stack may look disjointed if the pulse energy reaching the focal volume is not maintained at a near constant value - the saturation pulse energy for optimized deep imaging. The expected attenuation of the light in the mouse cortex can be predicted using the effective attenuation length [23].

As imaging depth increases resulting in more attenuation of the excitation light, the pulse energy will eventually drop below the saturation pulse energy due to the limitation of output power of the laser. Fortunately, OPA lasers with ever higher output power are becoming increasingly common due to advances in non-collinear OPA technology.

In regard to temporal pulse width, imaging depth is optimized when pulse widths are as short as possible meaning they are Fourier-transform limited. It is important to note that the pulse should be Fourier-transform limited at the focal volume. As demonstrated in Fig. 2.1, prisms can be used to pre-chirp the pulse such that the pulse is nearly Fourier-transform limited after the objective. Ideally, the pulse would also be pre-chirped by some amount to account for the pulse broadening within the mouse brain, however this is difficult to determine. For pulses that are 50 fs or greater, the dispersion for 1 mm of brain tissue should not be large; however for pulses on the order of 10 fs, dispersion may be a factor to consider.

### 5.3.2 Microscope parameters

Microscope parameters that affect imaging depth include the microscope objective numerical aperture, transmission, and immersion liquid, and the design and alignment of the scan optics and collection optics.

High numerical aperture objectives are crucial for efficient multiphoton excitation and low magnification is necessary for increased collection of the fluorescence signal. Oheim et al. [85] demonstrate an order of magni-

tude increase in fluorescence collection in deep-tissue using a 20X objective ($NA$=0.95) versus a 63X objective ($NA$=0.90).

The transmission of the microscope objective is important to consider as it can have a significant impact on the power at the sample surface. The common objective used for *in vivo* MPM imaging is the Olympus XLUMPLFLN20XW, referred to as 20X. The 20X objective has relatively high transmission between 700 and 1,000 nm, making it the typical selection for *in vivo* MPM imaging with Ti:S oscillators. It peaks at 75% transmission near 700 nm and drops to 60% at 1,000 nm. For wavelengths beyond 1,000 nm, the objective's transmission falls off significantly as it was not designed for long wavelengths. Recently, Olympus developed the XLPLN 25X series for MPM imaging with longer wavelengths. The series has coatings optimized for 1600 nm that significantly boosts the transmission for wavelengths beyond 1,000 nm.

The series has the option for a 2, 4, or 8 mm working distance. The working distance defines the maximum imaging depth as the objective collides with the cranial window about 100 - 300 $\mu$m before the imaging depth matches the working distance depending on the thickness of the cranial window and angle of the brain relative to the objective. Additionally, the objective body may collide with the craniotomy at shallower imaging depths. I note that the 20X objective has a working distance of 2 mm. During a few deep-tissue imaging experiments, I found the objective body of the 20X collided with the sides of the craniotomy near an imaging depth between 1 and 1.5 mm. For

this reason, a longer working distance can be favorable, such as 4 mm.

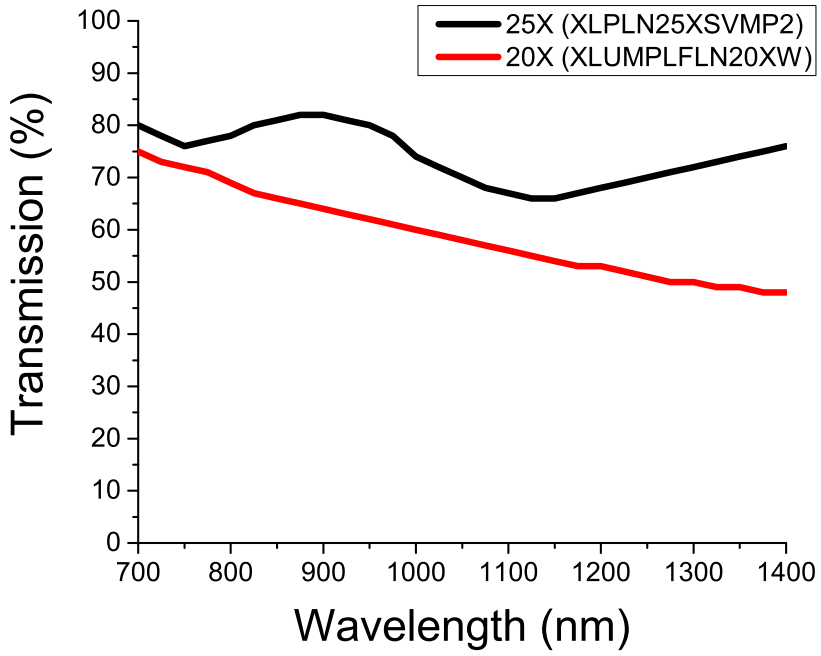


Figure 5.2: Comparison of the transmission for the Olympus 25X (XLPLN25XSVMP2) and 20X (XLUMPLFLN20XW) microscope objectives from 700 to 1,400 nm.

I performed many imaging experiments with the 4 mm working distance XLPLN 25X objective (XLPLN25XSVMP2), referred to as 25X, to explore the possibility of imaging deeper than 2 mm. While I did not exceed 2 mm, I did record an imaging depth of 1,535 $\mu$m as shown in Fig. 4.1. The transmission of the 25X objective across the OPA spectrum is greater than 65%. Figure 5.2 compares the transmission of the 25X and 20X objective. At 1,300 nm, the 25X objective has a transmission of 72%, far better than the 20X which has a

transmission of 50% at 1,300 nm. I note here that Figs. 4.1, 4.5, and 4.7 were acquired with the 25X objective and Figs. 4.3, 4.4, and 4.6 were acquired with the 20X objective.

An additional advantage of the 25X objective is the correction collar which adjusts for the index mismatch of water and brain tissue. The correction collar can account for an index of refraction of 1.33 to match water and up to 1.41 to match brain tissue. In practice, I set the collar to the water setting (all the way to the left when the objective is positioned in an upright microscope) and rotate the collar to the right with increasing imaging depth. By inspecting the live image while rotating the collar, the image brightness can be optimized indicating optimized index matching. I typically rotate the collar every 200 to 400 $\mu$m depending on the goals of the imaging session. The collar should be rotated to the right as imaging depth increases, which compensates for the rising refractive index that the excitation beam travels when focused deeper into the brain.

A practical disadvantage of the 25X objective is the large 4 mm working distance. It can be difficult to get a 4 mm column of water to stay throughout an imaging session, and typically imaging sessions required multiple applications of water. It is important to maintain a column of water between the objective tip and the cranial window regardless of the working distance as this is necessary to achieve the full numerical aperture of the objective for both the excitation light, and even more importantly, the fluorescence signal.

Both the 20X and 25X Olympus objectives use water for the immersion

liquid. For *in vivo* deep-tissue experiments, heavy water ($D_2O$) should be used instead of normal water ($H_2O$) to reduce the absorption of the excitation light by the immersion liquid, thus increasing the laser power that reaches the focal volume. All images presented in Chapter 4 used heavy water as the immersion liquid. Heavy water absorbs significantly less than water across the OPA spectrum; the absorption coefficient of heavy water near 1,300 nm is about an order of magnitude less than normal water [86].

Maximizing imaging depth also depends on the design and alignment of the laser beam, scan optics, and collection optics. The scan optics should be designed to maximize the power reaching the sample surface at all scan angles as well as minimize aberrations and vignetting. Optical coatings optimized for wavelength regions near 1,300 nm and 1,700 nm are becoming increasingly common with the rise in popularity of deep-tissue imaging at these wavelengths. Optimized coatings for both scan optics and mirrors can provide a significant increase in the power reaching the sample surface due to the number of optical elements typically contained within a multiphoton microscope and the number of mirrors used to steer the laser beam to the microscope. Similarly for collection optics, the design should maximize the number of fluorescence photons that reach the detector. One factor to optimize is the coatings for the expected fluorescence wavelengths, which are typically in the visible spectrum. A second factor is the size of the optics; two inch optics or larger can be used to minimize the number of vignetted fluorescent photons.

Practically, it is important to align the laser beam properly within the

scan optics. One quick check is to ensure there is no lateral displacement of the laser beam at the back aperture of the objective while scanning. Additionally, the collection optics should be aligned properly to maximize the system collection efficiency.

### 5.3.3 Fluorophore parameters

The selection of a bright, stable fluorophore is vital for routine *in vivo* deep-tissue MPM imaging. As discussed in Chapter 1.7, the MPM community is currently engaged in developing and characterizing bright fluorophores at longer wavelengths near 1,300 and 1,700 nm. The current brightest option for vasculature labeling is Alexa680 which has an action cross section of around 55 GM at 1,300 nm [6], however Alexa680 is quite expensive relative to other fluorescent dyes; further, the action cross section value has only been measured by one group and has an expected error bar of 30%. Fluorescent proteins tend to be brighter than fluorescent dyes, however few have been developed for longer excitation wavelengths. A fluorescent dye and fluorophore with action cross section values on the order of 100 GM at 1,300 nm would be beneficial for deep imaging. Additionally, a fluorescent dye that does not clear quickly and has a red-shifted fluorescence wavelength would add to the increase in imaging depth. For fluorescent proteins, a more robust and controlled way to control expression would be beneficial.

### 5.3.4 Animal parameters

The importance of the preparation of the mouse craniotomy cannot be overstated. Regardless of the laser source, if the craniotomy preparation is poor, then imaging depth will be severely limited. Inflammation arises shortly after surgical implantation of the cranial window, if not during the surgery. In mice, there can be a short time window on the order of hours before inflammation is significant; however, this requires exquisite surgical expertise (provided in my case by Dr. Flor Medina and Ahmed Hassan). I experimented imaging immediately after surgery both with and without an optical window. Imaging depth in this situation was never as deep as waiting for about two weeks for the inflammation to recede. I suspect this is because imaging immediately after surgery puts significant stress on the mouse as the mouse is under anesthesia for a prolonged period.

Experimentally, I also found that imaging depth was typically greater for younger mice than older mice. This is seen in other literature as well and may be due to incomplete myelination of the brain tissue in young mice [85] which would result in a higher scattering length of the mouse brain tissue. Further, the scattering length and absorption length are not uniform in each brain region. In modeling the expected amount of photons to reach a particular imaging depth, such as 1 mm shown in Fig. 1.2, the brain tissue is often approximated to have a single effective attenuation length for an excitation wavelength. However, each layer of the brain has unique properties and thus different optical properties [23].

## 5.4 Looking Ahead

I conclude this chapter with an optimistic view of the future of optical microscopy. Microscopes are now ubiquitous in biological and neuroscience research. The imaging depth of optical microscopy has been rapidly advancing with the advent of multiphoton microscopy in 1991. While the theoretical limits appear to cap the imaging depth of *in vivo* MPM to around 2 mm, I suspect unforeseen technological advances will keep pushing the imaging depth deeper and deeper - likely through a combination of higher output power lasers, beam shape engineering, adaptive optics, brighter and more targeted fluorophores, sophisticated holographic or computational techniques to overcome scattering, and *in vivo* optical clearing methods. One predictive method is to use the analogy of Moore's law from electronics which predicts, based on past observations, that the number of transistors in an integrated circuit doubles every two years. The question pertinent with respect to multiphoton microscopy is the number of years to double the imaging depth. Imaging depth has approximately doubled every 10 years since its development in 1990; further, the image quality has also increased while the acquisition time of such images has fallen. Extrapolating this trend, I estimate that multiphoton microscopy or a derivate of the technique will be able to image the entire mouse brain, which is approximately 10 mm in diameter, in the next 25 to 35 years. This could fill a large gap in our understanding of the functional connectivity of the brain at the cellular level.

# Chapter 6

# Proof of Concept Studies

The custom MPM imaging system presented is a flexible system capable of novel imaging beyond extending the traditional imaging depth of 2PM. Here, I present proof of concept demonstrations for future research areas with the MPM system.

## 6.1 Tiled Multiphoton Microscopy Imaging

One approach to wide field of view MPM imaging is to tile individual 3D stacks together. Figure 6.1 is a 3×3 tiled two-photon microscopy image of vasculature labeled with Texas Red. Each individual stack is 440 $\mu$m × 440 $\mu$m in X and Y. For tiling the images, I used a 30% overlap such that the final tiled image is slightly larger than 1 mm × 1 mm in X and Y. The entire stack was taken to an imaging depth of 1 mm at 5 $\mu$m axial steps. Thus, the entire volume demonstrates a cubic millimeter volume of vasculature. Figure 6.1(b) shows a maximum intensity projection of the first 400 $\mu$m below the brain surface. Figure 6.1(a) is a laser speckle contrast image of the entire mouse brain surface; the red square indicates the location of the tiled two-photon image. A fiber laser at an excitation wavelength of $\lambda$=1055 nm was used to acquire

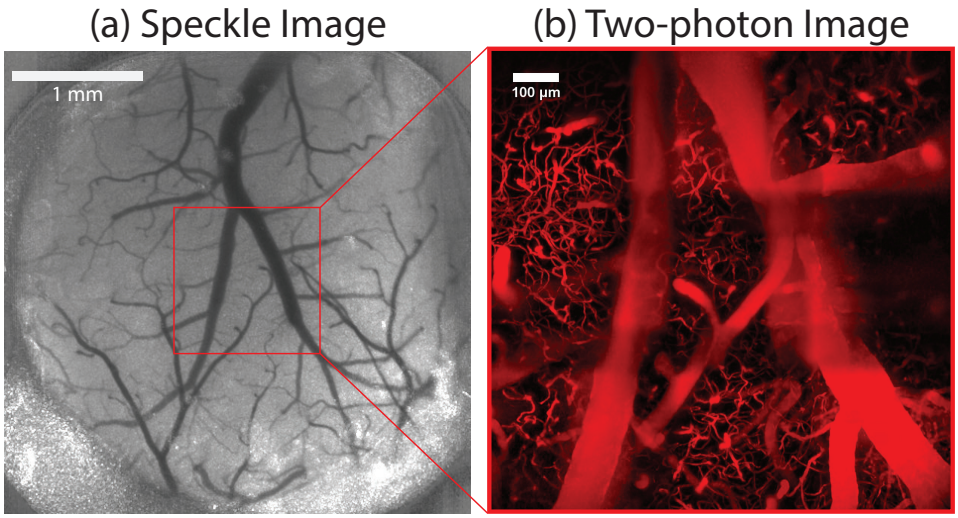


Figure 6.1: (a) Laser speckle contrast image of the entire mouse brain surface. The red square indicates the location of the tiled two-photon image. (b) Tiled 3×3 two-photon microscopy image of vasculature labeled with Texas Red.

the image in the presented MPM imaging system; the 25X objective was used. The tiled image has some artifacts from the tiling process; namely, the overlap at the edges of each individual stack causes some blurriness. This could be mitigated with smaller axial steps such as 1 $\mu$m instead of 5 $\mu$m. Additionally, the two large vein branches cause significant out-of-focus fluorescence nearby which reduces the image quality. Overall, however, the tiled image reveals the microvasculature and offers a promising route to image the entire mouse brain cortical volume.

## 6.2 Two-color Two-photon Imaging

Two-color two-photon (2C2P) imaging employs two synchronized ultrafast lasers of different wavelengths ($\lambda_1$ and $\lambda_2$) to cause two-photon excitation of a fluorophore, one photon from each laser [87]. The pulses are overlapped both spatially and temporally to excite the fluorophore at an effective wavelength $\lambda_3$ of

$$\lambda_3 = \frac{2}{\frac{1}{\lambda_1} + \frac{1}{\lambda_2}} \ . \tag{6.1}$$

Here, the term "two-color" refers to the two wavelengths of the laser. The advantage of the technique is that multiple fluorophores can be excited with the two lasers as simultaneous two-photon excitation is possible at all three wavelengths $\lambda_1$, $\lambda_2$, and $\lambda_3$.

I demonstrate the ability to perform 2C2P imaging with the OPA system presented in Fig. 2.1. The OPA converts the $\lambda_1$=800 nm regenerative Ti:S amplifier light to a longer wavelength. Since the OPA is synchronized with the regenerative Ti:S amplifier, the OPA wavelength $\lambda_2$ can be tuned from 1,100 to 1,400 nm to excite a fluorophore at any wavelength $\lambda_3$ between 926 and 1018 nm. I demonstrate the ability of the OPA system to excite YFP at an effective wavelength $\lambda_3$=960 nm with the OPA tuned to $\lambda_2$=1,200 nm. Figure 6.2 shows 2C2P imaging of neurons in fixed mouse brain tissue labeled with YFP; strong fluorescence is observed when the pulses are overlapped both spatially and temporally whereas the fluorescence decreases when a temporal delay is introduced.

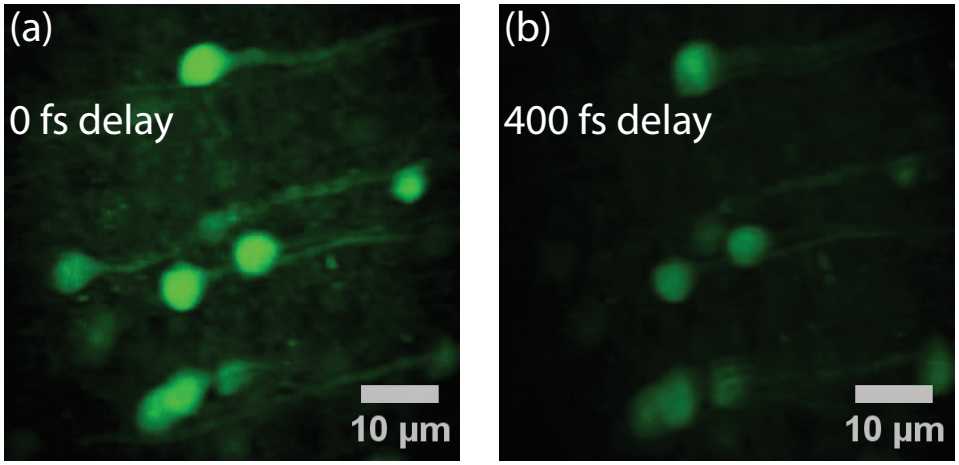


Figure 6.2: Two-color two-photon images of YFP labeled neurons in fixed mouse brain tissue acquired with the regenerative Ti:S amplifier at $\lambda_1$=800 nm and OPA at $\lambda_2$=1200 nm to excite YFP at an effective wavelength of $\lambda_3$=960 nm. Strong fluorescence is demonstrated in (a) when there is no delay offset between the OPA and regenerative Ti:S amplifier, whereas fluorescence decreases significantly in (b) with a temporal delay of 400 fs (equating to 120 $\mu$m pathlength difference) between the pulses.

## 6.3 Super-resolution Technique SLAM

An interesting feature of 2C2P excitation is the spatial profile of the excitation at the effective wavelength $\lambda_3$. The excitation spatial profile, called the point spread function (PSF), depends on the product of the spatial beam profile of both lasers. The PSF for $\lambda_3$ is dictated by the cross terms as seen in the expansion of the total two-photon excitation:

$$(I_1(\boldsymbol{r}) + I_2(\boldsymbol{r}))^2 = I_1^2(\boldsymbol{r}) + I_2^2(\boldsymbol{r}) + 2I_1(\boldsymbol{r})I_2(\boldsymbol{r}) \ . \tag{6.2}$$

Thus, the spatial product for the effective wavelength depends on a mixing of the spatial modes for $I_1$ and $I_2$. This is the central idea for a super-resolution

technique termed "Switching LAser Mode" microscopy or SLAM [88]. Akin to the more common super-resolution technique STED (Stimulated Emission Depletion) microscopy, SLAM uses PSF engineering to create a super-resolution effective spot size (meaning the spot size is smaller than the diffraction limit). SLAM subtracts a high-resolution image acquired with a typical bright beam with peak intensity at its center from a second image acquired with a PSF that has a dark spot at the center, referred to as the dark beam [88]. The resulting resolution of the subtraction image is defined by the size of the hole in the dark beam, similar to STED microscopy.

I explored combining 2C2P excitation with SLAM such that the bright beam and dark beam would be the result of 2C2P from the OPA and regenerative Ti:S amplifier (referred to as RegA). The bright beam is a combination of the RegA and OPA beams both in transverse electromagnetic mode $TEM_{00}$. The dark beam is a combination of the $TEM_{00}$ OPA beam and the $TEM_{01}$ RegA beam. The $TEM_{01}$ RegA beam mimics a doughnut shaped beam. I modeled several types of spatial beam profiles and computed the difference between the bright and dark beam. Beam profiles were computed using vectorial diffraction theory for high $NA$ objectives [89]. Figure 6.3 shows the PSF for the bright beam, dark beam, and difference for a subtraction factor $g$=0.7. Figure 6.3(b) shows the marked improvement in resolution of the difference PSF, which is the result of mode mixing of the spatial products of the beams. The model shows that the 2C2P effect improves the resolution by 1.8 times over typical 2PM. Further, the mode mixing effect enables a PSF of about 80

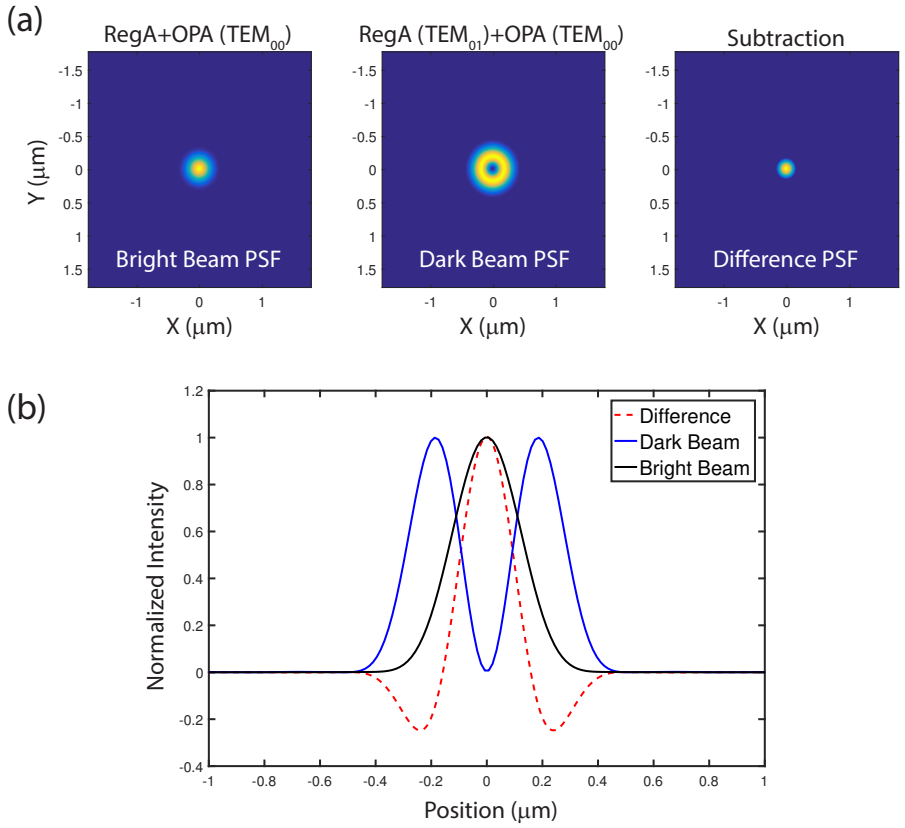


Figure 6.3: (a) The PSF of the bright beam, dark beam, and difference for a subtraction factor $g$=0.7. (b) Cross-section plot of the PSF position for the difference, dark, and bright beam demonstrating the improvement of the difference PSF.

nm, nearly a five times improvement over typical 2PM.

To implement 2C2P SLAM, I modified the laser and microscopy imaging system presented in Chapter 2. The setup is shown in Fig. 6.4. Both the regenerative Ti:S amplifier and OPA have temporal delay lines to properly align the beams temporally. The azimuthal polarizer (ARCoptix, Switzerland), a liquid-crystal device that can generate azimuthal polarization from

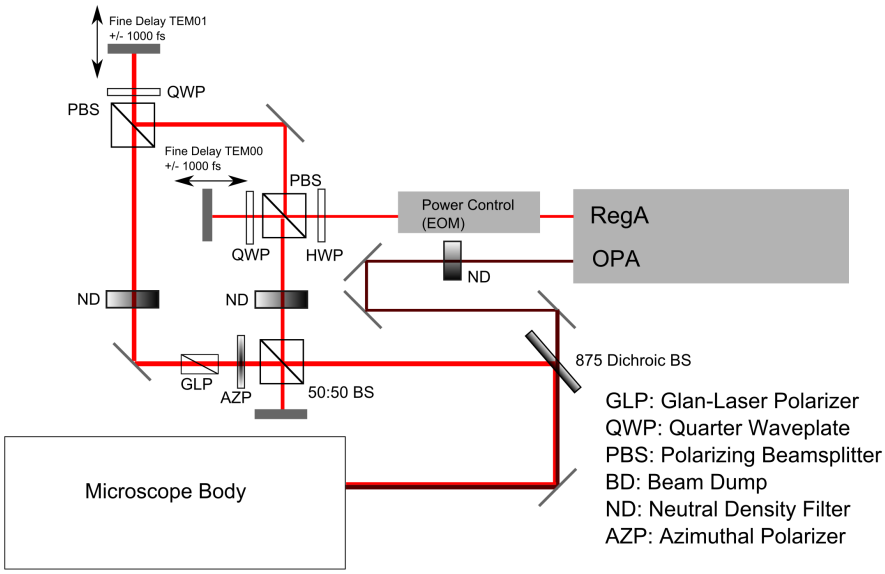


Figure 6.4: Laser schematic of the 2C2P SLAM setup.

linearly polarized light, creates the RegA doughnut beam. When azimuthally polarized light is focused with a high $NA$ objective, a doughnut shape is created similar to a $\mathrm{TEM}_{01}$ beam profile. The beams are recombined through a 875 nm dichroic beamsplitter (Semrock, FF875-Di01-25x36).

Future experiments will demonstrate the utility of 2C2P SLAM to image dendritic spines, which is challenging for 2PM due to the small size of dendritic spines on the order of 1 $\mu$m. Super-resolution imaging of spines with 2C2P SLAM will enable the characterization of morphological changes in dendritic spines induced by long-term potentiation.

## 6.4 Ruthenium Micelles for Oxygen Sensing

Measuring oxygen concentration levels in cerebral tissue is a useful proxy for tissue health, in particular for stroke studies. Here, I demonstrate the ability of the MPM system to measure fluorescence lifetimes of Ruthenium micelles to perform oxygen sensing. A Ruthenium complex $[Ru(dpp)_3]^{2+}$ encapsulated into a nanomicelle and coated with silica causes collisional quenching with oxygen [90], thus altering the lifetime of the micelle.

With the help of Dr. Andrew Fowler, I prepared a batch of Ruthenium micelles following the procedure outlined in [90]. A retro-orbital injection of 50 $\mu$L of the micelles at a concentration of 0.3 $\mu$M was performed to perform *in vivo* MPM imaging of the vasculature and lifetimes within a mouse. MPM imaging was performed with the regenerative Ti:S amplifier in the setup presented in Fig. 2.1 at a repetition rate of 100 kHz. The laser was routed into the microscope presented in Fig. 2.3. The photon counting board, outlined in Fig. 2.11, was used to record fluorescence lifetime data.

I performed two-photon imaging of the vasculature immediately after the injection of the micelles, shown in Fig. 6.5. Fluorescence lifetime data was acquired in two vessel regions (ROI 1 and ROI 2) and one region outside of any vessel (ROI 3), shown in Fig. 6.5. The measured lifetime at ROI 1 was 3.55 $\mu$s and at ROI 2 was 2.85 $\mu$s. These values correspond to low oxygen environments. The measured lifetime data at ROI 3 was not discernible as there was no decay curve, which confirms the micelles were localized to the blood vessels.

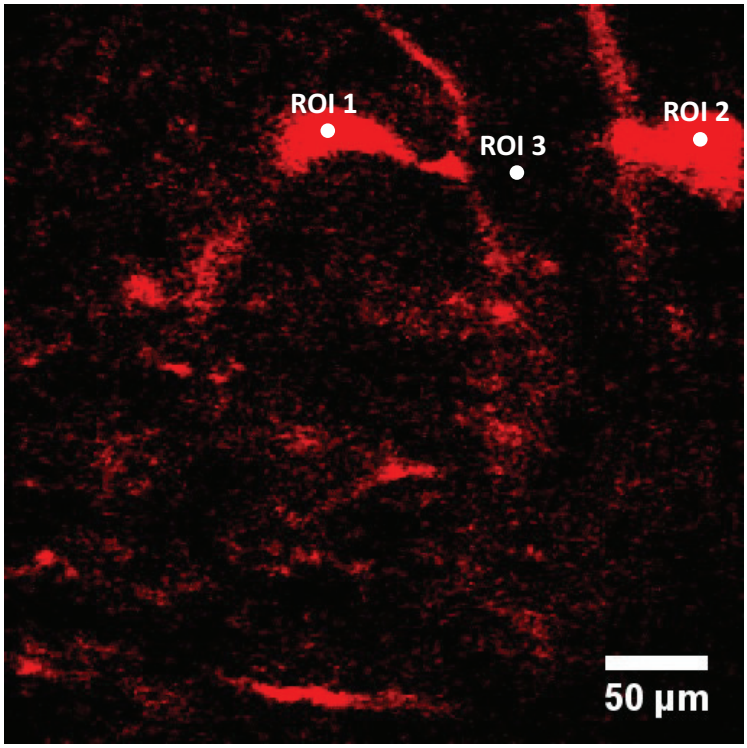


Figure 6.5: Two-photon microscopy image of vasculature labeled with Ruthenium micelles. Fluorescence lifetime data was taken at ROI 1, 2, and 3 to evaluate the oxygen levels inside and outside of the blood vessels.

One drawback to the Ruthenium micelles was that they cleared from the vessels within about 10 minutes. Future work should extend the clearance time to enable longer *in vivo* imaging sessions. Additionally, the signal level was low, in part due to the low concentration of the micelle batch.

## 6.5 Multiphoton Imaging of Self-assembled Vessels

The MPM system can be used for *ex vivo* imaging. Here, I demonstrate the ability of the system to evaluate the growth of vessel networks in a 3D

matrigel. The 3D matrigel contains pluripotent stem cells that self-organize into vascular networks. Calcein was used to stain live cells. Figure 6.6 shows a maximum intensity projection of a 50 $\mu$m stack in which vessel networks appear to be in the initial stages of self-assembly. The deep imaging capabilities of

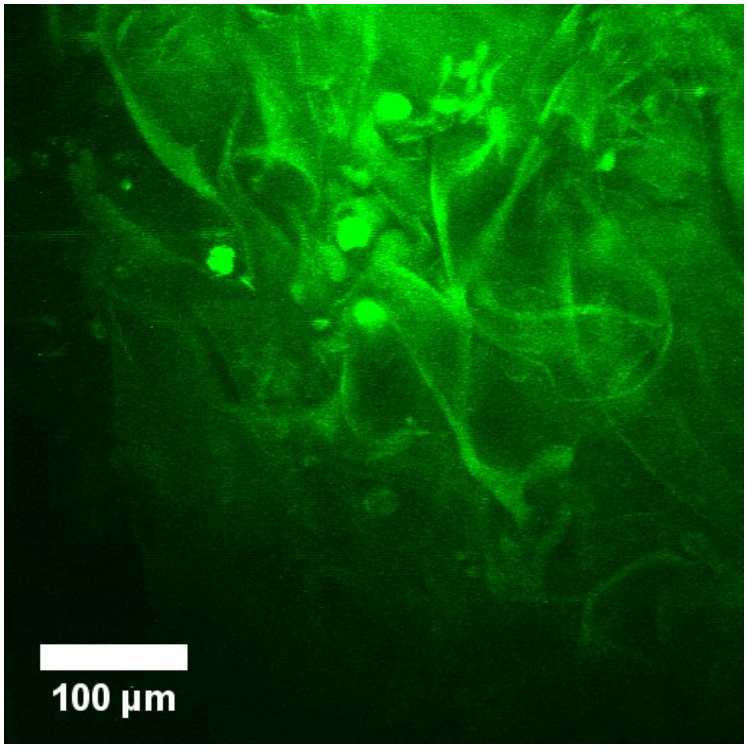


Figure 6.6: Maximum intensity projection image of a 50 $\mu$m thick 3D matrigel containing pluripotent stem cells that appear to be in the initial stages of vessel self-assembly. The matrigel is stained with calcein.

the MPM system are beneficial to image thick 3D matrigels. I was able to image 600 $\mu$m thick matrigels with high signal throughout the stack, on par with the signal-to-background ratios for *in vivo* deep imaging stacks. I suspect imaging multiple millimeter thick 3D matrigels is possible.

## 6.6 Does Quantum Entanglement Affect Neuron Firing?

While quantum mechanics and biology seem an unlikely breeding ground for synergy, recent developments in quantum biology have demonstrated quantum effects can explain some of biology's most pronounced processes. One such process is photosynthesis. While the quantum efficiency of state-of-the-art detectors is about 30%, photosynthesis units are able to reach an efficiency of nearly 100% for transporting light to reaction centers for storage. Engel et al. present strong evidence that this is due to energy transfer through quantum coherence, which significantly increases the efficiency of energy transfer [91]. Another potential example from biology is avian magnetoreception in which certain birds can navigate through sensing Earth's magnetic field [92]. While there is certainly more research required to understand the intricacies of these quantum effects, this suggests that quantum coherence effects in biological samples at room temperature is possible.

Due to the dependency of neural activity on individual molecules, it is interesting to consider the role, if any, of quantum mechanics in neural processes. Certainly the atomic underpinning of the brain's environment obeys quantum mechanics - however there is nothing special about the brain in that regard [93]. Rather, I am interested in applying a quantum biology approach to neural processes: Do any neural processes utilize quantum mechanics for improved cognitive ability?

The coherence time of a quantum state describes how long entangle-

ment can be maintained. Typical measured timescales of quantum coherence for everyday environments are on the order of picoseconds to attoseconds. Timescales can be extended to minutes in unique environments at temperatures approaching 0 Kelvin. Thus, the environment of the brain seems not conducive for quantum operations due to its high temperature and lack of environmental isolation - quantum coherence on the order of picoseconds seems too short to affect neural processes in an amplifying computational manner. However, aforementioned evidence from quantum biology points at the possibility that quantum coherence can be sustained on the order of microseconds in biological samples at room temperature. At the timescale of microseconds, this could have an effect on neural processes.

A possibility to explore is the quantum entanglement of ion spins. Quantum entanglement occurs when two particles, or more, become entangled such that each particle's state is dependent on the entire system state - that is, an individual particle state is no longer independent of the others. MPM imaging offers a route for testing the role of quantum mechanics in the brain due its ability to image at the cellular level and employment of ultrafast lasers which can be used to test a violation of Bell's inequality as proof of quantum entanglement.

Quantum chemistry predictions identify one candidate molecule for involvement in neural processes that has an extended coherence time. The "Posner" molecule, $Ca_9(PO_4)_6$, may have a coherence time up to 5 minutes due to it having a nuclear spin of 1/2 [94]; other spin 1/2 molecules may similarly

have long coherence times. The Posner molecule plays a role in presynaptic processes, thus it is possible that the uptake of multiple Posner molecules in different presynaptic neurons could induce entanglement between presynaptic neurons [94]. One possible experiment to test this hypothesis, inspired by [94] and crafted with the help of Scott Aaronson (S. Aaronson, personal communication, August 30 2016) who is a renown quantum theorist, is the following:

Step 1) Prepare an *in vitro* mouse brain sample with neurons that remain active. The sample should be transgenic such that neurons are labeled with a genetically encoded calcium indicator. The assumption here is that there exists many entangled Posner molecules within the brain sample.

Step 2) Slice the sample in half to create Sample A and Sample B. Quickly position Sample A and Sample B under independent microscopes separated by a distance on the order of 100 meters. The assumption here is that by slicing the sample, we spatially separate multiple entangled pairs of Posner molecules. These quantum states may stay entangled for up to 5 minutes. I note that it takes light 300 nanoseconds to travel 100 meters.

Step 3) In Sample A, lower the pH rapidly. This should cause the release of chemical bonds between Posner molecules and calcium in Sample A. The calcium fluorescence is collected by the microscope and analyzed with a half-wave plate and polarizing beam splitter, then measured by a time-correlated single photon counting board. Another possibility is to ablate Sample A with an ultrafast amplified laser which would presumably break any quantum co-

herence.

Simultaneously, measure the fluorescence signal from Sample B using a half-wave plate and polarizing beam splitter to analyze the polarization, and then measure the fluorescence with a second time-correlated single photon counting board. The assumption here is that Bell's inequality could be tested through coincidence and correlations between the fluorescence signal of Sample A and Sample B to reveal if entanglement was present. As noted previously, it would take light 300 ns to travel between Sample A and B. Coincidences below this are detectable with modern photon counting boards.

I investigated the experimental setup for such an experiment. Unfortunately, limitations in detectors and time-correlated single photon counting boards thwart the experimental realization. The quantum efficiency of detectors is only about 30%, and state-of-the-art time-correlated single photon counting boards have a temporal resolution on the order of picoseconds for single photons. If we optimistically assume that 100 entangled pairs existed in Sample A and B, we need to detect all of these pairs on the picosecond timescale to test Bell's inequality, however we are limited to a single photon measurement on this timescale. While such an experiment may not be able to test Bell's inequality, the experiment still offers the potential to put bounds on measurements of quantum coherence in the brain.

# Chapter 7

# Conclusion

## 7.1 Summary

The deep-tissue multiphoton microscopy imaging system described extends the imaging depth of traditional *in vivo* two-photon microscopy. The novelty of the microscope is the OPA light source. I demonstrate a high pulse energy (400 nJ), high repitetion rate (511 kHz) light source tunable between 1,100 nm and 1,400 nm can enable imaging depths to 1 mm for a variety of fluorescent dyes and proteins. I show imaging depths of 1,535 $\mu$m for vasculature and 1,160 $\mu$m for neurons, as well as measure functional blood flow information at a depth of 1,200 $\mu$m. The high repetition rate and high pulse energy of the OPA laser system produces high image quality with reasonable image acquisition times and fine axial steps for deep stacks, enabling the analysis of vascular morphology at depths to 1.45 mm.

Based on a theoretical model for the maximum imaging depth of multiphoton microcopy, I estimate the imaging depth of the OPA system could be extended beyond 1,600 $\mu$m and identify future improvements to the system and in general to realize such depths experimentally. One important aspect of extending the imaging depth requires the development of bright fluorophores

with optimal excitation wavelengths near 1,300 nm. I demonstrate many common fluorophores undergo 2PE and 3PE across the OPA spectrum near 1,300 nm, and characterize the brightness of Texas Red and ICG.

## 7.2 Future Work

The work presented in this dissertation showcases an empowering neuroimaging tool leveraging advances in laser technology and microscope optics to investigate the rodent brain at unprecedented imaging depth with cellular resolution. Though these imaging depths will advance basic neuroscience research, the current methods of MPM are limited to studying the rodent brain. This is because the human brain is much larger; the human cerebral cortex is multiple millimeters thick and thus a 1.5 mm imaging depth will not capture the full structure of the cortex. Future work should aim to further extend the imaging depth of the MPM system as well as expand the field of view. The second design of the scan optics (Section 2.3.2) will facilitate an increase in field of view for the presented system.

High-resolution, large field of view MPM imaging of the human brain should be attempted - and sooner rather than later. There are many hurdles to such an endeavor - such as access to willing human patients undergoing brain surgery necessitating a craniotomy and incorporating an ultrafast laser system into an operating room - but there is much to be gained from the possible insights. The work of optical imaging as a whole should move toward more translational work, particularly for diseases that are poorly understood

or poorly treated such as neurological disorders and cancers.

The work presented here and of others points to the ability of *in vivo* MPM imaging of the entire mouse cortex, and deeper structures such as the hippocampus, to chronically track both the structure and dynamics of blood vessel and neural networks. Particularly interesting for understanding the neural pathways of the brain is the development of systems that can simultaneously record traces of thousands of neurons within the mouse cortical volume. A synergistic development of decoding algorithms and deep MPM imaging systems will offer new insights into the functional architecture of blood vessel and neural networks. Examining these findings across healthy and disease state rodent models is an important step in understanding the cellular dynamics of neurological diseases. This dissertation demonstrates the ability for MPM imaging systems as an important tool to chronically track vessel and neural networks throughout the entire mouse brain cortex. Current preliminary work is applying this system to understand blood vessel and neuron recovery and reorganization after stroke. The ability to image cellular features and dynamics of the brain at increasing imaging depths will engender incredible insights into how the brain operates and empower effective neurological disorder treatments; further, these insights open new possibilities for neural interfaces to augment cognition in patients with neurological disorders, and the general public.

# Appendices

# Appendix A

# Derivation of Maxwell's Equations

This appendix is adapted with permission from World Scientific (Biophysical Reviews and Letters) from "The Physics of Vision" Vol 9, Issue 2, Copyright (2014) [95] for which David Miller independently wrote the manuscript and performed the research described within.

For a function $W$ to be a wave, it must satisfy the wave equation

$$\nabla^2 W = \frac{1}{\mathrm{v}^2}\frac{\partial^2 W}{\partial t^2} \tag{A.1}$$

where v is the speed of the wave, and $\nabla^2$ is the Laplacian (in cartesian coordinates $\nabla^2 = \frac{\partial^2}{\partial x^2} + \frac{\partial^2}{\partial y^2} + \frac{\partial^2}{\partial z^2}$) [96]. To determine if light satisfies the wave equation, we first need a function to describe the properties of light. For a quantitative description of light, we turn to electricity and magnetism.

In the 1800's, James Maxwell developed a set of equations to describe electric fields, **E**, and magnetic fields, **B**. Maxwell's equations in a vacuum,

such that there are no charges or current present, are:

$$\nabla \cdot \mathbf{E} = 0 \tag{A.2}$$

$$\nabla \cdot \mathbf{B} = 0 \tag{A.3}$$

$$\nabla \times \mathbf{E} = -\frac{\partial \mathbf{B}}{\partial t} \tag{A.4}$$

$$\nabla \times \mathbf{B} = \mu_o \epsilon_o \frac{\partial \mathbf{E}}{\partial t} \tag{A.5}$$

where $t$ is time, $\mu_o$ is the magnetic constant in vacuum, and $\epsilon_o$ is the electric constant in vacuum [96]. The first equation, $\nabla \cdot \mathbf{E} = 0$, represents that there is no source of electric fields. The second equation, $\nabla \cdot \mathbf{B} = 0$, represents that there are no sources for the magnetic field as a magnetic charge has never been found. The third equation, $\nabla \times \mathbf{E} = -\frac{\partial \mathbf{B}}{\partial t}$, represents that a magnetic field changing in time creates an electric field. The fourth equation, $\nabla \times \mathbf{B} = \mu_o \epsilon_o \frac{\partial \mathbf{E}}{\partial t}$, represents that an electric field changing in time creates a magnetic field. Notice the beautiful symmetry in Maxwell's equations for a vacuum - an electric field changing in time can create a magnetic field changing in time which in turn can create an electric field changing in time and the process can continue indefinitely.

Maxwell's equations can be used to show that electric and magnetic fields satisfy the wave equation in free space. The wave equation is a second-order linear partial differential equation involving the spatial and temporal derivatives of a single function. Thus, to determine if the electric and magnetic fields satisfy the wave equation, Maxwell's equations must be decoupled to isolate the electric and magnetic fields. This can be done for an electric field

using the vector calculus identity

$$\nabla \times (\nabla \times \mathbf{E}) = \nabla(\nabla \cdot \mathbf{E}) - \boldsymbol{\nabla^2 \mathbf{E}} \tag{A.6}$$

and plugging in $\nabla \times \mathbf{E} = -\frac{\partial \mathbf{B}}{\partial \mathbf{t}}$ on the left side of the equation and $\nabla \cdot \mathbf{E} = 0$ on the right to find

$$\nabla \times (-\frac{\partial \mathbf{B}}{\partial t}) = 0 - \nabla^2 \mathbf{E} \ . \tag{A.7}$$

We can then pull out the partial derivative with respect to time outside of the curl since the curl is a spatial derivative and does not depend on time:

$$-\frac{\partial}{\partial t}(\nabla \times \mathbf{B}) = -\boldsymbol{\nabla^2 \mathbf{E}} \ . \tag{A.8}$$

Plugging in $\nabla \times \mathbf{B} = \mu_{\mathbf{o}} \epsilon_{\mathbf{o}} \frac{\partial \mathbf{E}}{\partial \mathbf{t}}$ and applying the partial derivative with respect to time, we conclude

$$\nabla^2 \mathbf{E} = \mu_{\mathbf{o}} \epsilon_{\mathbf{o}} \frac{\partial^{\mathbf{2}} \mathbf{E}}{\partial \mathbf{t^2}} \tag{A.9}$$

which illustrates that $\mathbf{E}$ satisfies the wave equation. [96]

A similar derivation also shows that $\mathbf{B}$ satisfies the wave equation. We again start with the identity

$$\nabla \times (\nabla \times \mathbf{B}) = \nabla(\nabla \cdot \mathbf{B}) - \boldsymbol{\nabla^2 \mathbf{B}} \tag{A.10}$$

and plug in $\nabla \times \mathbf{B} = \mu_{\mathbf{o}} \epsilon_{\mathbf{o}} \frac{\partial \mathbf{E}}{\partial \mathbf{t}}$ and $\nabla \cdot \mathbf{B} = \mathbf{0}$. Pulling out the partial derivative with respect to time and constants on the left side, we find:

$$\mu_o \epsilon_o \frac{\partial}{\partial t}(\nabla \times \mathbf{E}) = -\boldsymbol{\nabla^2 \mathbf{B}} \ . \tag{A.11}$$

Next, plugging in $\nabla \times \mathbf{E} = -\frac{\partial \mathbf{B}}{\partial \mathbf{t}}$ and applying the partial derivative with respect to time, we conclude that

$$\nabla^2 \mathbf{B} = \mu_\mathbf{o} \epsilon_\mathbf{o} \frac{\partial^\mathbf{2} \mathbf{B}}{\partial \mathbf{t^2}} \ , \tag{A.12}$$

which illustrates that $\mathbf{B}$ satisfies the wave equation. Therefore, both the electric and magnetic field satisfy the wave equation. Comparing the decoupled forms of the electric field (Eq. A.9) and magnetic field (Eq. A.12) with the wave equation (A.1), we find that both the electric and magnetic field travel in vacuum with a speed of

$$\mathrm{v} = \frac{1}{\sqrt{\epsilon_o \mu_o}} \ . \tag{A.13}$$

$\epsilon_o$ appears in Coulomb's Law as a relation between the force on two charges at a distance; while $\mu_o$ appears in the Biot-Savart Law relating the magnetic field produced from the current in a wire. The magnetic constant is defined as $\mu_o = 4\pi \times 10^{-7}$ $\mathrm{Ns^2/C^2}$ and the electric constant is experimentally found to be $\epsilon_o = 8.85 \times 10^{-12}$ $\mathrm{C^2/Nm^2}$ where N is Newtons, C is Coulombs and s is seconds. Plugging in these values to Eq. A.13, we find that the electric and magnetic fields travel at a speed of $\mathrm{v} = 3 \times 10^8$ meters/second. Incredibly, this is the speed of light in a vacuum and we have thus shown that light is an electromagnetic wave! The speed of light in a vacuum is called $c$ to distinguish it from the speed of light in other media, which is defined as

$$\mathrm{v} = \frac{1}{\sqrt{\epsilon \mu}} \tag{A.14}$$

where $\epsilon$ and $\mu$ are the electric and magnetic constant for the specific medium. The index of refraction, $n$, relates the speed of light in a vacuum to other

media and is defined as:

$$n = \sqrt{\frac{\epsilon\mu}{\epsilon_o\mu_o}} = \frac{c}{\mathrm{v}} \tag{A.15}$$

where v represents the speed of light in the specific media. The index of refraction in vacuum is 1 by definition. All media[1] have an index of refraction greater than 1 meaning that light travels slower in media other than vacuum. [96]

[1]Except materials with negative indices of refraction.

# Appendix B

# Fourier Analysis of Light

This appendix is adapted with permission from World Scientific (Biophysical Reviews and Letters) from "The Physics of Vision" Vol 9, Issue 2, Copyright (2014) [95] for which David Miller independently wrote the manuscript and performed the research described within.

To understand the wave nature of light, let us consider the Fourier analysis of light. If we view light as a sinusoidal electromagnetic wave that stretches for infinite time, then we would expect to be able to determine the exact frequency of the wave, $f_o$, with no uncertainty. This is represented in Fourier analysis in that the Fourier transform of an infinite sinusoidal wave in the time domain to the frequency domain is a delta function at the positive and negative frequency of the wave. However, light does not extend for infinite time but rather is a localized electromagnetic sinusoidal wave. The temporal length of the wave, $\tau$, represents the amount of time for which the electromagnetic wave is a single sinusoidal wave [97].

Fourier analysis of a localized sinusoidal wave in the temporal domain requires that the amplitude of the wave equal zero at all times where the wave does not exist. To accomplish this, numerous frequencies are required

to create destructive interference everywhere except where the localized wave exists. Assuming the localized electromagnetic wave has a constant maximum amplitude, then we can view the wave as a convolution of a sinusoidal wave and square wave. The convolution theorem states that the Fourier transform of the convolution of two functions is the product of the Fourier transform of the functions [97]. Thus, the Fourier transform of a localized sinusoidal wave with constant maximum amplitude is the product of the Fourier transform of a sinusoidal wave and square wave. The Fourier transform of a square wave is the *sinc* function and thus, the Fourier transform of a localized sinusoidal wave is the product of a delta function and *sinc* function, depicted in Fig. B.1. Figure B.1 shows that a continuous set of frequencies is required to create a localized sinusoidal wave. The central maximum frequency, $f_o$, corresponds to the frequency of the infinitely long sinusoidal wave - thus, the frequency of the unlocalized wave contributes the strongest component in the frequency components of the localized wave.

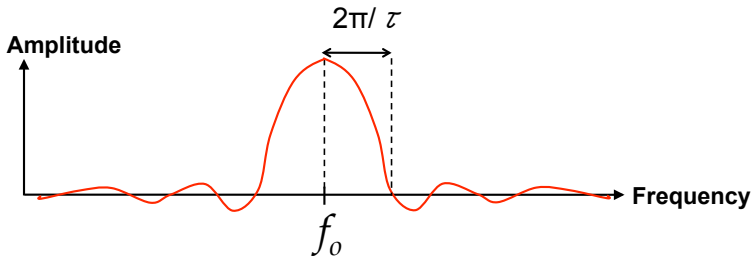


Figure B.1: The Fourier transform of a localized sinusoidal wave representing a localized electromagnetic wave. The Fourier transform is a *sinc* function in which the central peak, $f_o$ represents the frequency of the sinusoidal wave if it was infinitely long. The half-width of the central peak is $2\pi/\tau$.

The Fourier analysis of light is merely a mathematical model to describe the localization of an electromagnetic wave. When localization is used in a spatial sense, it is typically used to describe a particle. At the turn of the $20^{th}$ century, Max Planck proposed a radical idea that electromagnetic radiation - light - is emitted in quantized amounts [98]. Planck applied his notion to explain the "ultraviolet catastrophe" of blackbody radiation in which classical theories were in disagreement with experimental findings for the electromagnetic radiation emitted by a blackbody in the ultraviolet region of the electromagnetic spectrum. Planck solved the "catastrophe" by assuming that a quantum of light has an energy $E$ that is proportional to its frequency $f$ in the equation

$$E = hf \tag{B.1}$$

where $h$ is Planck's constant ($h = 6.63 \times 10^{-34}$Joule seconds) [97, 98]. A few years later in 1905, Albert Einstein explained the photoelectric effect using Planck's equation. The photoelectric effect refers to a metal ejecting electrons when incident light is above a threshold frequency. Einstein pointed out that electrons were only ejected if the frequency of the incident light was sufficiently high such that its energy overcame the minimum energy needed to remove the electron from an atom [98]. Niels Bohr further applied Planck's idea of quantization to the hydrogen atom in 1913 [97]. Bohr proposed that the energy levels of electrons within the hydrogen atom are quantized. Thus, when an electron drops from a higher energy state to a lower energy state, it emits a photon with an energy exactly equal to the energy difference in the

energy levels. This idea is the root of fluorescence. Another interpretation of an electron dropping from a higher energy state to a lower energy state is that the electron creates an electric field changing in time which then creates a magnetic field changing in time and therefore creates an electromagnetic wave. This interpretation brings the wave-particle duality of light full circle.

Planck's equation $E = hf$ bridges a gap between the wave and particle characteristics of light because it relates energy, a particle characteristic, and frequency, a wave characteristic. We can also substitute wavelength $\lambda$ into Planck's equation since frequency and wavelength are related by the speed of light $c$ (assuming light is traveling in vacuum) in the equation $f\lambda = c$. Thus, we find that the energy of light is inversely proportional to the wavelength:

$$E = \frac{hc}{\lambda} \ . \tag{B.2}$$

To summarize, light exhibits both wave and particle properties, both of which are important to understand multiphoton microscopy imaging. The construction of ultrafast pulses utilizes the wave properties of light in the intricate balance of destructive and constructive interference to create a pulse on the order of femtoseconds. The absorption of light by fluorophores uses the particle-like concept of light in which a molecule absorbs a quanta of energy to enter an excited state. This idea is also vital for the operation of photomultiplier tubes which use the photoelectric effect to convert light energy into a steam of electrons that are proportional to the intensity of the incoming light. The fluorescent photon that a molecule emits is also a particle-like

phenomena, however it can also be viewed from a wave perspective in that fluorescence is stimulated emission from "virtual photons" of the quantum fluctuations of the universe. The development and optimization of fluorophores relies on both of these principles.

# Bibliography


[1] J Fujimoto and W Drexler. *Optical Coherence Tomography: Technology and Applications*. Springer, 2015.

[2] Steven L. Jacques. Optical properties of biological tissues: a review. *Phys. Med. Biol.*, 58:R37–R61, 2013.

[3] H. Dana, B. Mohar, Y. Sun, S. Narayan, A. Gordus, J.P. Hasseman, T. Getahun, G.T. Holt, A. Hu, D. Walpita, and R. Patel et al. Sensitive red protein calcium indicators for imaging neural activity. *eLife*, 5:e12727, 2016.

[4] Mikhail Drobizhev, Nikolay S. Makarov, Shane E. Tillo, Thomas E. Hughes, and Aleksander Rebane. Two-photon absorption properties of fluorescent proteins. *Nat. Methods*, 8:393–399, 2011.

[5] T. Harris. Two-photon fluorescent probes. *URL: https://www.janelia.org/lab/harris-lab-apig/research/photophysics/two-photon-fluorescent-probes*, Accessed 12 June 2017.

[6] Demirhan Kobat, Michael E. Durst, Nozomi Nishimura, Angela W. Wong, Chris B. Schaffer, and Chris Xu. Deep tissue multiphoton microscopy using longer wavelength excitation. *Opt. Express*, 17:13354–13364, 2009.

[7] Chris Xu and Watt W. Webb. Measurement of two-photon excitation cross sections of molecular fluorophores with data from 690 to 1050 nm. *Opt. Soc. Am. B*, 13:481–491, 1996.

[8] Douglas A. Coulter. What is the two-photon process? *URL: http://www.-med.upenn.edu/twopcenter/whatis.shtml*, Accessed 27 February 2018.

[9] Arnold Delfino Estrada. High-resolution measurement of dissolved oxygen concentration in vivo using two-photon microscopy (doctoral dissertation). The University of Texas at Austin, Retrieved from Texas ScholarWorks 22 January 2018.

[10] Li-Chung Cheng, Nicholas G. Horton, Ke Wang, Shean-Jen Chen, and Chris Xu. Measurements of multiphoton action cross sections for multiphoton microscopy. *Biomed. Opt. Express*, 5:3427–3433, 2014.

[11] David R. Miller, Ahmed M. Hassan, Jeremy W. Jarrett, Flor A. Medina, Evan P. Perillo, Kristen Hagan, S. M. Shams Kazmi, Taylor A. Clark, Colin T. Sullender, Theresa A. Jones, Boris V. Zemelman, and Andrew K. Dunn. *In vivo* multiphoton imaging of a diverse array of fluorophores to investigate deep neurovascular structure. *Biomed. Opt. Express*, 8:3470–3481, 2017.

[12] David R. Miller, Jeremy W. Jarrett, Ahmed M. Hassan, and Andrew K. Dunn. Deep tissue imaging with multiphoton fluorescence microscopy. *Curr. Opin. Biomed. Eng.*, 4:32–39, 2017.

[13] F.A. Azevedo, L.R. Carvalho, L.T. Grinberg, J.M. Farfel, R.E. Ferretti, R.E. Leite, W. Jacob Filho, R. Lent, and S. Herculano-Houzel. Equal numbers of neuronal and nonneuronal cells make the human brain an isometrically scaled-up primate brain. *J. Comp. Neurol.*, 512:532–541, 2009.

[14] E.J. Benjamin, M.J. Blaha, and S.E. Chiuve et al. on behalf of the American Heart Association Statistics Committee & Stroke Statistics Subcommittee. Heart disease and stroke statistics 2017 update: a report from the American Heart Association. *Circulation*, 135:e229–e445, 2017.

[15] Quanhe Yang, Xin Tong, and Linda Schieb et al. Vital signs: Recent trends in stroke death rates. *Morbidity and Mortality Weekly Report*, 66:933–939, 2017.

[16] Winfried Denk, James H. Strickler, and Watt W. Webb. Two-photon laser scanning fluorescence microscopy. *Science*, 248:73–76, 1990.

[17] M.Z. Lin and M.J. Schnitzer. Genetically encoded indicators of neuronal activity. *Nat. Neuroscience*, 19:1142–1153, 2016.

[18] N.J. Sofroniew, D. Flickinger, J. King, and K. Svoboda. A large field of view two-photon mesoscope with subcellular resolution for in vivo imaging. *eLife*, 5:e14472, 2016.

[19] C. Tischbirek, A. Birkner, H. Jia, B. Sakamann, and A. Konnerth. Deep

two-photon brain imaging with a red-shifted fluorometric Ca2+ indicator. *Proc. Natl. Acad. Sci. USA*, 112:11377–82, 2015.

[20] P.S. Tsai, C. Mateo, J.J. Field, C.B. Schaffer, M.E. Anderson, and D. Kleinfeld. Ultra-large field-of-view two-photon microscopy. *Opt. Express*, 23:13833–13847, 2015.

[21] A.Y. Shih, J.D. Driscoll, P.J. Drew, N. Nishimura, C.B. Schaffer CB, and D. Kleinfeld. Two-photon microscopy as a tool to study blood flow and neurovascular coupling in the rodent brain. *J. Cereb. Blood Flow. Metab.*, 32:1277–1309, 2011.

[22] Fritjof Helmchen and Winfried Denk. Deep tissue two-photon microscopy. *Nat. Methods*, 2:932–940, 2005.

[23] Nicholas G. Horton, Ke Wang, Demirhan Kobat, Catharine G. Clark, Frank W. Wise, Chris B. Schaffer, and Chris Xu. *In vivo* three-photon microscopy of subcortical structures within an intact mouse brain. *Nat. Photonics*, 7:205–209, 2013.

[24] J.A. Kubby. Adaptive optics for biological imaging. *CRC Press*, 2013.

[25] K. Wang, W. Sun, C.T. Richie, B.K. Harvey, E. Betzig, and N. Ji. Direct wavefront sensing for high-resolution in vivo imaging in scattering tissue. *Nat. Commun.*, 6:7276, 2015.

[26] Patrick Theer, Mazahir T. Hasan, and Winfried Denk. Two-photon imaging to a depth of 1000 $\mu$m in living brains by use of Ti:$Al_2O_3$ regenerative amplifier. *Opt. Lett.*, 28:1024–1022, 2003.

[27] Demirhan Kobat, Nicholas G. Horton, and Chris Xu. *In vivo* two-photon microscopy to 1.6-mm depth in mouse cortex. *J. Biomed. Opt.*, 16:106014–1 – 106014–4, 2011.

[28] D. G. Ouzounov, T. Wang, M. Wang, D. D. Feng, N. G. Horton, J. C. Cruz-Hernández, Y. Cheng, J. Reimer, A. S. Tolias, N. Nishimura, and C. Xu. In vivo three-photon imaging of activity of GCaMP6-labeled neurons deep in intact mouse brain. *Nat. Methods*, 14:288–390, 2017.

[29] H.M. Kim and B.R. Cho. Small-molecule two-photon probes for bioimaging applications. *Chem. Rev.*, 115:5014–5055, 2015.

[30] J.V. Frangioni. In vivo near-infrared fluorescence imaging. *Chem. Biol.*, 7:626–634, 2003.

[31] U. Resch-Genger, M. Grabolle, S. Cavaliere-Jaricot, R. Nitschke, and T. Nann. Quantum dots versus organic dyes as fluorescent labels. *Nat. Methods*, 5:763–775, 2008.

[32] D.R. Larson, W.R. Zipfel, R.M. Williams, S.W. Clark, M.P. Bruchez, F.W. Wise, and W.W. Webb. Water-soluble quantum dots for multiphoton fluorescence imaging in vivo. *Science*, 300:1434–1436, 2003.

[33] I.L. Medintz, H.T. Uyeda, E.R. Goldman, and H. Mattoussi. Quantum dot bioconjugates for imaging, labelling and sensing. *Nat. Mater.*, 4:435–446, 2005.

[34] W. Changfeng and D.T. Chiu. Highly fluorescent semiconducting polymer dots for biology and medicine. *Angew. Chem. Int. Edit.*, 52:3086–3109, 2013.

[35] W. Changfeng, C. Szymanski, Z. Cain, and J. McNeill. Conjugated polymer dots for multiphoton fluorescence imaging. *J. Am. Chem. Soc.*, 129:12904–12905, 2007.

[36] J. Pecher, J. Huber, M. Winterhalder, A. Zumbusch, and S. Mecking. Tailor-made conjugated polymer nanoparticles for multicolor and multiphoton cell imaging. *Biomacromolecules*, 11:2776–2780, 2010.

[37] N.C. Shaner, P.A. Steinbach, and R.Y. Tsien. A guide to choosing fluorescent proteins. *Nat. Methods*, 2:905–909, 2005.

[38] R. Bianchi, A. Teijeira, S.T. Proulx, A.J. Christiansen, C.D. Seidel, T. Rülicke, T. Mäkinen, R. Hägerling, C. Halin, and M. Detmar. A transgenic prox1-cre-tdtomato reporter mouse for lymphatic vessel research. *PLoS One*, 10:e0122976, 2015.

[39] D. Shcherbo, C.S. Murphy, G.V. Ermakova, E.A. Solovieva, T.V. Chepurnykh, A.S. Shcheglov, V.V. Verkhusha, V.Z. Pletnev, K.L. Hazelwood,

P.M. Roche, and S. Lukyanov. Far-red fluorescent tags for protein imaging in living tissues. *Biochem. J.*, 15:567–574, 2009.

[40] O.S. Finikova, A.Y. Lebedev, A. Aprelev, T. Troxler, F. Gao, C. Garnacho, S. Muro, R.M. Hochstrasser, and S.A. Vinogradov. Oxygen microscopy by two-photon-excited phosphorescence. *ChemPhysChem*, 9:1673–1679, 2008.

[41] L. Gagnon L, S. Sakadžić, F. Lesage, J.J. Musacchia, J. Lefebvre, Q. Fang Q, M.A. Ycel, K.C. Evans, E.T. Mandeville, J. Cohen-Adad, J.R. Polimeni, M.A. Yaseen, E.H. Lo, D.N. Greve, R.B. Buxton, A.M. Dale, A. Devor, and D.A. Boas. Quantifying the microvascular origin of bold-fmri from first principles with two-photon microscopy and an oxygen-sensitive nanoprobe. *J. Neurosci.*, 25:3663–3675, 2015.

[42] C. Stosiek, O. Garaschuk, K. Holthoff, and A. Konnerth. In vivo two-photon calcium imaging of neuronal networks. *P. Natl. Acad. Sci. USA*, 100:7319–7324, 2003.

[43] L.L. Looger and O. Griesbeck. Genetically encoded neural activity indicators. *Curr. Opin. Neurobiol.*, 22:18–23, 2012.

[44] B.L. Sabatini, T.G. Oertner, and K. Svoboda. The life cycle of ca 2+ ions in dendritic spines. *Neuron*, 33:439–452, 2002.

[45] J. Akerboom, T.W. Chen, T.J. Wardill, L. Tian, J.S. Marvin, S. Mutlu, N.C. Calderón, F. Esposti, B.G. Borghuis, X.R. Sun, and A. Gordus.

Optimization of a gcamp calcium indicator for neural activity imaging. *J. Neurosci.*, 32:13819–40, 2012.

[46] L. Tian, S.A. Hires, T. Mao, D. Huber, M.E. Chiappe, S.H. Chalasani, L. Petreanu, J. Akerboom, S.A. McKinney, E.R. Schreiter, and C.I. Bargmann. Imaging neural activity in worms, flies and mice with improved gcamp calcium indicators. *Nat. Methods*, 6:875–881, 2009.

[47] J. Nakai, M. Ohkura, and K. Imoto. A high signal-to-noise Ca2+ probe composed of a single green fluorescent protein. *Nat. Biotechnol.*, 19:137–141, 2001.

[48] T.W. Chen, T.J. Wardill, Y. Sun, S.R. Pulver, S.L. Renninger, A. Baohan, E.R. Schreiter, R.A. Kerr, M.B. Orger, V. Jayaraman, and L.L. Looger. Ultrasensitive fluorescent proteins for imaging neuronal activity. *Nature*, 499:25–300, 2013.

[49] M. Inoue, A. Takeuchi, S.I. Horigane, M. Ohkura, K. Gengyo-Ando, H. Fujii, S. Kamijo, S. Takemoto-Kimura, M. Kano, J. Nakai, K. Kitamura, and H. Bito. Rational design of a high-affinity, fast, red calcium indicator R-CaMP2. *Nat. Methods*, 12:64–70, 2015.

[50] C. Xu and W.R. Zipfel. Multiphoton excitation of fluorescent probes. *Cold Spring Harbor Protocols*, 2015.

[51] J. Mütze, V. Iyer, J.J. Macklin, J. Colonell, B. Karsh, Z. Petráek, P. Schwille, L.L. Looger, L.D. Lavis, and T.D. Harris. Excitation spec-

tra and brightness optimization of two-photon excited probes. *Biophys. J.*, 102:934–944, 2012.

[52] M. Kauert, P.C. Stoller, M. Frenz, and J. Ricka. Absolute measurement of molecular two-photon absorption cross-sections using a fluorescence saturation technique. *Opt. Express*, 14:8434–8447, 2006.

[53] D.A. Oulianov, I.V. Tomov, A.S. Dvornikov, and P.M. Rentzepis. Observations on the measurement of two-photon absorption cross-section. *Opt. Commun.*, 191:235–243, 2001.

[54] P. Tian and W.S. Warren. Ultrafast measurement of two-photon absorption by loss modulation. *Opt. Lett.*, 27:1634–1636, 2002.

[55] P. Sengupta, J. Balaji, S. Banerjee, R. Philip, G.R. Kumar, and S. Maiti. Sensitive measurement of absolute two-photon absorption cross sections. *J. Chem. Phys.*, 112:9201–9205, 2000.

[56] R. Kapoor, C.S. Friend, and A. Patra. Two-photon-excited absolute emission cross-sectional measurements calibrated with a luminance meter. *J. Opt. Soc. Am. B*, 20:1550–1554, 2003.

[57] M.Y. Berezin, C. Zhan, H. Lee, C. Joo, W.J. Akers, S. Yazdanfar, and S. Achilefu. Two-photon optical properties of near-infrared dyes at 1.55 $\mu$m excitation. *J. Phys. Chem. B*, 115:11530–11535, 2011.

[58] C. Le Droumaguet, O. Mongin, M.H.V. Werts, and M. Blanchard-Desce. Towards "smart" multiphoton fluorophores: strongly solvatochromic probes

for two-photon sensing of micropolarity. *Chem. Commun.*, pages 2802–2804, 2005.

[59] Albert Einstein. Concerning an heuristic point of view toward the emission and transformation of light. *Annalen der Physik.*, 17:132–148, 1905.

[60] Albert Einstein. Strahlungs-emission and -absorption nach der quanentheorie [emission and absorption of radiation in quantum theory]. *Deutsche Physikalische Gesellschaft.*, 18:318–323, 1916.

[61] Barry R. Masters and Peter So. *Handbook of Biomedical Nonlinear Optical Microscopy*. Oxford University Press, 2008.

[62] J. Lakowicz. *Topics in Fluorescence Spectroscopy: Nonlinear and Two-Photon Induced Fluorescence*, volume 5. Plenum Press, New York, 2008.

[63] Maria Göppert-Mayer. Über elementarakte mit zwei quantensprüngen. *Annalen der Physik*, 1931.

[64] David R. Miller. Extending the depth limit of multiphoton microscopy for in vivo brain imaging (master's thesis). The University of Texas at Austin, Retrieved from Texas ScholarWorks 22 January 2018.

[65] Giulio Cerullo and Sandro De Silvestri. Ultrafast optical parametric amplifiers. *Rev. Sci. Instrum.*, 74:1–18, 2003.

[66] Chris Xu, Jeffrey Guild, Watt W. Webb, and Winfried Denk. Determination of absolute two-photon excitation cross sections by in situ second-order autocorrelation. *Opt. Lett.*, 20:2372–2374, 1995.

[67] S. M. Shams Kazmi, Anthony J. Salvaggio, Arnold D. Estrada, Michael A. Hemati, Nazariy K. Shaydyuk, Emannuel Roussakis, Theresa A. Jones, Sergei A. Vinogradov, and Andrew K. Dunn. Three-dimensional mapping of oxygen tension in cortical arterioles before and after occlusion. *Biomed. Opt. Express*, 4:1061 – 1073, 2013.

[68] Adrian Negrean and Huibert D. Mansvelder. Optimal lens design and use in laser-scanning microscopy. *Biomed. Opt. Express*, 5:1588–1609, 2014.

[69] Jonathan R. Bumstead, Jasmine J. Park, Isaac A. Rosen Andrew W. Kraft, Patrick W. Wright, Matthew D. Reisman, Daniel C. Côté, and Joseph P. Culver. Designing a large field-of-view two-photon microscope using optical invariant analysis. *Neurophotonics*, 5:025001, 2018.

[70] Chris Xu, Warren Zipfel, Jason B. Shear, Rebecca M. Williams, and Watt W. Webb. Multiphoton fluorescence excitation: New spectral windows for biological nonlinear microscopy. *Proc. Natl. Acad. Sci.*, 93:10763–10768, 1996.

[71] M. A. Albota, C. Xu, and W. W. Webb. Two-photon fluorescence excitation cross sections of biomolecular probes from 690 to 960 nm. *Appl. Optics*, 37:7352–7356, 1998.

[72] Nikolay S. Makarov, Mikhail Drobizhev, and Aleksander Rebane. Two-photon absorption standards in the 550-1600 nm excitation wavelength range. *Opt. Express*, 16:4029–4047, 2008.

[73] Evan P. Perillo, Justin E. McCracken, Daniel C. Fernée, John R. Goldak, Flor A. Medina, David R. Miller, Hsin-Chih Yeh, and Andrew K. Dunn. Deep in vivo two-photon microscopy with a low cost custom built mode-locked 1060 nm fiber laser. *Biomed. Opt. Express*, 7:324–334, 2016.

[74] Philbert S. Tsai, Pablo Blinder, Benjamin J. Migliori, Joseph Neev, Yishi Jin, Jeffrey A. Squier, and David Kleinfeld. Plasma-mediated ablation: An optical tool for submicrometer surgery on neuronal and vascular systems. *Curr. Opin. Biotech.*, 20:90–99, 2009.

[75] J. Schindelin, I. Arganda-Carreras, E. Frise, V. Kaynig, M. Longair, T. Pietzsch, S. Preibisch, C. Rueden, S. Saalfeld, B. Schmid, J. Tinevez, D. J. White, V. Hartenstein, K. Eliceiri, P. Tomancak, and A. Cardona. Tfiji: an open-source platform for biological-image analysis. *Nat. Methods*, 9:676–682, 2012.

[76] J. Ahrens, B. Geveci, and C. Law. *ParaView: An End-User Tool for Large Data Visualization*. Elsevier, 2005.

[77] P. Tsai, J. P. Kaufhold, P. Blinder, B. Friedman, P. J. Drew, H. J. Karten, P. D. Lyden, and D. Kleinfeld. Correlations of neuronal and microvascular densities in murine cortex revealed by direct counting and colocalization of nuclei and vessels. *J. Neurosci.*, 46:14553–14570, 2009.

[78] J. P. Kaufhold, P. S. Tsai, P. Blinder, and D. Kleinfeld. Vectorization of optically sectioned brain microvasculature: learning aids completion of

vascular graphs by connecting gaps and deleting open-ended segments. *Med. Image Anal.*, 16:1241–1258, 2012.

[79] David R. Rivera, Christopher M. Brown, Dimitre G. Ouzounov, Ina Pavlova, Demirhan Kobat, Watt W. Webb, and Chris Xu. Compact and flexible raster scanning multiphoton endoscope capable of imaging unstained tissue. *P. Natl. Acad. Sci. USA*, 108:17598–17603, 2011.

[80] Supang Khondee and Thomas D. Wang. Progress in molecular imaging in endoscopy and endomicroscopy for cancer imaging. *J. Healthc. Eng.*, 4:1–22, 2013.

[81] K. A. Tennant, D. L. Adkins, N. A. Donlan, A. L. Asay, N. Thomas, J. A. Kleim, and T. A. Jones. The organization of the forelimb representation of the C57BL/6 mouse motor cortex as defined by intracortical microstimulation and cytoarchitecture. *Cereb. Cortex.*, 21:865–876, 2011.

[82] E. Beaurepaire, M. Oheim, and J. Mertz. Ultra-deep two-photon fluorescence excitation in turbid media. *Opt. Comm.*, 188:25–29, 2001.

[83] G. Olivié, D. Giguére, F. Vidal, T. Ozaki, J.-C. Kieffer, O. Nada, and I. Brunette. Wavelength dependence of femtosecond laser ablation threshold of corneal stroma. *Opt. Express*, 16:4121–4129, 2008.

[84] N. Nishimura, C. B. Schaffer, B. Friedman, P.S. Tsai, P. D. Lyden, and D. Kleinfeld. Targeted insult to subsurface cortical blood vessels using

ultrashort laser pulses: three models of stroke. *Nat. Methods*, 3:99–108, 2006.

[85] Martin Oheim, Emmanuel Beaurepaire, Emmanuelle Chaigneau, Jerome Mertz, and Serge Charpak. Two-photon microscopy in brain tissue: parameters influencing the imaging depth. *J. Neurosci. Meth.*, 111:29–37, 2001.

[86] Yuxin Wang, Wenhui Wen, Kai Wang, Peng Zhai, Ping Qiu, and Ke Wang. Measurement of absorption spectrum of deuterium oxide (D2O) and its application to signal enhancement in multiphoton microscopy at the 1700-nm window. *Appl. Phys. Lett.*, 108:021112, 2016.

[87] Pierre Mahou, Maxwell Zimmerley, Karine Loulier, Katherine S. Matho, Guillaume Labroille, Xavier Morin, Willy Supatto, Jean Livet, Delphine Débarre, and Emmanuel Beaurepaire. Multicolor two-photon tissue imaging by wavelength mixing. *Nat. Methods*, 9:815–818, 2012.

[88] Harold Dehez, Michel Piché, and Yves De Koninck. Resolution and contrast enhancement in laser scanning microscopy using dark beam imaging. *Opt. Express*, 21:15912–15925, 2013.

[89] B. Richards and E. Wolf. Electromagnetic diffraction in optical systems, II. Structure of the image field in an aplanatic system. *Proc. R. Soc. Lond. A. Math. Phys. Sci.*, 253:358–379, 1959.

[90] Aamir A. Khan, Genevieve D. Vigil, Yide Zhang, Susan K. Fullerton-Shirey, and Scott S. Howard. Silica-coated ruthenium-complex nanoprobes for two-photon oxygen microscopy in biological media. *Opt. Mater. Express*, 7:1066–1076, 2017.

[91] Gregory S. Engel, Tessa R. Calhoun, Elizabeth L. Read, Tae-Kyu Ahn, Tomáš Mančal, Yuan-Chung Cheng, Robert E. Blankenship, and Graham R. Fleming. Evidence for wavelike energy transfer through quantum coherence in photosynthetic systems. *Nature*, 446:782–786, 2007.

[92] Neill Lambert, Yueh-Nan Chen, Guang-Yin Chen Yuan-Chung Chengand Che-Ming Li, and Franco Nori. Quantum biology. *Nat. Phys.*, 9:10–18, 2013.

[93] Christof Koch and Klaus Hepp. Quantum mechanics in the brain. *Nature*, 440:611–612, 2006.

[94] Matthew P.A. Fisher. Quantum cognition: The possibility of processing with nuclear spins in the brain. *Annals of Physics*, 362:593–602, 2015.

[95] David R. Miller. The physics of vision. *Biophysical Reviews and Letters.*, 2014.

[96] D. Griffiths. *Introduction to Electrodynamics*, volume Second Edition. Prentice Hall, 1989.

[97] Frank L. Pedrotti, Leno S. Pedrotti, and Leno M. Pedrotti. *Introduction to Optics*, volume Third Edition. Pearson Prentice Hall, 2007.

[98] J. Taylor, C. Zafiratos, and M. Dubson. *Modern Physics for Scientists and Engineers*, volume Second Edition. Prentice Hall, 2004.

[99] Chun-Yu Lin, Chi-Hsiang Lien, Keng-Chi Cho, Chia-Yuan Chang, Nan-Shan Chang, Paul J. Campagnola, Chen Yuan Dong, and Shean-Jen Chen. Investigation of two-photon excited fluorescence increment via crosslinked bovine serum albumin. *Opt. Express*, 20:13676, 2012.

[100] Christian J Schrandt, SM Shams Kazmi, Theresa A Jones, and Andrew K Dunn. Chronic monitoring of vascular progression after ischemic stroke using multiexposure speckle imaging and two-photon fluorescence microscopy. *J. Cereb. Blood Flow Metab.*, 35:933–942, 2015.

[101] N. Nishimura, C. B. Schaffer, B. Friedman, P. D. Lyden, and D. Kleinfeld. Penetrating arterioles are a bottleneck in the perfusion of neocortex. *P. Natl. Acad. Sci. USA*, 104:365–370, 2007.

[102] Hossmann KA. Pathophysiology and therapy of experimental stroke. *Cell Mol. Neurobiol.*, 26:1057–1083, 2006.

[103] Timothy H. Murphy and Dale Corbett. Plasticity during stroke recovery: from synapse to behaviour. *Nat. Rev. Neuroscience*, 10:861–872, 2009.

# Vita

David Miller received a B.A. in Physics from Carleton College where he studied electromagnetic theory and quantum gravity, and conducted research for the LIGO collaboration. He came to UT Austin to study the intersection of physics and neuroscience.

Email address: david.r.miller8@gmail.com.

This dissertation was typed by David Miller and typeset with LaTeX.